Science of the Total Environment 926 (2024) 172025

Contents lists available at ScienceDirect

Science of the Total Environment

journal homepage: www.elsevier.com/locate/scitotenv

Review

Iron-containing nanominerals for sustainable phosphate management: A comprehensive review and future perspectives

Teng Bao [a,b,c,g], Mekdimu Mezemir Damtie [b,d], Chu Yan Wang [a], Cheng Long Li [a], Zhijie Chen [e], Kuk CHO [c], Wei Wei [b], Peng Yuan [f], Ray L. Frost [g], Bing-Jie Ni [b,e,*]

[a] School of Biology, Food and Environment Engineering, Hefei University, China
[b] Centre for Technology in Water and Wastewater, School of Civil and Environmental Engineering, University of Technology Sydney, Sydney, NSW 2007, Australia
[c] Department of Environmental Engineering, College of Engineering, Pusan National University, 2 Busandaehak-ro 63beon-gil, Geumjeong-gu, Busan 46241, South Korea
[d] Water Resources Engineering Department, Adama Science and Technology University, Adama, P.O. Box 1888, Ethiopia
[e] School of Civil and Environmental Engineering, The University of New South Wales, Sydney, NSW 2052, Australia
[f] KAUST Catalysis Center (KCC), Division of Physical Sciences and Engineering, King Abdullah University of Science and Technology (KAUST), Thuwal 23955-6900, Saudi Arabia
[g] Nanotechnology and Molecular Science Discipline, Faculty of Science and Engineering, Queensland University of Technology (QUT), 2 George Street, GPO Box 2434, Brisbane, QLD 4000, Australia

HIGHLIGHTS

- Modified iron-containing nanominerals (mICNs) have higher phosphate removal efficiency than ICNs.
- The phosphate removal mechanism of mICNs is coordinated by multiple mechanisms.
- Compared with anions/organic matter, cations can promote phosphate removal from mICNs.
- mICNs saturated with adsorbed phosphate can be used as fertilizer to promote plant growth.
- mICNs can effectively manage eutrophic municipal wastewater, seawater, and lake water.

GRAPHICAL ABSTRACT

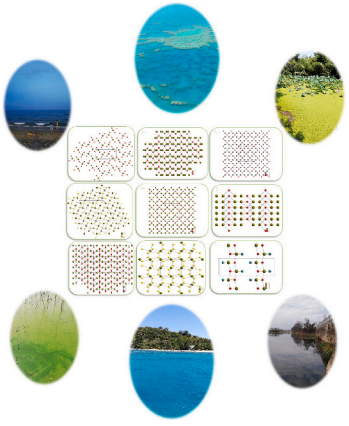

ARTICLE INFO

Editor: Yifeng Zhang

Keywords:
Iron-containing nanominerals
Modification
Phosphate management

ABSTRACT

Adsorption, which is a quick and effective method for phosphate management, can effectively address the crisis of phosphorus mineral resources and control eutrophication. Phosphate management systems typically use iron-containing nanominerals (ICNs) with large surface areas and high activity, as well as modified ICNs (mICNs). This paper comprehensively reviews phosphate management by ICNs and mICNs in different water environments. mICNs have a higher affinity for phosphates than ICNs. Phosphate adsorption on ICNs and mICNs occurs

* Corresponding author at: Centre for Technology in Water and Wastewater, School of Civil and Environmental Engineering, University of Technology Sydney, Sydney, NSW 2007, Australia.
E-mail address: bingjieni@gmail.com (B.-J. Ni).

https://doi.org/10.1016/j.scitotenv.2024.172025
Received 4 January 2024; Received in revised form 25 March 2024; Accepted 25 March 2024
Available online 29 March 2024

Adsorption mechanism
Phosphate resource recovery

through mechanisms such as surface complexation, surface precipitation, electrostatic ligand exchange, and electrostatic attraction. Ionic strength influences phosphate adsorption by changing the surface potential and isoelectric point of ICNs and mICNs. Anions exhibit inhibitory effects on ICNs and mICNs in phosphate adsorption, while cations display a promoting effect. More importantly, high concentrations and molecular weights of natural organic matter can inhibit phosphate adsorption by ICNs and mICNs. Sodium hydroxide has high regeneration capability for ICNs and mICNs. Compared to ICNs with high crystallinity, those with low crystallinity are less likely to desorb. ICNs and mICNs can effectively manage municipal wastewater, eutrophic seawater, and eutrophic lakes. Adsorption of ICNs and mICNs saturated with phosphate can be used as fertilizers in agricultural production. Notably, mICNs and ICNs have positive and negative effects on microorganisms and aquatic organisms in soil. Finally, this study introduces the following: trends and prospects of machine learning-guided mICN design, novel methods for modified ICNs, mICN regeneration, development of mICNs with high adsorption capacity and selectivity for phosphate, investigation of competing ions in different water environments by mICNs, and trends and prospects of in-depth research on the adsorption mechanism of phosphate by weakly crystalline ferrihydrite. This comprehensive review can provide novel insights into the research on high-performance mICNs for phosphate management in the future.

1. Introduction

As a globally strategic resource, phosphorus is regarded as a nonrenewable resource that is crucial for the nutrition of plants and organisms (Dong et al., 2023). With growing populations and economic development, a large volume of phosphate-rich, arbitrary domestic and industrial wastewater has been discharged into the environment. A statistical report in Li, 2017 revealed that 61.47 % of China's lakes have reached a medium eutrophic state, while 30.28 % are eutrophic (Almanassra et al., 2021). Eutrophication due to excessive discharge of phosphates into lakes and rivers has adversely affected ecosystems (Dong et al., 2023). Phosphate in water resources is mainly sourced from i) eutrophic wastewater with a low phosphate concentration after purification and ii) phosphate in farmland runoff due to dissolution and loss of phosphate fertilizers by rainwater (Almanassra et al., 2021). Meanwhile, phosphate from fertilizers mainly contributes to the formation of microcystins and algal blooms in surface water (Dai et al., 2016; Li et al., 2016; Sun et al., 2018; Vieira and Lijklema, 1989; Wang et al., 2017a). The water quality of treated wastewater reuse (RSC) for agricultural use in China has been intensively investigated to address the shortage of water resources and anticipated food insecurity challenges (Lyu et al., 2016; Wang et al., 2007). The replenishment of land with phosphate waste, whether from RSC or fertilizer runoff, will contribute to recycling and reuse and will facilitate sustainable development (Yi et al., 2011).

The main form of phosphorus in the environment is phosphate, which is transformed from phosphorus through microbial metabolic processes (Almanassra et al., 2021; Wang et al., 2017a). Phosphate in wastewater is usually removed by coagulation, biological activity, ion exchange, membrane separation, adsorption, or precipitation (Dai et al., 2016; Li et al., 2016). Compared with other recovery methods, phosphate recovery via adsorption is particularly popular because it is simpler, more reliable, more efficient, and more applicable but requires the selection of efficient adsorbents (Almanassra et al., 2021).

Iron-containing nanomaterials (ICNs) are nanometer-sized natural minerals (ferrihydrite). Nano-micron-sized mineral particles or large crystals, such as hematite, siderite, pyrite, pyrrhotite, maghemite, limonite, goethite, and magnetite, are found in the environment (Anschutz and Penn, 2005; Baek et al., 2019; Banfield and Zhang, 2001; Bonneville et al., 2004; Levett et al., 2020; Xie et al., 2017). ICNs are important active nanominerals that are widely distributed as crystalline and weakly crystalline forms in the supergene eco-environment. They are characterized by large surface hydroxyl site densities, large specific surface areas (SSAs), high reactivity, and variable positive charges (Banfield and Zhang, 2001; Barrón and Torrent, 2013; Bonneville et al., 2004). The physical and chemical properties and environmental migration capabilities of ICNs differ from those of large particles. ICNs are involved in various geochemical and biogeochemical processes, including lake phosphate management, eutrophication of seawater management, and phosphate management in urban wastewater.

Modified ICNs (mICNs) have achieved higher removal efficiency than ICNs (Bose et al., 2009; Byrne et al., 2015). Several reviews have focused on phosphate management by modified biochars (Almanassra et al., 2021), lanthanum-based adsorbents (He et al., 2022), attapulgite-based adsorbents (Liu et al., 2023), iron-based materials (Wang et al., 2021a), and iron oxide mineral-based adsorbents (Wang et al., 2023). However, systematic reports on the management of phosphate by ICNs and mICNs are lacking. A comprehensive review should cover the crystal structural characteristics, modification methods, adsorption mechanisms, competitive substances, and applications of ICNs and mICNs in municipal wastewater, lake eutrophication management, eutrophic seawater management, and agricultural phosphate fertilization after phosphate adsorption. More importantly, the phosphate adsorption mechanisms of ICNs and mICNs have not been systematically explained and remain contentious. The adsorption–desorption of phosphate to/from ICNs also affects the evolution and geochemical behavior of ICNs. Interestingly, phosphate-containing iron ore has been recently found on the Moon (Guo et al., 2022; Yao et al., 2022).

This comprehensive review assesses the crystal structure of ICN, evaluates its unique surface–interface properties, and examines modification methods for ICN (such as calcination modification using H_2, O_2, and N_2) (Chen et al., 2015; Cheng et al., 2017; Liu et al., 2013b; Xing et al., 2017). The effects of substitution on the surface physicochemical properties, crystal structures, and phosphate management of ICNs modified by aluminum (Al) impregnation (Li et al., 2016b; Li et al., 2016c; Liao et al., 2020), pyrolysis-formed biochar (Zhang et al., 2020a), and surface decoration with lanthanum (La) or cerium (Ce) are also reviewed (Fang et al., 2018; Shan et al., 2021). The mechanisms of phosphate removal by ICNs and mICNs, including electrostatic interaction, surface precipitation, electrostatic ligand adsorption, and surface complexation adsorption, are discussed. Subsequently, the effects of other factors on phosphate management by ICNs and mICNs, including the complexation of ICNs and mICNs with competitive ions, are reviewed. The applications of ICNs and mICNs to phosphate management in municipal wastewater, eutrophic seawater, and lakes are then summarized, concentrating on applications of agricultural phosphate fertilizer, the current understanding of the geochemical phosphate cycle, and solutions for improving the ecological phosphate environment. Finally, the advancement and future directions of ICNs and mICNs are discussed.

2. Summary of phosphorous wastewater management

2.1. Summary of different sources of phosphorus-rich wastewater

Multiple forms of phosphorus are available in wastewater, revealing easily removable phosphates in granular form. However, dissolved phosphorus species, including inorganic and organic (polyphosphates and orthophosphates), require biological or chemical methods for

removal. Depending on the pH of the water environment, orthophosphates can exist in various forms, such as $H_2PO_4^-$, H_3PO_4, PO_4^{3-}, or HPO_4^{2-} (Duenas et al., 2003). Table 1 summarizes the concentrations and main sources of phosphorus in different phosphate-rich wastewaters (Bacelo et al., 2020; Kunhikrishnan et al., 2022).

The main sources of phosphorus wastewater include the following: livestock processing wastewater, untreated wastewater, food processing wastewater, various industrial phosphorus-rich wastewater, and farm product processing wastewater. Industrial phosphorus-rich wastewater, such as wastewater discharged from an anodizing plant, contains high phosphorus concentrations (Table 1). The phosphorus concentration in municipal wastewater is typically below 20 mg/L (Bacelo et al., 2020). Phosphorus separation and concentration can generally be effectively achieved through biological, physical, or chemical methods, allowing for effective phosphorus management (Sengupta et al., 2015).

2.2. Summary of phosphorus management techniques in wastewater

The methods for the effective management of phosphorus in wastewater/water include coagulation, ion exchange, chemical precipitation, adsorption, biological treatment, and membrane separation (Bacelo et al., 2020). Adsorption is an effective method for managing low phosphorus concentrations in wastewater, and its mechanisms include electrostatic ligand exchange, surface precipitation, Lewis acid-base interactions, hydrogen bonding, physical adsorption, ion exchange, and electrostatic interactions, thereby increasing its effectiveness in phosphate management. High-performance adsorbents should have high phosphorus selectivity and adsorption capacity, high permeability to avoid blockage, resistance capability against corrosion and degradation during phosphorus desorption and adsorption processes, and a fast kinetic mechanism to promote the recovery and purification of high-quality phosphate (Kunhikrishnan et al., 2022). The most popular adsorbents currently include modified biochar, activated carbon, metal-based adsorbents, and metal–organic frameworks; however, these adsorbents have a high phosphate adsorption capacity, are costly, and easily cause secondary pollution (Almanassra et al., 2021).

Iron is environmentally friendly, abundant in the Earth's crust, and plays a crucial role in the phosphorus, oxygen, carbon, hydrogen, nitrogen, and sulfur cycles. This element is widely distributed in organisms, soils, and sediments, thereby increasing its importance (Wang et al., 2021a). Moreover, iron is a major trigger in the conversion of pollutants in the environment during oxidation–reduction processes (Wang et al., 2021a). Compared to metals such as La, Zr, Ce, Ca, Al, and others used for phosphate management, iron is economically efficient, easily accessible, and widely used in environmental remediation. In recent years, ICNs/mICNs have displayed effective phosphate management capability due to their large SSA and excellent surface physical and chemical properties (Wang et al., 2021a; Wang et al., 2023).

Table 1
The concentration of phosphorus in wastewater comes from various sources.

Wastewater sources	Total P (mg L^{-1})	Reference
Raw water from urban domestic sewage	5–20	(Davis, 2010; Kunhikrishnan et al., 2022)
Pig wastewater (original/primary lagoon/pre-treatment by lagoon)	52–987	(Bradford et al., 2008; Cheng et al., 2018; Kunhikrishnan et al., 2022; Vieira, 2007)
Abattoir wastewater	25–200	(Bustillo-Lecompte and Mehrvar, 2015; Kunhikrishnan et al., 2022)
Winery wastewater	3–188	(Kunhikrishnan et al., 2022; Mosse et al., 2011)
Wastewater from dairy processing industry	21–123	(Longhurst et al., 2000; Di and Cameron, 2002; Kunhikrishnan et al., 2022; Bradford et al., 2008; Longhurst et al., 2017)
Wastewater discharge from fruit and fruit canning plants	182	(Ammary, 2004; Kunhikrishnan et al., 2022)
Paper mill and pulp process wastewater	0.6–5.8	(Ammary, 2004; Cai et al., 2013; Kunhikrishnan et al., 2022)
Printing and dyeing wastewater	0–15	(Cai et al., 2013; Patel and Vashi, 2015; Kunhikrishnan et al., 2022; Santos and Boaventura, 2015)
Anodizing industrial process wastewater	620–5069	(Delgadillo-Velasco et al., 2018; Kunhikrishnan et al., 2022)
H_3PO_4 formation of wet process wastewater	15–31	(Grzmil and Wronkowski, 2006; Kunhikrishnan et al., 2022)
Fecal and urine wastewater	470–1070	(Kunhikrishnan et al., 2022; Randall and Naidoo, 2018)

3. Characteristics of ICNs

ICNs can be obtained from nature or synthesized in the laboratory (Jaiswal et al., 2013; Luther and George, 1991; Mora Mendoza et al., 2021; Niculescu et al., 2022; Wheeler et al., 2012). Natural ICNs are found on the Moon (Xian et al., 2023), on Mars (Di Bella et al., 2021), and in the Earth's aquatic sediments (Von Der Heyden et al., 2019), soil particles (Caraballo et al., 2022), and rocks (Notini et al., 2023). To date, approximately 300 natural ICNs have been discovered. ICNs can be divided into the following two types based on their elemental compositions: iron oxide minerals (IOMs) and iron sulfide minerals (ISMs) (Lai et al., 2021; Liu et al., 2014) (Fig. 1). Table 2 summarizes the physicochemical properties and crystal structures of various ICNs.

3.1. Synthesis of iron-containing nanominerals

Numerous studies on the application of ICNs in phosphate management have been conducted (Wang et al., 2021a; Wang et al., 2023). Several of these studies have demonstrated that laboratory-synthesized ICNs, including hematite, maghemite, goethite, magnetite, pyrite, pyrrhotite, lepidocrocite, ferrihydrite, and nano-zero-valent iron (NZVI), can effectively manage phosphate in wastewater through the adsorption process (Wang et al., 2021a; Wang et al., 2023). The synthesized ICNs in these laboratories are typically prepared using iron or sulfate salts through the following methods: (1) hydrolysis of acidic iron or sulfate salts in aqueous solution; (2) formation through a thermal dehydration process of iron oxides, iron sulfides, or iron hydroxides; (3) transformation of low crystallinity water ferrite into thermodynamically stable ICNs; (4) liquid-phase reduction using iron or sulfate salts; and (5) co-precipitation method using iron salts. These pathways have led to methods for synthesizing ICNs, including but not limited to solvothermal and hydrothermal methods, liquid-phase reduction, precipitation, electrochemical deposition, and sol–gel methods (Tan et al., 2022). However, some laboratory-synthesized ICNs are not easily scalable for practical applications due to their high cost (Wang et al., 2021a; Wang et al., 2023). By contrast, natural ICNs are more accessible and cost-effective, demonstrating remarkable potential for phosphate management.

3.2. Natural iron oxide minerals

Oxide-containing ICNs on Earth include amorphous and crystalline types of IOMs (Lai et al., 2021). Among the IOMs, ferrihydrite (Antelo et al., 2015), magnetite (Yoon et al., 2014), maghemite (Makie et al., 2011), siderite (Balboni et al., 2020; Zhang et al., 2017a), lepidocrocite (Liao et al., 2020), goethite (Parfitt et al., 1976), hematite (Elzinga and Sparks, 2007), and limonite (Chen et al., 2022b) are used in phosphate management.

Most existing iron on Earth is in the form of iron–magnesium minerals. Weathering dissolves the minerals to form iron oxides (hydroxides), thereby releasing iron deposits. Consequently, natural iron minerals occur as iron oxide and hydroxide minerals (Fig. 1) and typically exist in trivalent form (Cornell and Schwertmann, 2003), with the exception of magnetite, which contains divalent iron. Fe—O is ionically

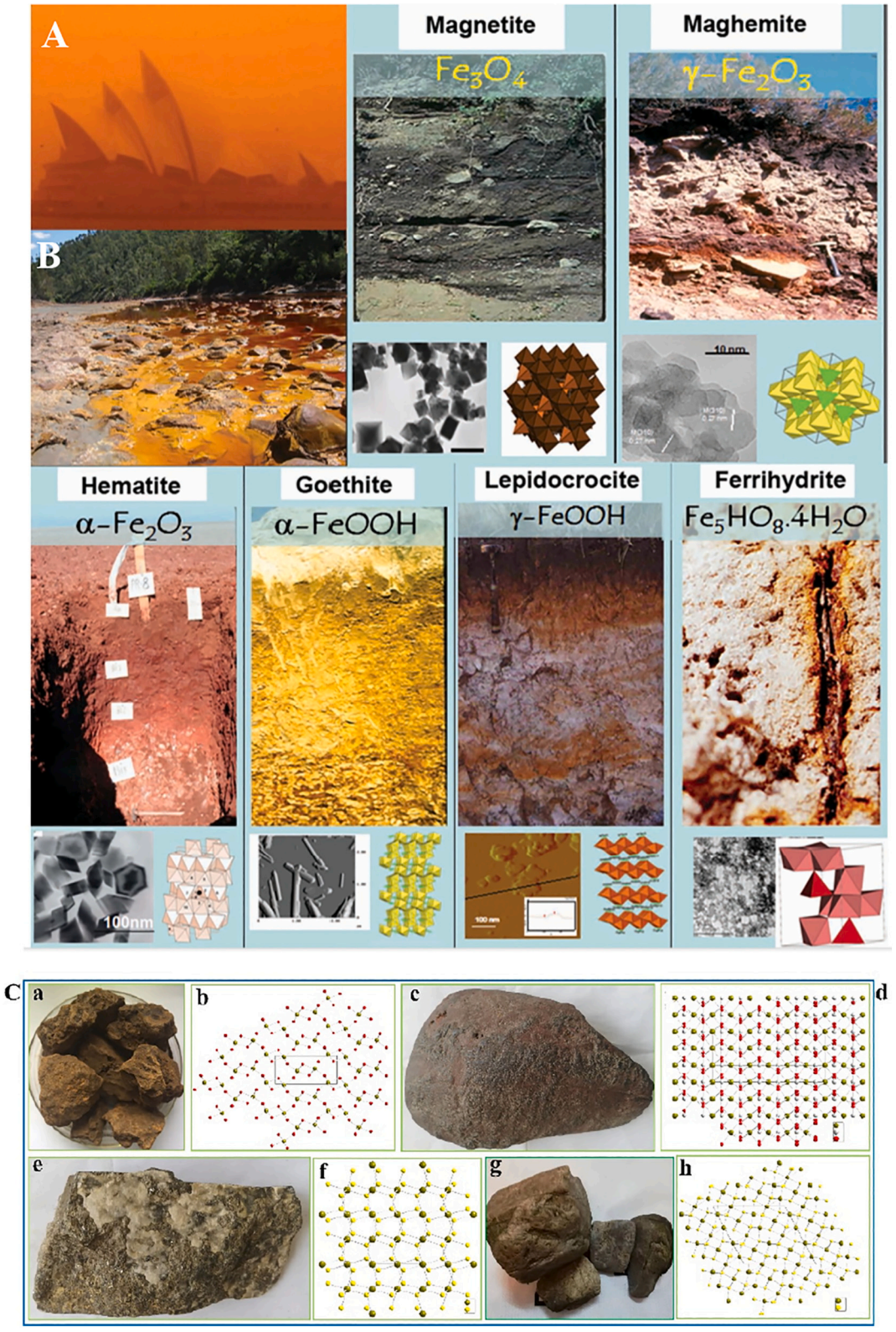

Fig. 1. (A) Sydney Opera House exposed to iron oxide dust (Tartaj et al., 2011); (B) iron oxide precipitation sample taken from Rio Tinto water in southwestern Spain (Tartaj et al., 2011); (C) different forms and crystal structures of ICNs: (a) image of limonite; (b) crystal structure of limonite; (c) image of siderite; (d) crystal structure of siderite; (e) image of pyrite; (f) crystal structure of pyrite; (g) image of pyrrhotite; (h) crystal structure of pyrrhotite. (Note: limonite, siderite, pyrite, and pyrrhotite come from Tong Ling City, Anhui Province, China).

Table 2
Overview characteristics of different types of ICNs.

	Iron-containing nanominerals								
	Goethite	Lepidocrocite	Hematite	Ferrihydrite	Maghemite	Magnetite	Siderite	Pyrite	Pyrrhotite
Chemical formula	a-FeOOH	γ-FeOOH	α-Fe_2O_3	$Fe_5HO_8{\cdot}4H_2O$	γ-Fe_2O_3	Fe_3O_4	$FeCO_3$	FeS_2	$Fe_{1-x}S$
Crystal system	Orthorhombic system	Orthorhombic system	Trigonal system	Trigonal system	Isometric system	Isometric system	Trigonal system	Isometric system	Hexagonal crystal system
Cell size/Å	$a_0 = 9.956$ $b_0 = 3.0215$ $c_0 = 4.608$	$a_0 = 12.52$ $b_0 = 3.873$ $c_0 = 3.071$	$a_0 = b_0 = 5.034$ $c_0 = 13.752$	$a_0 = b_0 = 5.08$ $c_0 = 9.4$	$a_0 = b_0 = c_0 = 8.4053$	$a_0 = b_0 = c_0 = 8.39$	$a_0 = b_0 = 4.979$ $c_0 = 14.064$	$a_0 = b_0 = c_0 = 5.42$	$a_0 = b_0 = 3.49$ $c_0 = 5.69$
Specific gravity /g/cm^3	4–4.4	4.1	5.3	3.96	4.88	4.9–5.2	3.7–4.0	4.9–5.2	4.6–4.7
Color	Tawny	Reddish brown	Blue gray	Red brown	Brown	Brown	Gray	Yellow brown	Brown
Shape	Acicular kidney	Flaky	Kidney oolitic	Spherical nanoparticles	Granular aggregates	Granular lumpy	Spherical gel	Stalactite radial	Columnar hexagonal plate
Octahedral occupancy	1/2	1/2	2/3	<2/3	–	–	–	–	–
Maximum aluminum substitution	1/3	+	1/6	n.k.	+b	+	–	–	–
Space group	Pnma	Bbmm	R-3c	P31c P3	$P4_332$ $P4_12_12$	Fd3m	R-3c	Pa3	A2/a
Close-packed anions	ABAB [001]	ABCABC [015]	ABAB [001]	ABAB [001]	ABCABC [111]	AB2O4	–	–	–
Standard free energy (ΔG°)	−488.6	−477.7	−724.8	−699.0	−711.14	−1016.1	−27.3	n.k.	n.k.
Solubility product (pFe + 3pHOH)	43.3–44	40.6–42.5	42.2–43.3	37–39.4	40.5	n.k.	n.k.	n.k.	n.k.
Magnetic	Diamagnetism	Diamagnetism	Weak magnetic	Paramagnetism	Magnetic	Magnetic	Weak magnetic	Weak magnetic	magnetic
Neel/K	400	77	955	25–115	n.k	850	n.k	n.k	n.k
Hardness	5–51/2	5	61/2	n.k.	5	5–6	3.75–4.25	6–6.5	3.5–4.5
References	(Liu, 2013; Liu et al., 2014)	(Liu, 2013; Liao et al., 2020)	(Liu, 2013; Makie et al., 2011)	(Liu, 2013; Tüysüz et al., 2008)	(Liu, 2013; Tartaj et al., 2011)	(Liu, 2013; Kodama, 1999)	(Liu, 2013; Xing et al., 2017)	(Liu, 2013; Moslemi and Gharabaghi, 2017)	(Liu, 2013; Zhu et al., 2018)

bonded, and its coordination number is determined by the sizes of the oppositely charged ions. The main coordination forms of iron (which has a small ionic radius) are octahedral and tetrahedral (Tsujimoto et al., 2007). The Fe3d electronic configuration of IOMs determines their electronic properties and magnetism. The electrostatic field of the ligand can divide the crystal structure configuration of five d-orbitals, resulting in Fe-d-orbitals with different energies (O_2^-/OH^-) and ICNs with various thermodynamic properties. For example, Fe^{3+} has no octahedral or tetrahedral coordination preference, whereas Fe^{2+} occupies octahedral sites. Thus, ICNs take numerous forms in the environment, ranging from highly crystalline (magnetite, maghemite, hematite, and goethite) to weakly crystalline IOMs (six-line ferrihydrite [6LFh], two-line ferrihydrite [2LFh], and limonite) (Tartaj et al., 2011). Highly crystallized magnetite is the optimal IOM phase in Fe^{2+}-rich environments, whereas goethite and hematite minimize the thermodynamic and energy values in the Fe_2O_3–H_2O system (Tsujimoto et al., 2007).

Hematite and corundum exhibit similar crystal structures, in which the O_2^- anions compactly assemble into hexagonal arrangements and the Fe^{3+} cations occupy two-thirds of the octahedral pores. Compared to the {001} facets, the SEM images and schematics of different facets of hematite (Huang et al., 2017) indicate that the Fe5c sites on the {012} facets have lower affinity for phosphate, as shown in (Fig. 2 and Fig. 3), respectively. This finding is attributed to the strong steric hindrance on the {012} facets of hematite, which inhibits the formation of phosphate complexes due to numerous undercoordinated iron cations. Additionally, compared to exposed {001} facets of nanosheets, hematite nanorods with exposed {110} and {001} facets exhibit superior ferrous ion confinement, thereby substantially promoting phosphate complexation (Fig. 2 and Fig. 3A, B and C) (Huang et al., 2016). The polar {110} facets can use a five-coordinate binding mode to restrict higher density ferrous ions, thereby more effectively reducing complexes with phosphate energy spans than nonpolar {001} facets (Fig. 3A, B and C).

In goethite, a common IOM in soil, half of the octahedral pores are occupied by Fe^{3+} cations, and the OH^-/O_2^- anions are arranged along the {100} orientations, forming a compact hexagonal stacked lattice (Tartaj et al., 2011). The hydroxyl group in goethite depends on the change in coordination number between the adjacent Fe^{3+} and O_2^- ions (Fig. 3D) (Echigo et al., 2012). C- and B-type hydroxyl groups cannot donate or accept electron pairs, whereas A-type hydroxyl groups can donate and accept protons. The D-type hydroxyl groups are Lewis acid sites (Fe^{3+}–H_2O) found on goethite surfaces. Goethite possesses an electrophilic D-type hydroxyl group with a certain affinity for phosphate because the positively charged goethite surface attracts negatively charged phosphate ions (Fig. 3D) (Echigo et al., 2012).

Limonite is a multimineral aggregate of aphanitic goethite with small amounts of pyrite, magnetite, illite, and siderite (Fig. 1C[a] and [b]) (Chen et al., 2022b). Lepidocrocite crystals possess a cubic, close-packed OH^-/O_2^- ion structure in which the Fe^{3+} cations form iron octahedral sheets and the layers are connected through hydrogen bonds (Tsujimoto et al., 2007). Magnetite and maghemite exhibit cubic anti-spinel crystal structures of oxygen and iron atoms, respectively. The O_2^- ions form a tightly packed cubic crystal structure, while the Fe^{3+} cations occupy the octahedral and tetrahedral positions in the pores. Different from magnetite, most or all of the iron atoms in maghemite are in the Fe^{3+}

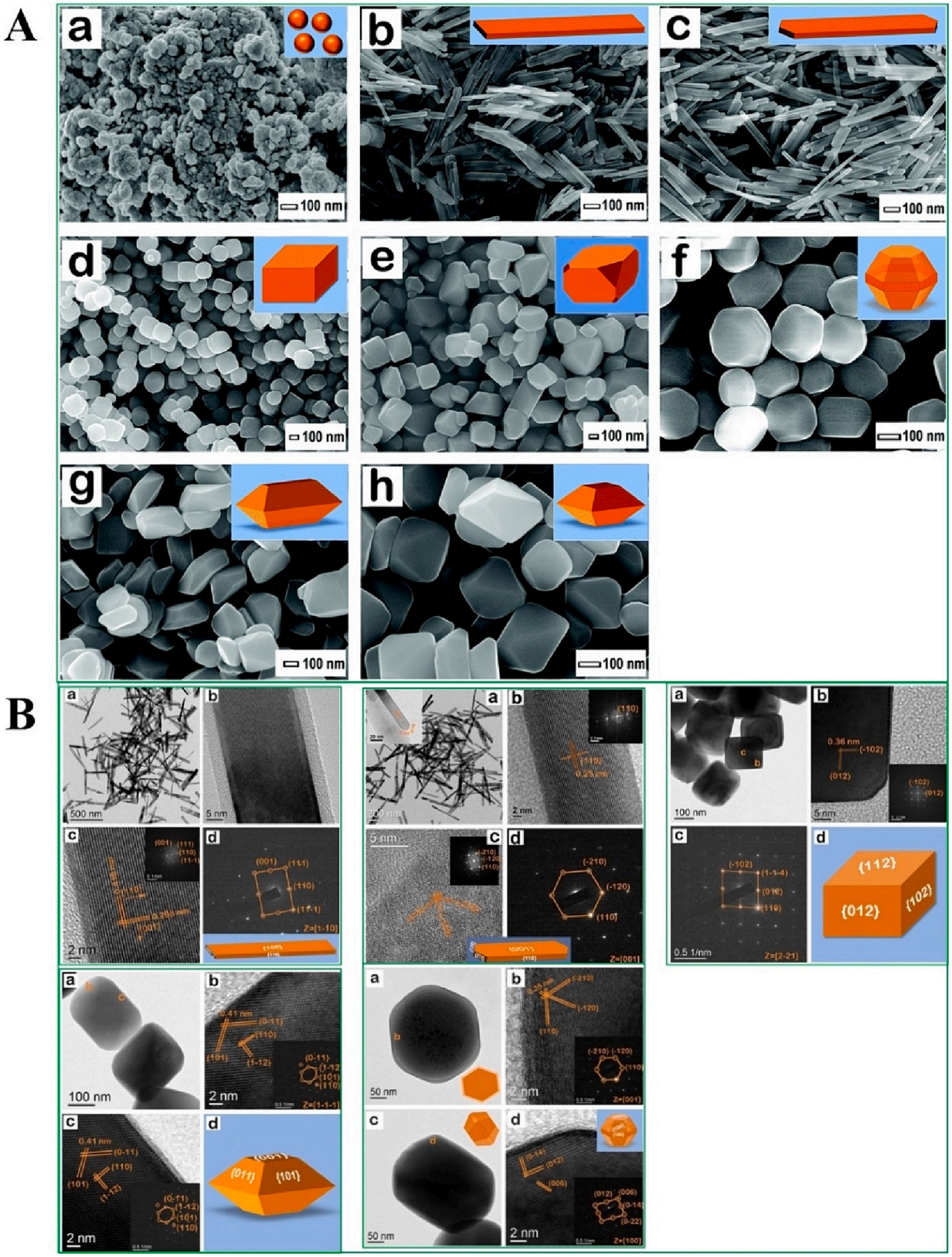

Fig. 2. (A) SEM and TEM (B) images of goethite nanocrystals and hematite nanocrystals with different facets (Patra et al., 2016).

state, and the ionic vacancies are compensated with Fe^{2+} oxidation (Kodama, 1999).

Ferrihydrite has a pronounced weak crystallinity, displaying a high SSA and reactivity, thereby playing a remarkable role in the migration and transformation of geochemical elements. Ferrihydrite exists in different crystalline forms, from weakly crystallized 2LFh quasi-amorphous solids to highly crystallized 6LFh (Michel et al., 2010; Tüysüz et al., 2008). Siderite comprises alternating hexagonal CO_3^{2-} and

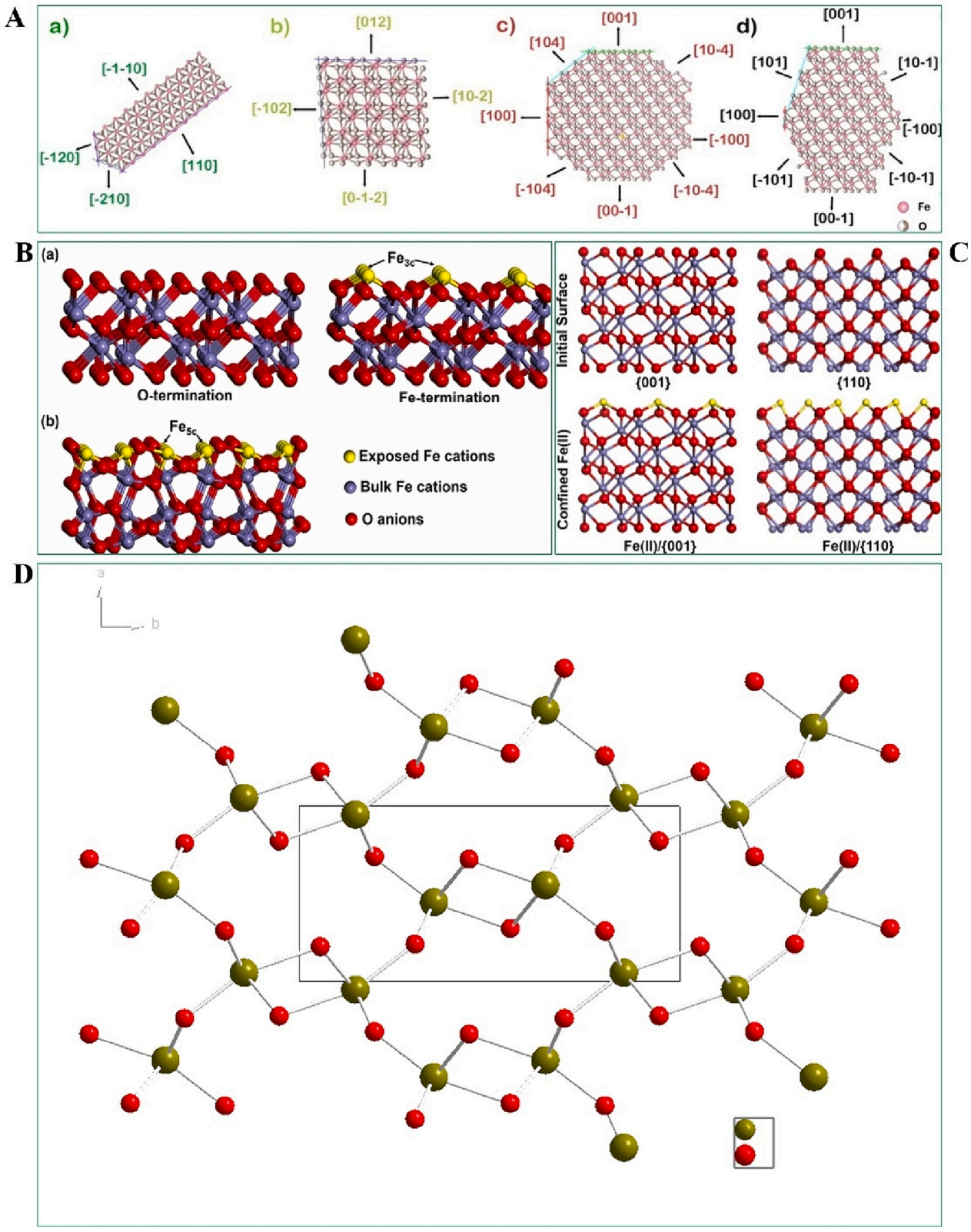

Fig. 3. (A) Schematic of different facets and their growth directions of hematite along (Patra et al., 2016); (B) schematic of the atomic arrangement of hematite has exposed {001} and {012} facets. {001} (a) and {012} (b) facets (Huang et al., 2017); (C) schematic of Fe(II) on the surfaces of hematite {001} and {110}. Red, blue, and yellow spheres represent O atoms, large Fe atoms, and restricted Fe atoms on the surface, respectively (Huang et al., 2016); (D) schematic of positions of the hydroxyl groups on goethite. Red spheres represent O atoms, chartreuse spheres represent Fe atoms.

octahedral Fe^{2+} layers. The hexagonal CO_3^{2-} layers form a typical octahedral eight-coordination structure (Fig. 1C[c] and [d]) (Farfan et al., 2012).

3.3. Natural iron sulfide minerals

Pyrite is an ISM containing octahedral FeS_6 units and S—S dimers (Fig. 1C[e] and [f]). The Fe—S bond distances inside the FeS_6 octahedron match those on the surface. However, three Fe atoms align with each S atom and one other S atom to form a tetrahedral coordination with paired S centers known as S_2^{2-} centers. The S—S bond is weak and easily broken, which is potentially beneficial for phosphate management (Moslemi and Gharabaghi, 2017). The three-dimensional structure of pyrrhotite can be artificially constructed from twisted octahedral FeS_6 units. The crystal structure units share their edges with adjacent FeS_6 layers units in *a* or *c* facet orientations (Fig. 1C[g] and [h]) (Yu et al., 2016).

Overall, the following findings are observed: (1) weakly crystalline ferrihydrite has a large SSA and active sites, showing affinity toward phosphate, thereby playing a crucial role in the biogeochemical cycling of iron and phosphate. (2) Magnetite is a stable ICN with strong ferromagnetic properties, serving as a potential adsorbent for phosphate management. (3) Goethite contains four types of hydroxyl groups, exhibiting high affinity toward phosphate. The modification of ICNs is generally necessary to enhance their SSA, isoelectric point, surface active groups, and stability for improved affinity toward phosphate.

4. ICNs and mICNs for phosphate management

4.1. ICNs for phosphate management

4.1.1. Iron sulfide minerals

The oxidation–reduction reaction of pyrite (Fig. 4A) and pyrrhotite (Fig. 4B) links the chemical valence transitions of sulfur and iron elements, thereby achieving elemental geochemical cycling. The oxidation–reduction reaction of pyrite occurs on different facets. The initial oxidation reaction rate is higher on the {111} and {210} facets than on the {100} facet. Meanwhile, under low-humidity conditions, the reaction rate is higher on the {210} facet than on the {111} facet. These differences in reactivity can be attributed to the varying sensitivities of different facet structures to oxidation reactions. The {111} facet displays the highest structural sensitivity to oxidation reactions. On the relatively inert {100} facet, the reaction rate is 10^{-2} to 10^{-3} times lower than on the {111} and {210} facets (Zhu et al., 2018) (Fig. 4C and D, respectively). Notably, pyrite and pyrrhotite are efficient phosphate removal adsorbents because they dissolve iron ions in aerobic environments. Wang et al. and Li et al. (Li et al., 2013; Wang et al., 2012) reported phosphate adsorption amounts of 0.12 and 0.42 mg/g on pyrite and pyrrhotite, respectively. The analysis above reveals the following: (1) Pyrite and pyrrhotite can cause environmental pollution, such as acid mine drainage. (2) Pyrite and pyrrhotite generally have a low removal ratio for phosphate. Thus, modifying pyrite and pyrrhotite is necessary to further enhance their affinity for phosphate.

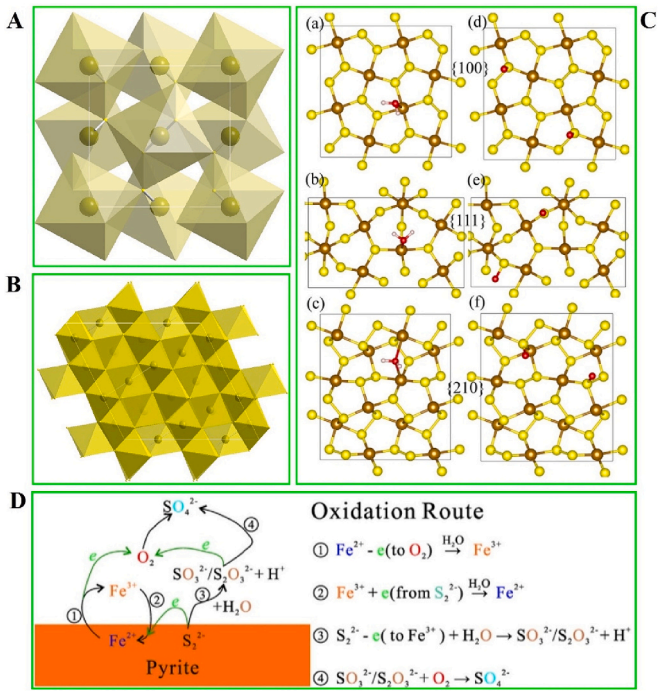

Fig. 4. (A) Crystal structure model of pyrite; (B) crystal structure model of pyrrhotite; (C) schematic of adsorption configurations of relaxed water (a–c) and oxygen (d–f) on the {100}, {111}, and {210} facets of pyrite. The yellow, brown, red, and pink spheres represent S, Fe, O, and H atoms, respectively (Zhu et al., 2018); (D) schematic showing the oxidation path of pyrite in air (Zhu et al., 2018).

4.1.2. Iron oxide minerals

4.1.2.1. Goethite. Phosphates can be adsorbed onto goethite with different degrees of crystallinity and SSA (Wang et al., 2021a; Wang et al., 2023). The crystallinity of goethite influences phosphate adsorption. Reports have indicated that the adsorption capacity of phosphate by highly crystalline goethite is 13.65 mg/g (Zhang et al., 2021a). For example, the hydroxyl active sites on the surface of δ-FeOOH removed 94.1 % of the phosphate at pH = 3, mainly through surface precipitation and electrostatic adsorption (Fig. 5A) (Li et al., 2019a). The goethite contains three isostructural polymorphs, including lepidocrocite, akaganeite, feroxyhyte, which also exhibit phosphate removal capabilities (Chitrakar et al., 2006). Goethite (with a higher PZC = 9.5 than akaganeite) maintains a positively charged surface at pH = 3; therefore, its adsorption capacity for phosphate exceeds that of akaganeite (Chitrakar et al., 2006). For example, Kim et al. (2011) reported the maximum phosphate adsorption capacities of goethite, akaganeite, and lepidocrocite as 0.266, 0.450, and 0.265 mmol/g, respectively (notably, akaganeite has the highest phosphate adsorption capacity). Natural goethite mainly exists in limonite, which also demonstrates a certain capability in phosphate management. The phenomenon of Al substitution in limonite leads to a low crystallinity of limonite. This condition reduces the phosphate adsorption capacity of limonite per unit area while simultaneously increasing the phosphate adsorption capacity of limonite per unit mass (Torrent et al., 1994; Wang et al., 2023).

4.1.2.2. Hematite. Hematite has the characteristics of large SSA, small particle size, and high reactivity, playing a key role in the migration and transformation of phosphate. Hematite surfaces exhibit abundant active adsorption sites, where phosphates can produce different forms of complexes with hematite, such as deprotonated and protonated bidentate complexes. The particle size of hematite considerably affects its adsorption of phosphates, demonstrating high surface adsorption site density and large surface heterogeneity, which lead to the strong adsorption capacity of phosphates by hematite (Wang et al., 2023). Previous studies have reported that the phosphate uptake capacity of hematite with different morphologies and crystal sizes ranges from 0.31 μmol/m^2 to 2.72 μmol/m^2 (Colombo et al., 1994). However, hematite exhibits a lower phosphate adsorption affinity than goethite (Barrón and Torrent, 1996). The absorbed phosphate amount decreases when hematite flattens along the *c*-axis direction relative to the *a*-axis direction. Therefore, a flat hematite facet has a low average affinity for phosphate, implying that the main phosphate-adsorbing facets of hematite are not

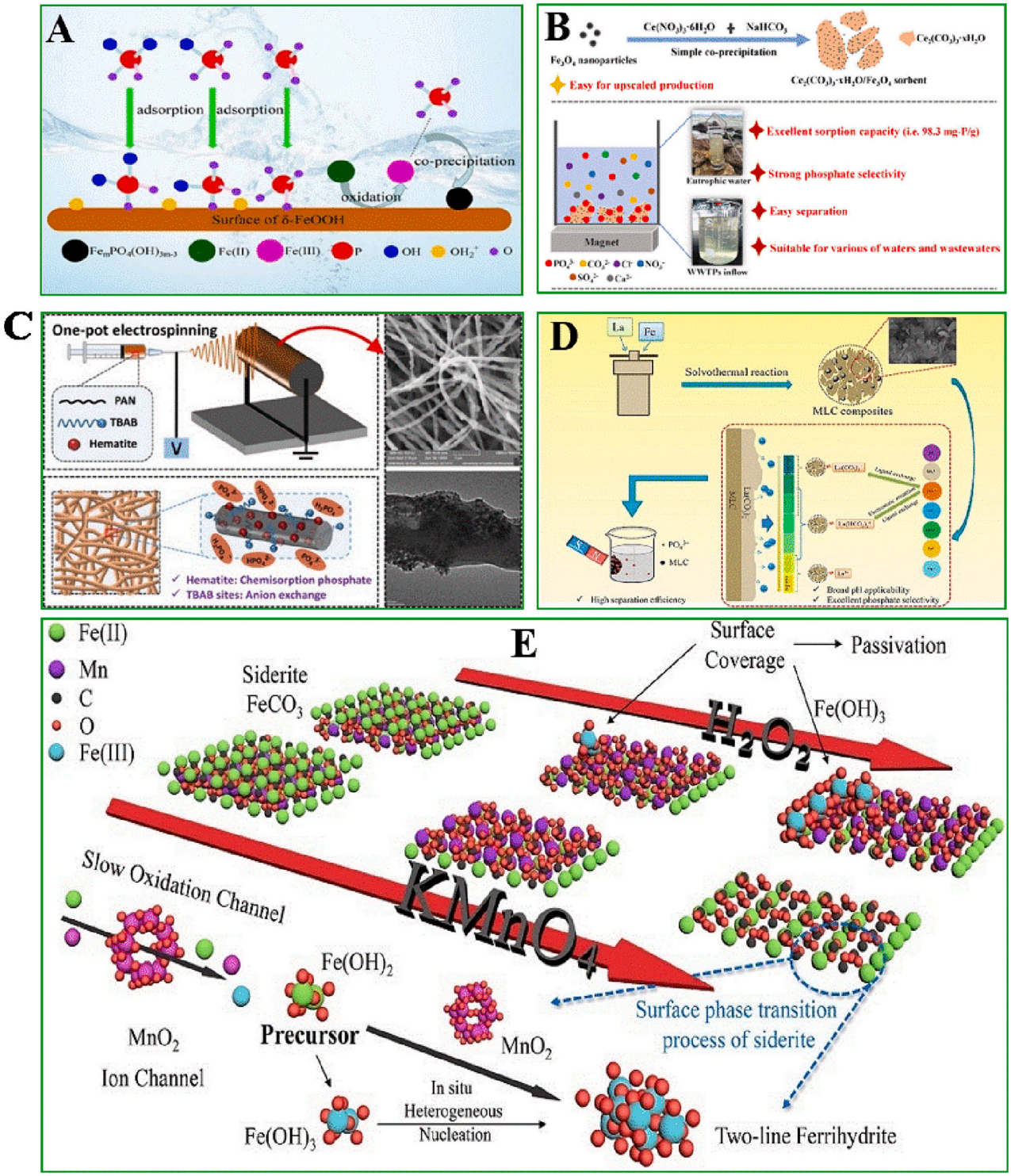

Fig. 5. (A) Schematic of the synergistic phosphate removal mechanism of δ-FeOOH/Fe(II) (Li et al., 2019a); (B) schematic of modification process and phosphate removal mechanism of $C_3Ce_2O_9{\cdot}xH_2O$ modified magnetite (Shan et al., 2021); (C) schematic of modification process and phosphate removal mechanism of polyacrylonitrile- and tetra-n-butylammonium bromide modified hematite (Wang et al., 2021b); (D) schematic of modification process and phosphate removal mechanism of $NaLa(CO_3)_2$ modified magnetite (Hao et al., 2019); (E) schematic of the transformation process of the crystal structure of siderite modified by $KMnO_4$ or H_2O_2 (Xing et al., 2022).

the basal facets (Barron et al., 1988; Barrón and Torrent, 1996; Barrón et al., 1997). However, compared to raw hematite, modified hematite shows a higher affinity for phosphate. For example, Liang et al. (2016) synthesized mesoporous α-Fe_2O_3 nanoparticles on cellulose nanocrystal templates. They reported a phosphate adsorption capacity of 5.7 (mg/g), an SSA of 106.9 m^2/g, and an ion-exchange adsorption mechanism.

4.1.2.3. Ferrihydrite. Ferrihydrite has a high affinity for phosphate. Owing to its high surface activity and SSA (200–610 m^2/g), ferrihydrite is crucial in phosphate management (Yang et al., 2020a). For example, Mallet (Mallet et al., 2013) and Ma (Ma et al., 2021) demonstrated that the 2LFh form of ferrihydrite adsorbs 104.8 and 22.55 mg/g of phosphate, respectively. Ferrihydrite exhibits different crystallinities under

various synthesis conditions and captures phosphate by electrostatic ligand exchange and electrostatic adsorption, respectively (Mallet et al., 2013; Ma et al., 2021).

4.1.2.4. Magnetite. With a large SSA and strong magnetism, magnetite is easily magnetically separated and has a certain adsorption capacity for phosphates (Hao et al., 2019). For example, the phosphate absorption capacities of abandoned tailings containing iron oxide (mainly nano-Fe_3O_4) and synthesized nano-Fe_3O_4 are 8.6 mg/g (Zeng et al., 2004) and 24.4 mg/g (Moharami and Jalali, 2014), respectively. The phosphate adsorption mechanisms are electrostatic adsorption and surface precipitation (Moharami and Jalali, 2014). Magnetite can serve as a material for phosphate removal, revealing its potential to scale up its use for magnetic recovery and effective management of phosphate. However, Fe^{2+} in the crystal structure of magnetite is prone to oxidation (Hao et al., 2019). Modifying the magnetite is essential to enhancing the corresponding phosphate management capability of the magnetite.

4.1.2.5. Siderite. Siderite, an important iron-containing carbonate mineral in nature, is rich in resources and is crucial in the iron–carbon cycle in nature (Zhang et al., 2017a). Siderite can fix phosphates in a stable manner due to its high chemical oxidation and thermal decomposition activity. Zhang et al. (2017a) demonstrated a phosphate adsorption amount of 0.0835 mg/g for siderite. The phosphate adsorption by siderite is realized through electrostatic adsorption and electrostatic ligand exchange because siderite undergoes hydrolysis on its surface, forming iron-containing hydroxides. However, siderite has a low affinity for phosphate due to its stable structure. Therefore, siderite must be modified to improve its affinity.

4.2. mICNs for phosphate management

Several chemical elements, such as Zn, Al, Ce, La, Mn, and Zr, have been employed for the modification of ICNs to enhance their affinity for phosphates (Belloni et al., 2023; Fu et al., 2018; Li et al., 2016b; Shan et al., 2021). The reports currently focus on the modification of ICNs using different metal elements and modification methods; for instance:

(1) impregnation modification (Li et al., 2016b);

(2) modification by calcination in different atmospheres (N_2, O_2, and H_2) (Chen et al., 2015; Liu, 2013; Liu et al., 2013a; Liu et al., 2013b; Xing et al., 2017);

(3) co-precipitation modification (Moharami and Jalali, 2014);

(4) solvothermal modification (Song et al., 2020);

(5) hydrothermal modification (Farfan et al., 2012);

(6) electrochemical modification (Chen et al., 2021a); and.

(7) co-pyrolysis of the biomass and ICNs (Zhang et al., 2020a).

Impregnation is currently the most commonly used modification method for ICNs (Li et al., 2016b). This method involves mixing metallic elements with ICNs and allowing them to react for a certain period of time or at a certain temperature. However, the impregnation method for modifying ICNs is generally a time-consuming and material-intensive task (Li et al., 2016b).

The surface physical and chemical properties of ICNs, such as SSA, surface charge, surface functional groups, and pore size, can be altered by using different metal elements to modify ICNs. However, considering the types of modified ions, the SSA of modified ICNs may exhibit different variation trends (Belloni et al., 2023; Fu et al., 2018; Li et al., 2016b; Shan et al., 2021). Numerous studies have shown that metal ions can block the pore or channel structure of ICNs, thereby reducing porosity and SSA after modification. However, other studies reveal an enhancement in SSA and porosity, leading to the creation of additional active sites in the modified ICNs. Regardless of increments or reductions in SSA of modified ICNs, modified ICNs can effectively enhance their affinity for phosphate (Belloni et al., 2023; Fu et al., 2018; Li et al., 2016b; Shan et al., 2021). Compared to ICNs, all metal ions used for modification increase the PZC of modified ICNs to a certain pH value and/or decrease their negatively charged surface, thus enhancing the adsorption capacity of modified ICNs for phosphate. Table 3 summarizes modified ICNs and their advantages and disadvantages.

4.2.1. Modification by calcination in different atmospheres

Modified ICNs have been calcined under different H_2, O_2, and N_2 atmospheres, yielding calcined products with higher SSA, porosity, and active site than the raw ICNs (Liu, 2013; Cheng et al., 2017; Xing et al., 2017). Notably, O_2-calcined ICNs (limonite, siderite, and goethite) lose their structural, crystal, and adsorption water through evaporation, which then increases their SSA, active sites, and porosity by reducing the number of hydroxyl groups (Cheng et al., 2017; Liu et al., 2013a; Xing et al., 2017). N_2-calcined ISMs have also been obtained (pyrite [Chen et al., 2015] and pyrite mixed goethite [Chen et al., 2016]). Sulfur volatilization from the crystal structure transforms pyrite into monoclinic and hexagonal pyrrhotite with an increased SSA, active sites, and porosity. H_2 calcination is used to obtain the calcination products of ICNs, which increase the number of active sites, SSA, and porosity. More importantly, this method reduces the standard electrode potential in ICNs (goethite, siderite, limonite, and magnetite) (Liu et al., 2013b; Zhao et al., 2021; Zhao et al., 2021a; Zhang et al., 2017). Zeta potential is a crucial indicator. Unfortunately, zeta potential is not monitored for these calcined products; therefore, some relevant conclusions can only

Table 3
Modification methods of ICNs its advantages and disadvantages.

Modification method	Advantage	Disadvantage	References
$H_2/O_2/N_2$ calcined modified ICNs	◇ Increased SSA; active sites; Zeta; porosity, ◇ Fe—O functional group;	◇ H_2 expensive; explosion; ◇ Produces SO_2, CO and CO_2; biomass tar;	(Liu et al., 2013b; Cheng et al., 2017; Chen et al., 2015)
Biochar modified ICNs	◇ Magnetically recycle	◇ Energy loss; Dehydroxylation; ◇ Destroying structure of biochar;	(Zhu et al., 2020; Zhang et al., 2020a)
Aluminum substitution modified goethite	◇ Increased the thermal stability; SSA, Zeta; OH groups; ◇ Needle to granular; ◇ Decreased the unit cell parameters; aspect ratio, crystallinity; Fe-Fe (Al) distance	◇ Passivated of Al-hematite facet (001) ◇ Increases dissolved Al; ◇ Decreased biodiversity and harming fish;	(Li et al., 2016b; Li et al., 2016c; Liao et al., 2020)
Aluminum substitution modified hematite	◇ Decreased lattice parameters; crystalline; ◇ Increased crystal size, SSA, structure water; ◇ Rhombic to plate		
Aluminum substitution modified lepidocrocite	◇ Decreased aspect ratio; coherent scattering domain sizes of facet (020); ◇ Crystals became thinner; ◇ Facets ratio of (200)/(002); ◇ Increase of OH groups; phosphate adsorption density		
Lanthanum/cerium modified ICNs	◇ Increased of active sites; Zeta; SSA; ◇ Organophilicity	◇ Toxic; ◇ Increase cost; ◇ Secondary pollution	(Shan et al., 2021; Fu et al., 2018)

be drawn based on the adsorption capacity of phosphate (Table 4). The above analyses show that calcination improves the activity of modified ICNs, enhancing their affinity for phosphate. The phosphate removal mechanisms of H_2-, O_2-, and N_2-calcined ICNs are electrostatic adsorption, surface precipitation, and surface complexation, respectively.

For example, Xing et al. (2017) reported that the transformation of siderite to hematite began during the calcination of siderite at 450 °C in O_2, followed by the release of a large amount of CO_2, forming a considerable amount of mesopores with sizes ranging from 1 nm to 5 nm. The maximum SSA of siderite calcined at 470 °C in O_2 was 57.5 m^2/g, and the adsorption capacity of phosphate was 9.24 mg/g. Chen et al. (2015) showed that N_2-calcined pyrite has a larger SSA (10 m^2/g) than natural pyrrhotite and reduces the phosphate concentration to below 0.02 mg/L after purification. Zhao et al. obtained H_2-calcined magnetite (SSA: 19 m^2/g), siderite (SSA: 15.3 m^2/g), and hematite (SSA: 15.1 m^2/g). The H_2-calcined magnetite demonstrated a large adsorption phosphate volume (13.45 mg/g) because magnetite is rich in iron (87.4 % Fe_2O_3) (Zhao et al., 2021). Other researchers have synthesized O_2-calcined limonite (Cheng et al., 2017), O_2-calcined goethite (Liu et al., 2013a), and N_2-calcined goethite mixed with pyrite for phosphate removal (Chen et al., 2016). The adsorption capacity of phosphate ions through the thermal decomposition products of goethite and pyrite obtained from N_2 calcined is 27.3 mg/g (Chen et al., 2016).

4.2.2. Biochar-modified ICNs

The SSA, numbers of functional groups and active sites, PZC, porosity, and adsorption efficiency of ICNs can be improved by coprecipitation impregnation and biochar modification of ICNs (magnetite, hematite, goethite, and ferrihydrite) (Zhang et al., 2020a; Zhang et al., 2021b; Zhu et al., 2020). For example, Zhang et al. reported large SSAs (64–691 m^2/g) in biochar-modified ICNs (Zhang et al., 2020a). At pH = 2, the phosphate adsorption volumes of biochar-modified ferrihydrite, goethite, magnetite, and hematite reached 18.49, 22.14, 9.408, and 13.81 mg/g, respectively. The differences can be attributed to the different PZCs of the mICNs, which ranged from 2.48 to 3.27 in biochar-modified magnetite and goethite, respectively. These findings are consistent with the PZCs of biochar-modified ICNs (Zhang et al., 2020a). Zhao et al. found that biochar-modified magnetite prepared via coprecipitation can immobilize water-soluble phosphate released from fresh biomass (Zhao et al., 2021). Biochar-modified goethite prepared

Table 4
Adsorption of phosphate by different type of adsorbents.

Type of adsorbent	Adsorbents	Q_m (mg/g)	Experimental conditions (adsorbent dosage; initial P concentration range; temperature; pH)	Mechanism	References
Natural ICNs	Siderite	0.0835	0.0125 to 0.25 mg/L; 20 mg/L; 30 °C; pH of 6	EA; ELE; SP;	(Zhang et al., 2017a)
	Pyrrhotite	1.15	40 g/L; 0 to 80 mg/L; 21 °C; pH of 5.81	EA; ELE; SP	(Li et al., 2013)
	Pyrite	0.00682	250 g/L; 2 mg/L; 25 °C; pH of 6.5	EA; ELE; SP	(Zhang et al., 2013)
	Limonite	0.5	1 g/L; 0.5 to 3 mg/L; 25 to 45 °C; pH of 3 to 9	EA; ELE; SP	(Cheng et al., 2017)
Modified natural ICNs	O_2 calcination limonite	0.916	1 g/L; 0.5 to 3 mg/L; 25 to 45 °C; pH of 3 to 9	EA	(Cheng et al., 2017)
	O_2 calcination siderite	9.24	2 g/L; 5 to 100 mg/L; 30 °C; pH of 6.5	EA; ELE; SP	(Xing et al., 2017)
	Ferrihydrite and La co-modified with magnetite	35	1 g/L; 2 to 120 mg/L; 25 °C; pH of 7.4	EA; ELE; SP	(Fu et al., 2018)
	$KMnO_4$ modification siderite	13.04	0.5 g/L; 5 mg/L; 45 °C; pH of 7	EA; ELE; SP	(Xing et al., 2022)
	H_2O_2 modification siderite	3.28			
	Magnetite modification pyrite	24.8	2.5 g/L;10 mg /L; 25 °C; pH of 3	EA; ELE; SP	(Cai et al., 2019)
	H_2 calcination limonite	16	0.5 g/L;10 mg/L; 25 °C; pH of 6.3	EA; ELE; SP	(Zhang et al., 2017)
	H_2 calcination siderite	9.66	1 g/L; 0.25 to 20 mg/L; 25 ± 2 °C; pH of 6	EA; ELE; SP	(Zhao et al., 2021)
	H_2 calcination hematite	3.86			
	H_2 calcination limonite	7.72			
	H_2 calcination limonite	12.18			
	H_2 calcination magnetite	13.45			
Laboratory synthesis ICNs	α-FeOOH	10	1 g/L; 50 mg/L; pH of 7.8; 25 °C	EA; SC	(Chitrakar et al., 2006)
	Hematite	1.75	10 g/L; 3 to 20 mg/L; pH of 3.39; 25 °C	SC	(Huang, 2004)
	Nano zero valent iron	245.65	1 g/L; 10 mg/L; pH of 3 to 12; 25 °C	EA; SP	(Wen et al., 2014)
	Fe_3O_4	24.4	1 g/L; 50 mg/L; pH of 2 to 8; 25 °C	EA; SP	(Moharami and Jalali, 2014)
	Ferrihydrite	66.7	1 to 12 g/L; 200 to 1000 mg/L; pH of 7; 15 to 55 °C	EA; SP	(Ajmal et al., 2018)
	Magnetite	57.8			
	Goethite	50.5			
	$La(OH)_3$ modified magnetite	19.34	0.2 g/L; 0 to 15 mg/L; 25 °C; pH of 7 ± 0.02	EA; ELE	(Song et al., 2020)
	Polyacrylonitrile- and tetra-n-butylammonium bromide co-modified hematite	8.76	1 g/L; 2 to 20 mg/L; 23 °C; pH of 5.6	EA; ELE	(Wang et al., 2021b)
	Humic acid modified magnetite	28.9	1 g/L; 0.05 to 100 mg/L; pH of 6.6; 25 °C	EA; ELE; SP	(Rashid et al., 2017)
	$La(OH)_3$ modified magnetite	52.7	0.1 g/L; 1 to 10 mg/L; pH of 7; 25 °C	EA; ELE; SP	(Fang et al., 2018)
	g-C_3N_4 modified Fe_2O_3	52.5	1 g/L; 5.7 mg/L; pH of 2–12; 24 °C	EA; ELE	(Gamshadzehi et al., 2019)
	H_2 calcined Al substituted goethite	5.96	0.5 g/L; 0.5 mg/L; pH of 5.5; 25 °C	EA; ELE; SP	(Li et al., 2019)
Modified laboratory synthesis ICNs	Ca and Mg co-modified Fe_2O_3	17	1 to 15 g/L; 200 mg/L; pH of 7; 25 °C	EA; ELE; SP	(Han et al., 2017)
	Biochar modified hematite	13.81	2 to 3 g/L; 8 mg/L; pH of 2; 25 °C	EA; ELE	(Zhang et al., 2020a)
	Bamboo biochar modified nano-α-Fe_2O_3/Fe_3O_4	8.73	10 g/L; 2 to 50 mg/L; pH of 3; 25 °C	EA; SC	(Zhu et al., 2018a)
	TiO_2 modified Fe_3O_4	64.6	1 g/L; 10 mg/L to 200 mg/L; pH of 6; 25 °C	EA; ELE	(Kong et al., 2022)
	Melamine sponge modified FeOOH	115.5	25 g/L;10 to 400 mg/L; pH of 2 to 12; 25 °C	EA; SC	(Tao et al., 2022)
	Bagasse modified ferrihydrite	180.7	0.4 g/L; 50 mg/L; pH of 5.3; 25 °C	EA; SC	(Zhou et al., 2020)
	Biochar modified nano-sized goethite	42.7	10 g/L; 100 mg/L; pH of 5.2 to 9; 25 °C	EA; PA	(Zhu et al., 2020)
	Biochar modified goethite	12.33	5 g/L; 15 mg/L; pH of 2; 25 °C	ELE; EA	(Qin et al., 2023)
	ZrO_2 modified Fe_3O_4	27.9–69.4	2.5 g/L; 1 to 300 mg/L; pH of 5; 25 °C	EA; ELE	(Wang et al., 2016)
	ZnO modified Fe_3O_4	100.3	0.3 g/L; 20 to 60 mg/L; pH of 7; 25 °C	ELE; EA; SC	(Li et al., 2018)

Note: surface precipitation—SP; electrostatic ligand exchange—ELE; electrostatic attraction—EA; physical adsorption—PA; surface complexation—SC.

through coprecipitation contained Fe—O groups and exhibited a larger phosphate adsorption capacity (42.7 mg/g) than biochar (Zhu et al., 2020). Zhang et al. (2021b) obtained a phosphate adsorption capacity of 57.39 mg/g in NaOH-modified–biochar composite goethite (a-FeOOH–600BC) formed using the impregnation method. The a-FeOOH–600BC has a higher PZC (8.2) than a-FeOOH (PZC = 5.2), and its phosphate adsorption capacity exceeds that of raw goethite (7.19 mg/g). However, the discovery of NZVI, maghemite, and wüstite in the ashes of wildfires at the interface between wilderness and urban areas is particularly interesting. The formation of these reduced iron phases may be attributed to the reduced atmosphere (H_2 or CO) or decreasing substances (carbon) generated in the combustion of forest biomass during the fire, which reduced goethite, hematite, and maghemite in the soil to NZVI, magnetite, and wüstite (Baalousha et al., 2022) (Fig. 6A–D). These reduced iron phases seriously impact the environment and human health because magnetite nanoparticles are linked to neurodegenerative diseases and climate change (Baalousha et al., 2022). However, future research directions will focus on the utilization of this method in the preparation of highly active ICNs.

4.2.3. Al-substituted ICNs

Al also binds to phosphate; therefore, Al-substituted mICNs have been synthesized via impregnation with iron and Al salts (Li et al., 2016b; Li et al., 2016c; Liao et al., 2020). Al (0.53 Å) has a smaller atomic radius than Fe (0.65 Å); thus, substituting Al atoms at Fe-atom sites in the ICN lattice decreases the unit cell (Li et al., 2016b). The SSA, surface functional groups, crystallinity, surface charge density, and PZC of Al-substituted mICNs differ from those of their ICN counterparts. Al-substituted goethite (Al-goethite) (Li et al., 2016c), hematite (Al-hematite) (Li et al., 2016b), and lepidocrocite (Al-lepidocrocite) have all been synthesized using the impregnation method (Liao et al., 2020).

4.2.3.1. Al-substituted goethite. Compared with raw goethite, Al-goethite has weaker crystallinity, a higher hydroxyl group content, a more granular shape, and a faster phosphate isotope exchange rate (Li et al., 2016c). Increasing the substituted amount of Al from 0 to 32 mol% in Al-substituted goethite reduces the cell parameter *c* from 3.029 Å to 2.99 Å, thereby decreasing the cell volume and increasing the crystal density from 137.35 Å to 139.28 Å. The average Fe—O distance (6 Å) remains unchanged, while the edge-shared Fe—Fe(Al) distance decreases from 6 Å to 4 Å. Al substitution increases the hydroxyl content of

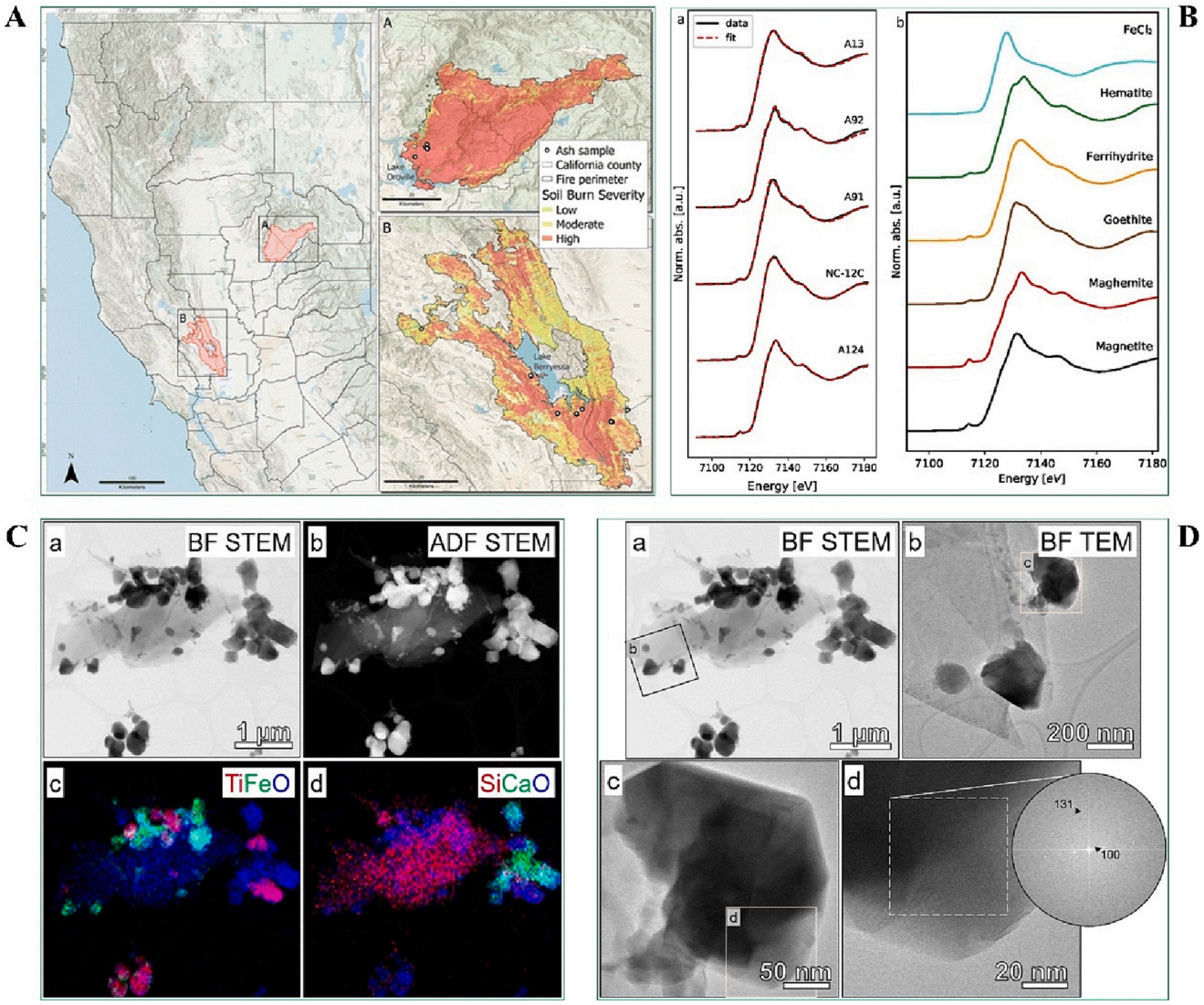

Fig. 6. (A) Map of specific locations at the interface between wilderness and urban areas (Baalousha et al., 2022); (B) XANES spectroscopy of Fe K-edge in flying ash in fire outbreaks (Baalousha et al., 2022); (C) TEM and EDS images of flying ash in fire outbreaks (Baalousha et al., 2022); (D) TEM images and electron diffraction patterns of flying ashes in fire outbreaks (Baalousha et al., 2022).

goethite while decreasing the O content in the lattice and adsorbed water molecules. Al-goethite adsorbs more phosphate (712 mmol/kg) than raw goethite (326.8 mmol/kg) (Li et al., 2016c). Torrent et al. (1992) determined the phosphate adsorption capacities on different facets of 31 types of synthetic Al-goethite with similar unit surface areas at pH of 6. They reported similar adsorption capacities on different facets. However, the characterization methods for assessing the interaction and morphology of phosphate-adsorbed Al-goethite differ among studies. Hsu et al. (2020), who compared the phosphate adsorption performances of goethite and Al-goethite, found that the Fe—O—P angle (131.38°) of phosphate adsorbed to Al-goethite was larger than the corresponding Al—O—P angle (124.48°). The study found that the Al substitution for goethite increased the phosphate fixation capacity from 135 mmol/kg to 584 mmol/kg due to the increase in the proportion of Al substitution in goethite from 0 to 17.4 mol%. Density functional theory (DFT) simulations and X-ray absorption near-edge structure spectroscopy (XANES) have recently shown that phosphate on Al-goethite preferentially bonds to Al (Fig. 8[A] and [B]). Xu et al. (2019) found that as the Al substituted amount in Al-goethite increased from 0 to 9 mol%, the SSA decreased from 64.9 to 57.7 m^2/g and the surface roughness of Al-goethite continuously increased, enhancing the surface charge density from 3.48 nm^2 to 3.54 nm^2. In addition, the aspect ratio of {110}/{021} facets decreased from 9 to 4.26 while the phosphate adsorption capacity of Al-goethite increased (Fig. 7A). Phosphate adsorbed on Al-goethite exhibits large and low affinity for bidentate and monodentate complexes, respectively. Li et al. (2019) varied the Al-substituted amount of Al-goethite for phosphate removal from 0 to 12 mol%. The Al-substituted goethite was H_2 calcined, thereby revealing the transformation of Al-magnetite by the pyrolysis phase into a mixture of Al-nZVI and Al-magnetite. The phosphate adsorption capacity increased from 1.21 mg/g to 5.96 mg/g when the substitution of Al in goethite increased from 0 mol% to 12 mol%.

4.2.3.2. Al-substituted lepidocrocite. Studies on phosphate removal by Al-substituted lepidocrocite are comparatively few. Al-lepidocrocite forms thinner crystals with a smaller aspect ratio than lepidocrocite crystals, thereby reducing the ratio of coherent scattering domain sizes of the (020) facet to the coherent diffractive domain sizes of the terminating (200) and (002) facets (Fig. 7C). The relative proportion of (020) facet with double-coordinated oxygen per SSA decreased, while the amount of active hydroxyl groups and phosphate adsorption density increased (Fig. 7D and E, respectively) (Liao et al., 2020). Liao et al. (2020) reported that as the Al-substituted amount in Al-lepidocrocite increased from 0 to 28.3 mol%, the Fe—O distance decreased from 2.011 Å to 2.003 Å, and the Fe—Al distance decreased from 3.074 Å to 3.063 Å, the SSA increased from 78 m^2/g to 383 m^2/g, and the adsorption capacity of phosphate increased from 185 μmol/g to 849 μmol/g.

4.2.3.3. Al-substituted hematite. Compared with hematite, Al-hematite exhibits a larger unit cell volume and lower unit cell density. The common-surface Fe—Al, common-edge Fe—Al, and average O—O distances are all larger in Al-hematite than in hematite. The adsorption ratio of phosphate is lower on the basal facets (001) of Al-hematite than that of hematite (Fig. 7B, F, and G) (Li et al., 2016b). In one study (Stanjek, 1992), raising the Al substitution amount from 0 to 9 mol% induced an increase in cell volume from 280 $Å^3$ to 307 $Å^3$, while the cell density decreased from 5.673 g/cm^3 to 5.170 g/cm^3. Li (2017) showed that altered the Al substitution amount in Al in hematite from 0 mol% to 20 mol%. They reported an SSA increase from 29.19 m^2/g to 61.13 m^2/g and an increase in phosphate adsorption capacity from 2.8199 mg/g to 10.8463 mg/g. Barron et al. (1988) synthesized 43 specimens with different molar fractions of Al-hematite and averaged their phosphate adsorption densities to obtain 0.97 μmol/m^2. The different phosphate affinities of goethite and hematite are attributed to the different facets of the two minerals. Notably, Al can be substituted into natural ICNs, which exhibit higher activity than Al-hematite (Xu et al., 2019). The phosphate adsorption capacity of Al-hematite is lower and comparable to that of limonite (Cheng et al., 2017). Overall, the following conclusions are obtained: (1) Al substitution for ICNs will lead to structural defects in ICNs, increasing the surface-active sites of Al-substituted ICNs. Al also inhibits the growth of ICN crystals, resulting in large SSA and small crystal sizes. (2) The toxic effects of Al on aquatic organisms and plants will be a future research direction that must be studied.

4.2.4. Lanthanum–cerium-modified ICNs

Lanthanum (La) and cerium (Ce) selectively and strongly bind to phosphates; moreover, La- and Ce-modified ICNs form oxygen-containing functional groups that can be synthesized through similar co-precipitation methods (Fang et al., 2018; Shan et al., 2021). For example, Fu et al. (2018) showed that ferrihydrite and La co-modified with magnetite (Mag@Fh–La) have a phosphate adsorption capacity exceeding 44.8 mg/g and an SSA of 85.8 m^2/g. Shan et al. (2021) determined the phosphate adsorption capacity and SSA of $C_3Ce_2O_9{\cdot}xH_2O$-modified magnetite (M-HCC) as 98.3 and 26.23 m^2/g, respectively (Fig. 5B). $La(OH)_3$- and $NaLa(CO_3)_2$-modified magnetite can also remove phosphate through solvothermal methods (Fig. 8C) (Ahmed and Lo, 2020; Song et al., 2020) or hydrothermal methods (Hao et al., 2019). Among these mICNs, $NaLa(CO_3)_2$-modified magnetite (MLC) (Hao et al., 2019) exhibits the largest phosphate adsorption capacity (77.85 mg/g) (Fig. 5D). Overall, although rare-earth-modified ICNs have substantially higher removal capabilities compared to other elements modified by ICNs, the application of rare-earth-modified ICNs is relatively limited. In addition, scientists are currently researching the effects of rare earth elements on the human body, microorganisms, aquatic animals, and the environment.

4.2.4.1. Other metal-modified ICNs. Investigations on Zn, Mn, and Zr as ICN modifiers are limited (Belloni et al., 2023). These modified elements are expensive and easily cause secondary pollution. For example, Zn-substituted goethite exhibits a higher PZC of 8.81 and phosphate adsorption capacity than goethite (8.81 and 6 mg/g, respectively, versus 8.42 and 5 mg/g, respectively, in goethite). Surface protonation enables a charge compensation mechanism in Zn-substituted goethite. However, Mn and Zr substituents reduce the PZC of goethite to 8.24 and 7.5, respectively, and the phosphate absorption capacities to 4 mg/g (Belloni et al., 2023).

4.2.5. Other modified ICNs

ICN modification by $KMnO_4$, H_2O_2 (Fig. 5E) (Xing et al., 2022), polyacrylonitrile, tetra-n-butylammonium bromide (Fig. 5C) (Wang et al., 2021b), FeS_2 (Cai et al., 2019), chitosan, and poly (acrylic acid) (Szewczuk-Karpisz et al., 2023) have not been extensively investigated because the raw materials are costly and contribute to secondary pollution. For example, Xing et al. (2022) reported a higher phosphate adsorption capacity in $KMnO_4$-modified siderite ($KMnO_4$-siderite) than that in H_2O_2-modified siderite (13.04 mg/g versus 3.28 mg/g) because $KMnO_4$-siderite forms crystalline 2LFh that reduces the nucleation barrier of 2LFh. H_2O_2 can effectively oxidize siderite Fe(II) to $Fe(OH)_3$, but the lattice Mn(II) of siderite cannot be oxidized. The exposed Mn(II) and $Fe(OH)_3$ produce a dense passivation film that terminates oxidation and decreases the phosphate removal efficiency. Polyacrylonitrile- and tetra-n-butylammonium bromide-modified hematite (Wang et al., 2021b), benzyldimethyldodecylammonium chloride-modified akageneite (Abu-Obaid et al., 2022), magnetite-modified pyrite (Cai et al., 2019), chitosan, and poly (acrylic acid)-modified goethite (Szewczuk-Karpisz et al., 2023) have been used for phosphate removal. Among these mICNs, magnetite-modified pyrite exhibits the largest phosphate

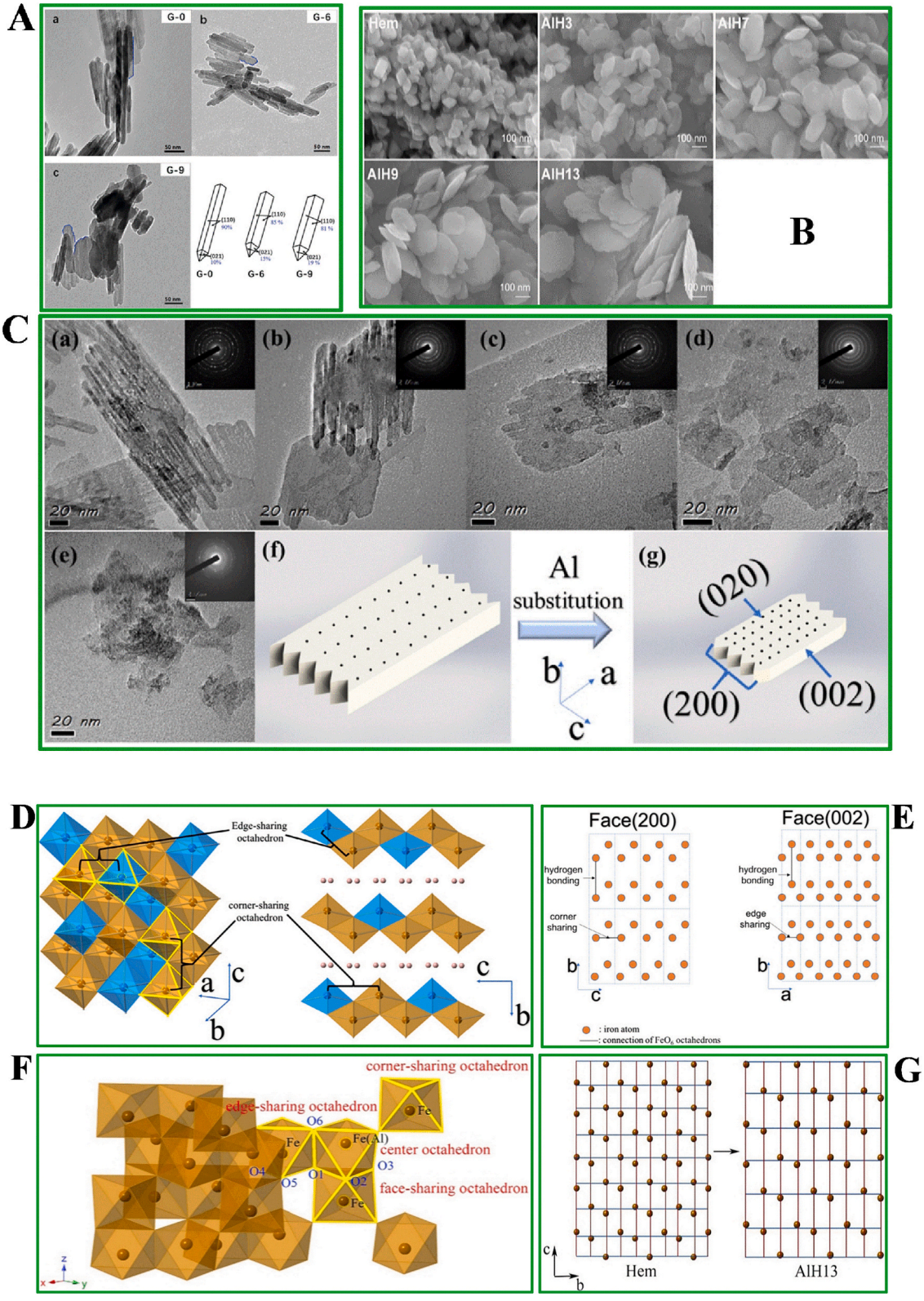

Fig. 7. (A) TEM images and facets of Al-goethite (Xu et al., 2019); (B) SEM images of Al-hematite and hematite (Li et al., 2016b); (C) TEM and selected area electron diffraction images of Al-lepidocrocite: lepidocrocite (a), Al-lepidocrocite 3 % (b), Al-lepidocrocite 5 % (c), Al-lepidocrocite 10 % (d), and Al-lepidocrocite 20 % (e); schematic of models of the facets of lepidocrocite (f) and Al-lepidocrocite (g) (Liao et al., 2020). (D) Schematic of (110) and (021) facets of Al-lepidocrocite (pink: H, blue: Al, yellow: Fe) (Liao et al., 2020); (E) schematic of network density maps of the (200) facet of Fe and the (002) facet of Al-lepidocrocite (Liao et al., 2020); (F) schematic of coordination of lattice iron atoms with Al-hematite (Li et al., 2016b); (G) schematic of Fe-network density maps of hematite (left) and Al-hematite (right) in the *b*–*c* direction (Li et al., 2016b).

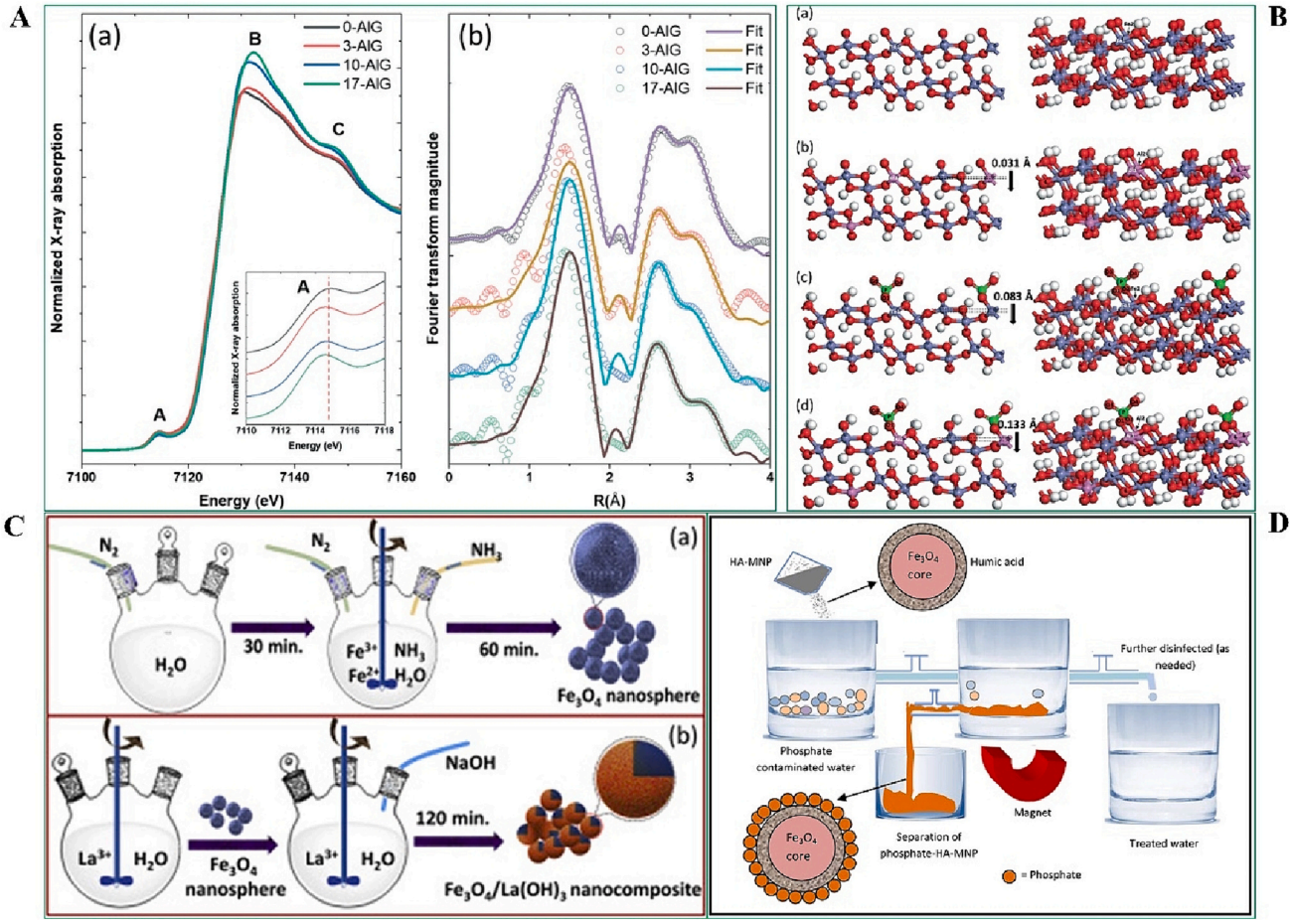

Fig. 8. (A) Fe K-edge XANES spectra of goethite and Al-goethite (Hsu et al., 2020); (B) Fourier-transformed Fe K-edge EXAFS of goethite and Al-goethite (Hsu et al., 2020); (C) schematic of modification process of $La(OH)_3$ modified Fe_3O_4 (Ahmed and Lo, 2020); (D) Schematic of enhanced phosphate management with the use of humic acid modified magnetite (Rashid et al., 2017).

adsorption capacity (24.8 mg/g) (Cai et al., 2019). Table 4 shows the adsorption capabilities of laboratory-synthesized ICNs and natural ICNs for phosphate.

5. Adsorption mechanisms of phosphate on ICNs and mICNs

Understanding the mechanism of phosphate adsorption is essential because it involves the recovery of ICNs and mICNs. This section reviews various mechanisms of phosphate adsorption: surface precipitation (Liu et al., 2013b), electrostatic ligand exchange (Fu et al., 2018), electrostatic attraction (Cai et al., 2019), and surface complexation (Ahmed et al., 2019).

5.1. Electrostatic attraction

Electrostatic attraction mainly involves positively charged groups on ICNs and mICNs or protonation at low pH. The pH modifies the surface morphology of ICNs and mICNs. For example, FeO^- (pH > 8.84), $FeOH_2^+$ (pH < 4.65), FeOH (pH = 4.65–8.84) (Wang et al., 2021a), and phosphate species such as $H_2PO_4^-$ ($pK_1 = 2.15$), HPO_4^{2-} ($pK_2 = 7.2$), and PO_4^{3-} ($pK_3 = 13.3$) can change the morphology of ICNs and mICNs (He et al., 2022).

The pH values of ICNs and mICNs are below the PZCs, which range between 5.4 and 8.6 (Jang et al., 2006). Therefore, ICNs and mICNs such as nano-Fe_3O_4 (Yoon et al., 2014) adsorb phosphate via electrostatic attraction on their positive surface charges (Wang et al., 2021a). Electrostatic adsorption can occur simultaneously with surface precipitation in some composites (such as magnetite-modified pyrite composites); thus, electrostatic adsorption is the driving force in ICNs and mICNs (Cai et al., 2019). On the contrary, negatively charged ICNs and mICNs will experience electrostatic repulsion with phosphate ions in an environment where the PZC is below the pH value of the solution. However, recent reports have found that phosphate removal is not inhibited when the pH value of the water environment is higher than the PZC of ICN or mICN, possibly due to the occurrence of mechanisms other than electrostatic interactions, such as electrostatic ligand exchange. One example is the phosphate removal mechanism of Mag@Fh–La by electrostatic ligand exchange (Fu et al., 2018). Overall, the main mechanism for removing phosphate from ICNs and mICNs involves electrostatic attraction, which is primarily influenced by the pH of the water environment and the active sites on ICNs and mICNs (Wang et al., 2021a). The negative surface charge of ICNs and mICNs also increases with pH, resulting in the inhibition of phosphate adsorption due to the generation of electrostatic repulsion by negatively charged phosphate ions in the solution (Wang et al., 2021a). Additionally, the number of protonizable ligands and active sites exposed to ICNs and mICNs increases at low pH ranges, resulting in strong electrostatic attraction between ICNs, mICNs, and phosphate ions, ultimately promoting high adsorption. Importantly, electrostatic interaction occurs during physical and chemical adsorption processes. Compared with other adsorption mechanisms, electrostatic interactions are reversible and more easily achieved.

5.2. Electrostatic ligand exchange

The surface physical and chemical properties of ICNs and mICNs depend on their ligand exchange capability, particularly surface charge. If ICNs or mICNs carry negative surface charge in aqueous environments, then electrostatic repulsion will occur, which is not conducive to capturing phosphate ions (Wang et al., 2021a). In addition, ICNs and mICNs adsorb even low concentrations of phosphate through intramolecular complexation driven by electrostatic ligand exchange. When phosphate adsorbs on the surfaces of ICNs and mICNs, it covalently bonds with iron ions and OH^-; alternatively, ligands bound to the iron ions are released, forming inner-sphere complexes. The OH^- groups undergo electrostatic ligand exchange with the negatively charged OH^- groups of ICNs and mICNs, causing a PZC reduction of the particles after phosphate adsorption (Wang et al., 2021a). For example, the phosphate remover M-HCC forms an inner-sphere complex via electrostatic ligand exchange (Shan et al., 2021). In the phosphate removal mechanism of iron oxide waste, electrostatic attraction is driven by electrostatic ligand exchange and ion exchange, whereas electrostatic repulsion is driven by Lewis acid–base interactions (Zeng et al., 2004). Multimetal-modified ICNs are adopted to compensate for the shortcomings of single-metal-modified ICNs and enhance the affinity of ICNs for phosphate. The synergistic effect of multimetals will influence the pore size, adsorption capacity, pore volume, and crystal structure of modified ICNs.

5.3. Surface complexation

Despite numerous publications on the adsorption of phosphates by ICN and mICN systems, the surface complexation structure of ICNs and mICNs with phosphates has remained controversial. Complexes form when ICNs and mICNs bind or retain O-containing functional groups on their surfaces. ICNs and mICNs provide complexes formed between functional groups (such as Fe and OH^- ions) with binding sites that ultimately increase the specific adsorption of Fe. The surface complexation formation of phosphate and iron ions can be divided into four types (Arroyave et al., 2018; Elzinga and Sparks, 2007; Weng et al., 2020; Zach-Maor et al., 2011): mononuclear bidentate complexes (MBCs), bidentate mononuclear complexes (BMCs), mononuclear monodentate complexes (MMCs), and binuclear bidentate complexes (BBCs) (Nanzyo and Watanabe, 1982; Persson et al., 1996; Tejedor-Tejedor and Anderson, 1990). Surface complexations of ICNs and mICNs with phosphate are reviewed below.

5.3.1. Goethite

The pH affects the type and coordination of phosphate ions adsorbed by goethite. The phosphate coordination form on goethite is transformed by the dissociation and association of surface phosphate ions induced by a pH change. Binuclear ligand phosphate is more stable than mononuclear ligand phosphate due to the differences in bond energies and structures between the two surface complexes (Liu, 1997; Parfitt and Atkinson, 1976). K-edge-extended X-ray absorption fine structure spectroscopy has characterized the chemical bond distances between phosphate and surface complexes formed by goethite. At pH 4.5, BBCs between phosphate and goethite exhibit P—O and P—Fe spacings of 1.51–1.53 and 3.2–3.3 Å, respectively; MMCs present a P—Fe spacing of 3.6 Å, and BMCs present a P—Fe spacing of 2.83–2.87 Å (Abdala et al., 2015; Abdala et al., 2015a). Performing infrared surface titrations, Arroyave et al. (2018) demonstrated that phosphate adsorbed on goethite forms MBC and MMC at pH < 5.5 and pH > 5.5, respectively. A diffuse-reflectance Fourier transform infrared (FTIR) study suggested phosphate adsorbed by goethite forms a BBC at pH 3.3–11.9 (Nanzyo and Watanabe, 1982). Persson et al. also reported similar results (Persson et al., 1996). Phosphate adsorbed on α-FeOOD or α-FeOOH also forms a BBC (Atkinson et al., 1974). Attenuated total reflection FTIR (ATR-FTIR) characterization by Luengo et al. (2006) illustrated that on phosphate-adsorbed goethite, non-protonated and protonated bidentate complexes coexist at pH 4.5, but only non-protonated bidentate complexes form at pH 7.5–9. These different surface complexation forms of goethite and phosphate under different pH conditions might reflect various microenvironments, including different phosphate adsorption densities, goethite synthesis conditions, and characterization methods (Parfitt et al., 1976).

The configuration of goethite-adsorbed phosphate (monodentate or bidentate) depends on the properties (exposed facets) of goethite (Kubicki et al., 2012). For example, Ahmed et al. (2019) demonstrated bidentate and monodentate complexes on the (100) and (010) facets of goethite, respectively (Fig. 9A). Goethite can form MBCs along with the monodentate motif as a minor fraction. Goethite forms hydrogen bonds with phosphate, and H_2O and its surface atoms form covalent bonds with the Fe atoms of H_2O. Other atoms dissociate into hydroxyl groups and protons at the surface (Fig. 9B). Weng et al. (2020) demonstrated that phosphate adsorption via monodentate chemisorption on the (100) facet of goethite reached 83 %, whereas that via bidentate chemisorption adsorption was low (0.04 %). The physisorption of adsorbed phosphate follows a Maxwell–Boltzmann distribution with a mean of 17 % (Fig. 9C). Atomic force microscope (AFM) characterization has shown phosphate complexes with goethite via an in-situ kinetic process of soluble phosphate immobilization on goethite. Iron–phosphate complexes can dissolve to release soluble phosphate that migrates through and transforms soil (Wang et al., 2012a). Recent research shows that the unit cell on the (010) surface of goethite is periodic and adsorbs phosphate at a concentration of 0.01 mol/L at a pH of 2.6. AFM characterization confirmed the presence of monodentate ligand hydroxyl groups on the (010) facet of goethite adsorbed with phosphate and hydrogen ions (Dideriksen and Stipp, 2003).

The complexation of phosphate on goethite facets also depends on the phosphate adsorption density. At low ($\leq$1.5 μmol/m^2) and high (>1.5 μmol/m^2) adsorption densities, phosphate forms non-protonated bidentate complexes and MMCs with goethite, respectively (Rahnemaie et al., 2007). Importantly, Tejedor-Tejedor and Anderson (1990) found that BBCs dominate at low pH (3.5–6.5) and high surface phosphate adsorption density (190 μmol/g), whereas MMCs dominate at high pH (6.5–8) and low surface phosphate adsorption density (100 μmol/g). Notably, goethite and hematite nucleate with phosphate to form amorphous-phase iron phosphate nanoparticles (1–4 nm). Crystalline-phase iron phosphate nanoparticles (>4 nm) then develop through aggregation and growth processes (Wang et al., 2015a; Wang et al., 2018).

5.3.2. Ferrihydrite

Ferrihydrite exhibits a higher OH^- release, larger SSA, and lower crystallinity than goethite and hematite (Wang et al., 2013). Phosphate adsorbs to ferrihydrite through a surface complexation process. First, rather than releasing OH^-, ferrihydrite forms a BBC coordination structure with phosphate. This stage is achieved through the exchange of phosphate with two Fe-$OH_2^{1/2+}$ groups. Compared to larger crystals, smaller ferrihydrite crystals with more Fe-$OH_2^{1/2+}$ groups exhibit a higher mass transfer rate per unit mass. Subsequently, Fe-$OH^{1/2-}$ and Fe-$OH_2^{1/2+}$ exchange with phosphate, releasing OH^- at each moment of phosphate adsorption. Various characterization methods confirmed that the adsorbed phosphate forms a BBC with a P—Fe distance of 3.25 Å on the surface of ferrihydrite after the release of OH^- (Wang et al., 2013). Arai and Sparks (2001) reported that phosphate-adsorbed ferrihydrite forms a non-protonated inner-sphere BBC ($\equiv Fe_2PO_4$) at pH $\geq$ 7.5. ATR-FTIR spectra revealed the formation of protonated inner-sphere complexes through adsorption–coordination processes at pH 4–6. Khare et al. determined a BBC of phosphate-adsorbed ferrihydrite at a pH of 6 based on XANES spectra (Khare et al., 2007).

The charge distribution–multisite surface complexation (CD-MUSIC) model can assess the surface charge characteristics of ferrihydrite at different phosphate concentrations, pH, zeta potentials, PZC, and OH/P exchange rates. The model also describes the morphology of phosphate-

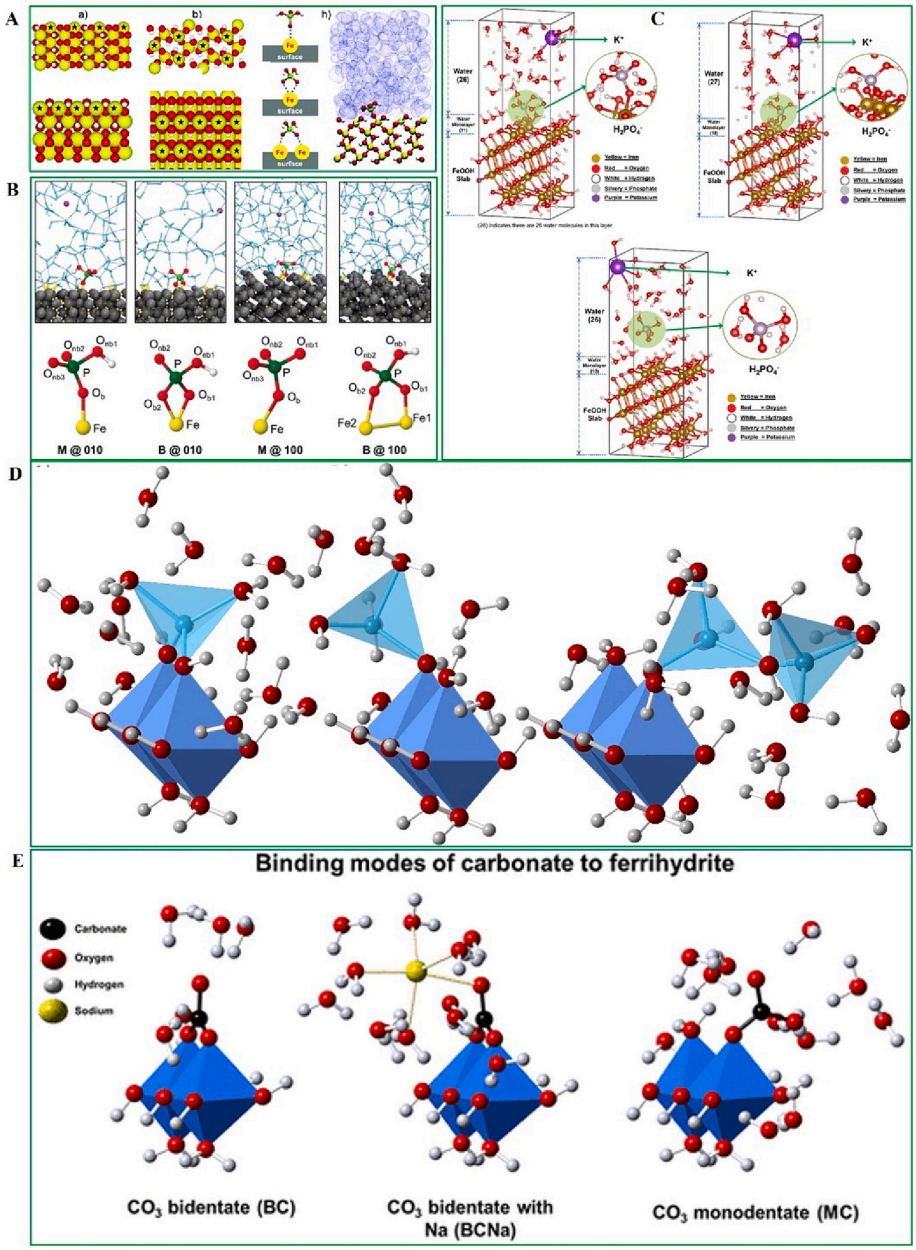

Fig. 9. (A) and (B) Schematic of phosphate adsorption on goethite and water interface with model specification (for details, see Ahmed et al., 2019); (C) schematic of possible adsorption configurations and (100) facet of hydrous ferric oxides (Weng et al., 2020); (D) schematic of Zn and ferrihydrite with surface complexity modeling (for details, see Eynde et al., 2022); (E) schematic of carbonate and ferrihydrite binding modes (Mendez and Hiemstra, 2018).

adsorbed ferrihydrite (Antelo et al., 2005; Hiemstra and van Riemsdijk, 1996). Antelo et al. (2010) employed the CD-MUSIC model and demonstrated the adsorption of protonated and non-protonated bidentate complexes of ferrihydrite with phosphates. The CD-MUSIC model also confirmed that surface groups of the monodentate ligand dominate the ferrihydrite surface. Angle-sharing among these configurations enables double-corner sharing, thereby forming bidentate surface complexes that affect the complexation with phosphates (Hiemstra and van Riemsdijk, 2009).

5.3.3. Other ICNs or mICNs

Phosphate-adsorbed hematite also forms surface complexes. An in-situ ATR–FTIR study by Elzinga and Sparks (2007) showed that phosphate-adsorbed hematite forms MBCs and is protonated or non-protonated at pH 8.5–9.0. O_2-calcined siderite forms MBCs and MMCs with phosphate (Xing et al., 2017). In addition, based on characterizations by 31P nuclear magnetic resonance spectroscopy, lepidocrocite, akageneite, and goethite form inner-sphere complexes and O–Fe(III)–P covalent bonds with phosphate (Ler and Stanforth, 2003). At low pH ($\leq$6.5), O_2-calcined siderite, hematite, akageneite, goethite, and ferrihydrite interact with phosphate complexes to generate iron–phosphate precipitates (Chitrakar et al., 2006; Liu et al., 1995; Nilsson et al., 1992; Xing et al., 2017; Yan et al., 2014; Wang et al., 2015a).

The management of phosphate by ICNs and mICNs is generally mainly achieved through complexation, with electrostatic ligand exchange playing a dominant role in the complexation process (Wang et al., 2021a). The nature of the metal active sites, the pH of the water environment, and the ligands on ICNs and mICNs all display an impact (Wang et al., 2021a). As the pH of the water environment increases, ligands involved in phosphate exchange (such as hydroxyl groups) will typically dissociate, forming complexes with phosphate at the metal

active sites. When the ligand is active, additional exposed metal active sites emerge, facilitating the easy formation of complexes with phosphate.

5.4. Precipitation

Precipitation on ICNs and mICNs is an effective phosphate removal mechanism. Precipitation occurs when the concentration of the product in each component of an aqueous solution far exceeds the solubility of that product (He et al., 2022). Moreover, precipitation is irreversible and rapid. Phosphate adsorbs to the Fe in ICNs and mICNs with a solubility product constant of K_{sp} [$FePO_4$] = 1.3 × 10^{-22}. ICNs modified with other metals form other precipitates containing Ca (Almanassra et al., 2021), Al (Li et al., 2016b; Li et al., 2016c; Liao et al., 2020), La (Fang et al., 2018), and Ce (Shan et al., 2021) with K_{sp}[$LaPO_4$] = 3.7 × 10^{-23}, K_{sp}[$Ca_3(PO_4)_2$] = 2.07 × 10^{-33}, K_{sp} [$CePO_4$] = 1 × 10^{-23}, and K_{sp} [$AlPO_4$] = 5.8 × 10^{-19}, respectively. For example, complexation between phosphate and ferrihydrite leads to $FePO_4$ precipitation (Mallet et al., 2013). Chen et al. (2021b) found that phosphate-adsorbed siderite forms amorphous iron–phosphate complexes and $FePO_4$. However, amorphous structures have a high affinity for phosphate. Phosphate adsorbed at high surface density (30–500 μmol/g) on goethite precipitates as iron phosphate (Li and Stanforth, 2000; Ler and Stanforth, 2003). $Fe_3Mn_2(PO_4)_{2.5}(OH)_2$ precipitation can also follow phosphate adsorption on natural goethite (Martin et al., 1988). The adsorption process of phosphate by goethite and natural goethite also resulted in precipitation, but the precipitation form was different, which is attributed to the presence of other metal impurities in natural goethite (Li and Stanforth, 2000). More interestingly, phosphate and phytate can co-adsorb on ferrihydrite, forming BBCs with undetermined ternary complexes along with precipitates of amorphous Fe–phytate and $FePO_4$ (Wang et al., 2017).

ICNs are frequently associated with other minerals, such as aluminum and calcite. Studies have shown that phosphate precipitation on mineral-associated ICNs is selective and related to the chemical properties of the minerals, which influence the phosphate adsorption capacity, surface hydroxyl density, PZC, and SSA (Wei et al., 2014). For example, ferrihydrite associated with boehmite absorbs 0.1 mol/kg of phosphate, which preferentially adsorbs on ferrihydrite and precipitates as $FePO_4$. A phosphate adsorption amount of 1.3 mol/kg was reported on ferrihydrite associated with boehmite, in which the phosphate preferentially adsorbed on boehmite and then precipitated as aluminum phosphate ($AlPO_4$). Phosphate adsorbed at different amounts (0.2–0.6 mol/kg) is not preferentially adsorbed on mineral surfaces (Khare et al., 2004). XANES analysis shows that in mixed systems of goethite–boehmite and hematite–amorphous aluminum hydroxide cultured under the same conditions, phosphate preferentially binds to aluminum when the adsorption reaches saturation (Khare et al., 2004). This analysis also reveals that in a mixed ferrihydrite–calcite system, phosphate preferentially adsorbs to ferrihydrite due to the higher surface density of hydroxyls on ferrihydrite than on calcite (Adam, 2017). In addition to precipitation, phosphate adsorption is also affected by surface complexation and electrostatic adsorption. For example, phosphate adsorbs to N_2-calcined pyrite (Chen et al., 2015), siderite (Zhang et al., 2017a), natural pyrrhotite (Li et al., 2013), a-FeOOH–600BC (Zhang et al., 2021b), H_2-calcined ICNs (Li et al., 2019), and La-modified magnetite (Song et al., 2020). Analyses of the abovementioned ICNs and mICNs revealed a synergistic effect of multiple adsorption mechanisms. Overall, surface chemical precipitation can effectively control eutrophication and is the main method of phosphate management. In addition, the phosphate minerals obtained from surface chemical precipitation can be used as fertilizers, such as iron phosphate, hydroxyapatite, struvite, and vivianite (Wang et al., 2023). However, iron phosphate is easily formed in the water environment and is regarded as the main method for future phosphate recovery.

6. Factors affecting phosphate management using ICNs and mICNs

The effectiveness of phosphate adsorption in wastewater depends on the properties of ICNs and mICNs. This section discusses the influences of ionic strength, natural organic matter (NOM), cations, and anions on phosphate adsorption.

6.1. Ionic strength

Ionic strength influences phosphate adsorption by altering the surface potential and isoelectric point of ICNs and mICNs (Yan et al., 2021). Current reports reveal that the surface potential between the interface and ICN and mICN in the water environment is influenced by electrolyte concentration when the pH value is higher than 6. This phenomenon can be attributed to the weakened electrostatic repulsion between the charged surfaces of ICN, mICN, and phosphate by electrolytes, thus promoting phosphate adsorption (Barrow et al., 1980; Xu et al., 2014). The influence of ionic strength is minimal when the pH value is <6, and the surface coordination of ICN and mICN forms inner-sphere complexes through electrostatic adsorption and ligand exchange (Antelo et al., 2010). For example, the adsorption of phosphorus by Mag@Fh-La is controlled by the formation of inner-sphere complexes and is therefore unaffected by ionic strength (Fu et al., 2018). By contrast, in a study reporting the formation of outer-sphere complexes (Chen et al., 2022a), the phosphate adsorption capacity increased from approximately 2 mg/g to 7 mg/g when the ionic strength of LM and LAT aqueous solutions decreased from approximately 0.10 M to 0.01 M.

The isoelectric points of ICNs and mICNs largely influence the phosphate adsorption processes of these absorbers. When the pH is below the isoelectric point, ICNs and mICNs are positively charged, and the active adsorption sites exhibit a positive electrostatic potential. Increasing the ionic strength raises the anion concentration in the diffusion layer on the active sites while reducing the electrostatic potential. Consequently, the electrostatic attraction to phosphate decreases, along with the phosphate adsorption density (Barrow et al., 1980; Xu et al., 2014). When the pH exceeds the isoelectric point, ICNs and mICNs are negatively charged, and the diffusion layer comprises cations, generating a negative electrostatic potential at the active adsorption sites. The cation concentration also increases in the diffusion layer and at the active sites as the ionic strength increases. The absolute value of the surface potential on the adsorption surface decreases with the static potential and the repulsive force toward anions, while the number of active adsorption sites increases (Barrow et al., 1980; Xu et al., 2014). For example, studies have found that the adsorption density of phosphate on hematite increases within the pH range of 3–10 when the ionic strength in water environments rises (Yan et al., 2014). Additionally, the adsorption density of phosphate on goethite is higher within the pH range of 3–9 as the ionic strength in water environments increases (Antelo et al., 2005). Overall, ICNs and mICNs exhibit decreased adsorption efficiency for phosphates as the ionic strength increases, and the adsorbed phosphate forms outer-sphere complexes through electrostatic interactions. Conversely, ICNs and mICNs bind phosphate ions through direct interaction with metal active sites via H_2O molecules in the inner-sphere complexes, indicating that inner-sphere complexation is the main mechanism for phosphate adsorption. Additionally, with an increase in ionic strength in the reaction system, a large adsorption capacity or no change in adsorption capacity is observed.

6.2. Anions

Anions such as Cl^-, NO_3^-, HCO_3^-, F^-, SO_4^{2-}, CO_3^{2-}, $S_2O_3^{2-}$, AsO_4^{3-}, and SiO_4^{4-} affect phosphate adsorption by forming outer- or inner-sphere complexes between PO_4^{3-} and the ICNs or mICNs surface. Inner-sphere complexes are generally directly coordinated and unaffected by

coexisting anions, whereas outer-sphere complexes typically form via electrostatic interactions, which are highly sensitive to electrolytes (Wang et al., 2021a).

CO_3^{2-} mainly co-adsorbs with phosphate through bidentate inner-sphere complexation, strengthening the phosphate adsorption process at high pH > 7 with electrostatic interactions (Mendez and Hiemstra, 2018) (Fig. 9E). Meanwhile, PO_4^{3-} adsorption affects the metallogenesis of ICNs (Li et al., 2022b). Li et al. showed that at pH 7.5, CO_3^{2-} suppresses the formation of goethite and accelerates the evolution process of ferrihydrite to hematite, whereas PO_4^{3-} inhibits the dissolution of ferrihydrite (Li et al., 2022b). CO_3^{2-} also inhibits PO_4^{3-} removal and $LaPO_4$ formation on La-modified ICNs due to the lower K_{sp} (3.98×10^{-34}) of $La_2(CO_3)_3$ than ($K_{sp}[LaPO_4] = 3.7 \times 10^{-23}$) and hydrolyzes CO_3^{2-}, thereby increasing the pH and introducing competition between OH^- and PO_4^{3-} (Fu et al., 2018). A similar phenomenon was observed in HA–MNP (Rashid et al., 2017). (Fig. 8D).

SiO_4^{4-} also inhibits PO_4^{3-} adsorption to ICNs and mICNs. Chen et al. (2022) recently reported that goethite selectively adsorbs PO_4^{3-} and SiO_4^{4-} at pH < 4 and pH > 10, respectively. In the pH range 4–10, PO_4^{3-} and SiO_4^{4-} compete for the surface-active sites, thereby controlling their mutual retentions. More interestingly, Sabur et al. (2021) reported that SiO_4^{4-} does not inhibit PO_4^{3-} adsorption during co-adsorption of PO_4^{3-} and SiO_4^{4-} on goethite at pH 3–7, but competitive adsorption strengthens when the Si:P molar ratio increases (>4) under alkaline conditions (pH 7–11).

AsO_4^{3-} is another inhibitor of PO_4^{3-} adsorption. Liang et al. (2021) demonstrated the different preferences of AsO_4^{3-} and PO_4^{3-} for magnetite. Adsorbed PO_4^{3-} forms monoprotonated MMCs at acidic pH and non-protonated BBCs at alkaline pH. Meanwhile, AsO_4^{3-} forms BBCs with outer-sphere complexes. The adsorption affinities of PO_4^{3-} and AsO_4^{3-} on the magnetite surface decrease in the following order: BB arsenate complex > NBB phosphate complex > MMM phosphate complex (Fig. 12A). Gustafsson and Antelo (2022) demonstrated that PO_4^{3-} and AsO_4^{3-} can co-adsorb on ferrihydrite, forming angle-sharing bidentate and monodentate complexes. However, ferrihydrite has a higher affinity for AsO_4^{3-} than for PO_4^{3-}. Chen et al. (2022b) showed that AsO_4^{3-} can inhibit phosphate removal mainly through electrostatic repulsion and competition for the adsorption sites when PO_4^{3-} and AsO_4^{3-} co-exist. These mechanisms reduce the amount of PO_4^{3-} on goethite. Li et al. (2021) reported the same phenomenon.

When PO_4^{3-} and AsO_4^{3-} ions are simultaneously added to the system, the competition is small; but when these ions are added separately, the previously added component forms a surface complex with goethite, followed by precipitation (Zhao and Stanforth, 2001). Liu et al. observed a similar behavior (Liu et al., 2001). Han et al. (2020) reported the strong adherence of As^{3+} to the pyrite surface, followed by PO_4^{3-} and As^{5+}. They also observed a more violent reaction between pyrite and As^{5+} than between As^{3+} and phosphate (Fig. 12C). Meanwhile, coexisting Ca^{2+} and PO_4^{3-} compete for the active sites on goethite, affecting the adsorption of As^{3+} and As^{5+} and forming As(III)–goethite–As(V)–P–Ca. This process is mostly affected by pH (refer to Deng et al., 2018 for additional information).

Even more interestingly, the coexistence of Cl^-, NO_3^-, SO_4^{2-}, and $S_2O_3^{2-}$ promotes the removal of phosphate on H_2-calcined limonite due to the formation of several reactive sites through the accelerated iron corrosion and consequent establishment of a secondary phase (green rust) (Zhao et al., 2021a; Zhang et al., 2017). However, coexisting HCO_3^- and F^- inhibit phosphate adsorption on M–HCC due to the low solubility of $Ce_2(CO_3)_3$ ($pK_{sp} = 35.24$) and CeF_3 ($pK_{sp} = 15.1$) (Shan et al., 2021).

6.2.1.1. Other ICNs and mICNs. This review also examined the effects of coexisting anions on phosphate adsorption to O_2-calcined limonite (Cheng et al., 2017), O_2-calcined siderite (Xing et al., 2017), N_2-calcined pyrite (Chen et al., 2015), N_2-calcined mixed pyrite–goethite (Chen et al., 2016), $KMnO_4$-modified siderite (Xing et al., 2022), LM and LAT (Chen et al., 2022a), and pyrite (Wang et al., 2012). Anions exert an inhibitory effect on these ICNs and mICNs.

6.3. Cations

Cations and phosphates frequently coexist in the environment. Cations (e.g., Zn^{2+}, Mg^{2+}, Cd^{2+}, Ca^{2+}, Fe^{2+}, and Cu^{2+}) can either inhibit or promote the adsorption of ICNs and mICNs (Elzinga and Kretzschmar, 2013; Eynde et al., 2022; Liu et al., 2016; Hinkle et al., 2015; Rietra et al., 2001; Tao et al., 2023b; Senn et al., 2017). Competition for coordination sites on the ICN and mICN surfaces and the stable formation of non-adsorptive cation–oxygen–anion complexes inhibit adsorption, while the formation of ternary complexes and surface precipitates promotes adsorption (Benjamin and Leckie, 1982; Collins et al., 1999; Diaz-Barrientos et al., 1990; Jiang et al., 2013; Theis and West, 1986; Vaca-Escobar et al., 2012). For example, Liu et al. (2016) showed that PO_4^{3-} and Zn^{2+} can co-adsorb on ferrihydrite, forming a hydroxide-bridged ternary complex with ferrihydrite that promotes PO_4^{3-} adsorption. The latest research revealed that the coordination number of Zn varies from 4 to 6. Zn forms a double angle bidentate complex with ferrihydrite at Zn/Fe molar ratios below 0.1. Meanwhile, at molar ratios above 0.1, the Zn ions are partially neutralized through dimer formation, and Zn forms a hydroxide-bridged ternary complex on the ferrihydrite surface (Fig. 9D) (Eynde et al., 2022). Similar phenomena were observed during the co-absorption of PO_4^{3-} and Cu^{2+} on ferrihydrite (Eynde et al., 2022).

Co-adsorption of Cd^{2+} and PO_4^{3-} on hematite (Elzinga and Kretzschmar, 2013), goethite (Tao et al., 2023a), and ferrihydrite (Tiberg and Gustafsson, 2016) controlled the Cd^{2+} reactivity through electrostatic adsorption and ternary complex formation. In addition, Liu et al. (2021) reported that electrostatic adsorption drives the coprecipitation of Cd^{2+} and PO_4^{3-} on the surfaces of hematite, goethite, and ferrihydrite, which leads to the formation of tridentate complexation of bridging phosphates between phosphate ions. However, the mechanisms of these species contribute differently to adsorption on hematite, goethite, and ferrihydrite. The precipitation of coexisting Cd^{2+} and PO_4^{3-} is more substantial on ferrihydrite than on hematite and goethite, and electrostatic adsorption is the main adsorption mechanism for the coexistence of Cd^{2+} and PO_4^{3-} on goethite (Liu et al., 2021). The chemical properties of specific bonds and the different geometric configurations of PO_4^{3-} and metal ions on ICN surfaces contribute to the different adsorption mechanisms and stabilities of phosphate complexes on different ICNs (Li et al., 2021).

Ca^{2+} enhances PO_4^{3-} adsorption on goethite due to the electrostatic interaction of PO_4^{3-} and Ca^{2+} with goethite (Rietra et al., 2001). Ma et al. (2023) demonstrated the co-existence of Ca^{2+} and PO_4^{3-} on ferrihydrite, forming bidentate and monodentate phosphate surface complexes. Ca^{2+} forms a ternary complex with bidentate phosphate ($(FeO)_2PO_2Ca$). The Ca^{2+} retardation effect on migration promotes phosphate adsorption on ferrihydrite (Fig. 10A and B). Meanwhile, they found a gradual improvement in the hetero-aggregation between goethite and ferrihydrite nanoparticles in aquatic environments or soils during the transformation process from ferrihydrite nanoparticles to goethite nanoparticles, effectively immobilizing pollutants in the water environment (Fig. 11A) (Ma et al., 2020). Kim et al. (2022) found that PO_4^{3-} ions delay the dissolution and recrystallization of ferrihydrite nanoparticles, leading to the transformation to hematite. Hematite nanoparticles transform into ferrihydrite nanoparticles through dehydration and solid-phase transformation (Fig. 11B). The findings of these studies have certain reference values for the transformation of weakly crystalline ferrihydrite nanoparticles into thermodynamically stable hematite or goethite and the fixation of pollutants (Liu et al., 2007).

Co-adsorption of AsO_4^{3-} and PO_4^{3-} on ferrihydrite also synergistically adsorbs Ca^{2+}. Calcium phosphate ternary complexes (P-ferrihydrite-Ca) are formed at lower Ca^{2+} concentrations (0.5 mM), whereas

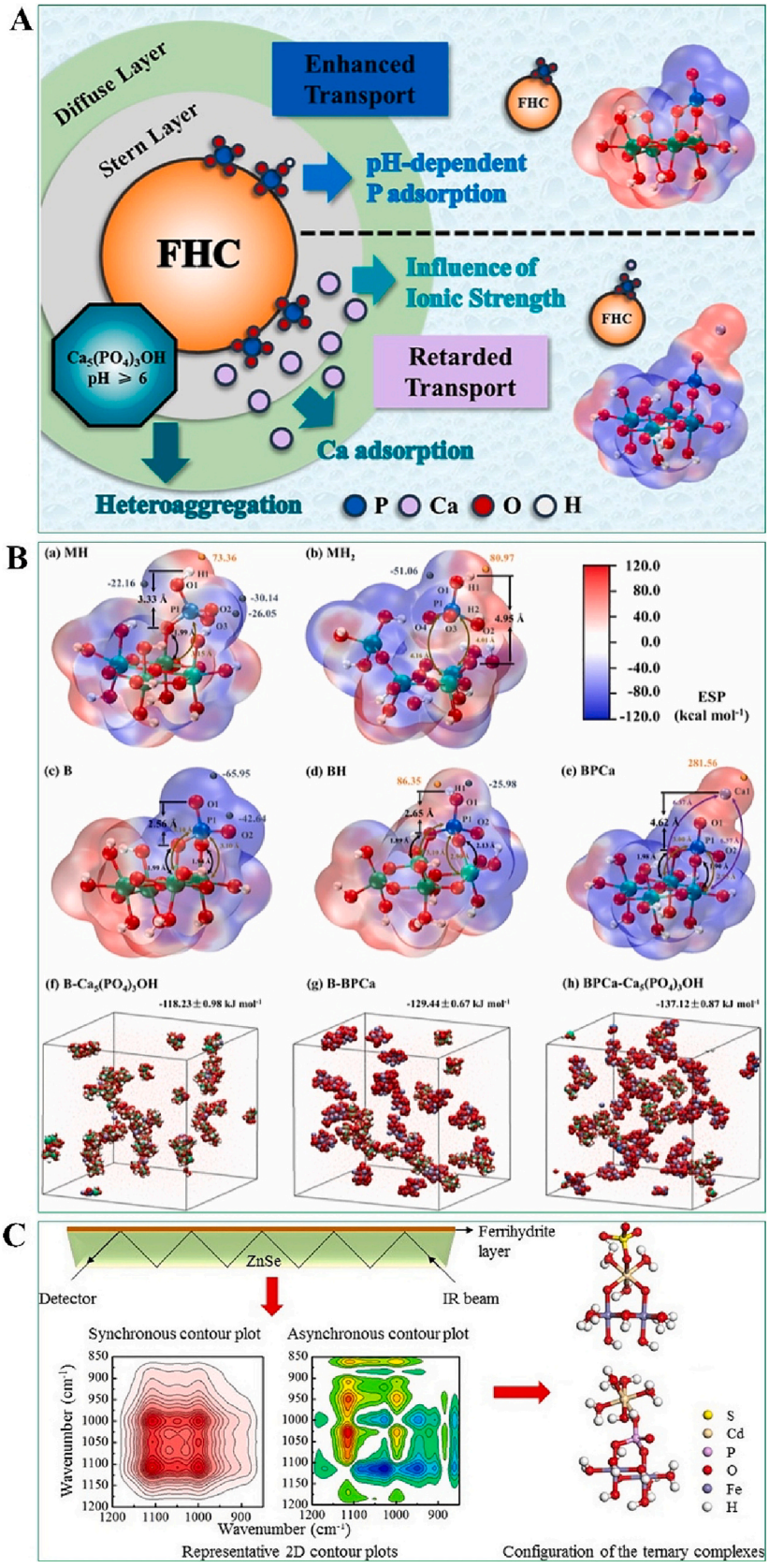

Fig. 10. (A and B) Schematic and DFT calculation diagram of phosphate enhancement and calcium inhibition of ferrihydrite colloid migration (Ma et al., 2023); (C) schematic of the synergistic adsorption of Cd(II) with phosphate/sulfate on ferrihydrite (Liu et al., 2018).

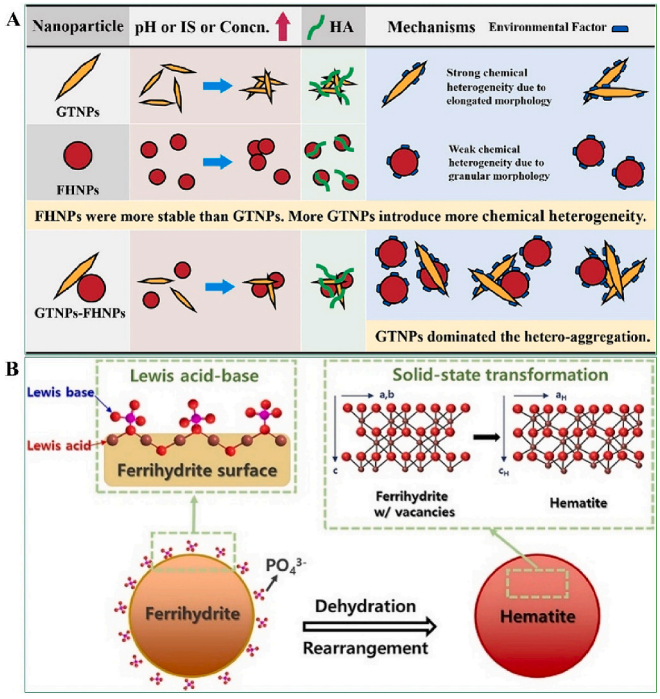

Fig. 11. (A) Schematic of heteroaggregation control of ferrihydrite and goethite by goethite nanoparticles (Ma et al., 2020); (B) schematic of phosphate as a stabilizer in the formation process of ferrihydrite/hematite (Kim et al., 2022).

hydroxyapatite ($Ca_5(PO_4)_3(OH)$) is formed at higher Ca^{2+} concentrations (6 mM) (Antelo et al., 2015). Another study reported the synergistic enhancement of Cd^{2+} adsorption on ferrihydrite through co-adsorbed PO_4^{3-} and SO_4^{2-} (Liu et al., 2018). Meanwhile, co-absorption of Cd^{2+} and PO_4^{3-} through electrostatic interactions forms P-bridged ternary complexes (P-ferrihydrite-Cd) that promote phosphate adsorption (Liu et al., 2018) (Fig. 10C). PO_4^{3-}, Mg^{2+}, and Ca^{2+} form a ternary complex that combines with ferrihydrite, obtaining an anionic bridged ternary complex ($FeOPO_3Mg$ and $(FeO)_2PO_2Ca$) and an $FeOPO_3Mg$ ternary complex in the Mg-PO_4 system (Fig. 12B) (Mendez and Hiemstra, 2020). Notably, Ca^{2+} and Mg^{2+} do not inhibit phosphate adsorption on MLC (Hao et al., 2019). Overall, cations can effectively promote the adsorption of phosphates by ICNs and mICNs. Compared to anions, cations in the solution are adsorbed, and the adsorption mechanism lies in the formation of negatively charged inner-sphere complexes. More importantly, the cations in the aqueous solution are a crucial active site for the precipitation of phosphates. The co-existence of cations can induce the precipitation of phosphates on the surface of ICNs and mICNs, effectively promoting the management of phosphates by ICNs and mICNs.

6.4. NOM

The functional groups and molecular weight contents of NOM influence phosphate adsorption on ICNs and mICNs. For example, Weng et al. (2008) showed that phosphate binding to goethite is inhibited by fulvic acid (FA) but not (to any considerable extent) by humic acid (HA) (Fig. 13A). This finding can be attributed to the larger molecular weight of FA than that of HA and phosphate and the greater electrostatic repulsion of FA than of HA. The density and protonation constant of the carboxyl groups in NOM also affect phosphate adsorption to goethite (Antelo et al., 2007; Fu et al., 2013; Ge et al., 2020; Wang et al., 2015). The carboxyl groups in NOM combine with the hydroxyl groups of goethite through electrostatic ligand exchange, occupying the adsorption sites on goethite and inhibiting phosphate adsorption (Deng et al., 2019; Groeneveld et al., 2020). An AFM analysis showed that NOM inhibits ICNs during the phosphate removal process (Chassé and Ohno, 2016). Furthermore, the sequential addition of phosphate and HA affects the phosphate adsorption capacity. Adding phosphate before HA exerts a larger effect than the simultaneous addition of phosphate and HA, which, in turn, exerts a greater effect than adding HA before phosphate (Fu et al., 2013). ICNs and mICNs display a notably strong adsorption capacity for hydrophobic NOM, which competes with phosphate for the active sites (Kaiser and Zech, 1997).

The HA concentration and crystal structural properties of ICNs and mICNs mainly influence phosphate adsorption on ICNs and mICNs. Low concentrations of HA (<0.5 mg/L) facilitate phosphate adsorption (Luo et al., 2021). For example, Xing et al. reported that phosphates are absorbed by siderite to form deprotonated BBC in the presence of 0.5 mg/L of HA (Xing et al., 2020). Phosphates are then transformed into deprotonated MMC when the concentration of HA is 10 mg/L. They found that carboxyl groups on the HA promote the chelation of the HA with siderite. Interestingly, phosphates and HA compete for limited adsorption sites on siderite. Chen and Sparks (2018) found that NOM suppresses the evolution of ferrihydrite to lepidocrocite or goethite. In the presence of HA at low concentrations, ferrihydrite more readily adsorbs phosphate than lepidocrocite and goethite because HA promotes phosphate removal from ferrihydrite. In addition, HA-modified magnetite (HA-MNP) exhibits a larger phosphate adsorption capacity (28.9 mg/g) than magnetite because phosphate and HA-MNP are strongly bound through electrostatic interactions (Rashid et al., 2017).

Aspartic acid (Yang et al., 2016), oxalic acid, ethanoic acid, citric acid (Geelhoed et al., 1998; Lindegren and Persson, 2009), hemimellitic acid, 1,2,4-benzenetricarboxylic acid, and mellitic acid (Lindegren and Persson, 2010) inhibit phosphate adsorption by goethite. Citric acid exerts the strongest inhibitory effect because it blocks the micropores of goethite and then hinders the diffusion of phosphate ions (Lindegren and Persson, 2009). Notably, sodium benzoate and phthalate do not affect phosphate adsorption on goethite due to their small molecular weights (Dorau et al., 2019; Lindegren and Persson, 2010). Overall, depending on the functional groups and specific ions involved, the co-existing ions in water environments have varying effects on the adsorption of phosphate by ICNs and mICNs. Some ions may exhibit inhibitory or promotional effects, while others may have no effect. Furthermore, even with the same co-existing ions, the removal efficiency may vary due to changes in ligands and metal ions in ICNs and mICNs. Current ICNs and mICNs often exhibit good selective adsorption of phosphate; thus, minimizing the impact of co-existing ions is necessary.

6.5. Other affecters

Crystallinity, SSA, light irradiation, and crystal size also influence phosphate adsorption to ICNs and mICNs (Torrent et al., 1992). The SSA of weakly crystalline ICNs gradually decreases during the aging process. A recent study reported that the structure stabilizes and phosphate adsorption becomes inhibited (Wang et al., 2013a). For example, Michel et al. (2010) reported a newly formed ferrihydrite with an SSA of 610 m^2/g, which is substantially larger than those of other ICNs such as nano-Fe_3O_4 (82.2 m^2/g) and α-Fe_2O_3 (106.9 m^2/g) (Mao et al., 2012; Wen-Xin et al., 2023). In addition, as the ferrihydrite crystal size increased from 1.6 nm to 4.4 nm, the SSA increased from 427 m^2/g to 234 m^2/g and the phosphate adsorption capacity decreased from 1690 μmol/g to 980 μmol/g. Fresh ferrihydrite achieves a higher reactivity than aged ferrihydrite due to its lower crystallinity and larger SSA (427 m^2/g) (Wang et al., 2013; Wang et al., 2013a). More importantly, ferrihydrite is unstable and tends to form thermodynamically stable hematite, goethite, and lepidocrocite, which release the initially precipitated phosphate (Senn et al., 2017) (Fig. 13B and C). A recent study found that photoreduction dissolution accelerates the release of Fe ions from ferrihydrite, promoting the co-adsorption of iron and phosphates and their consequent formation of ternary complexes/

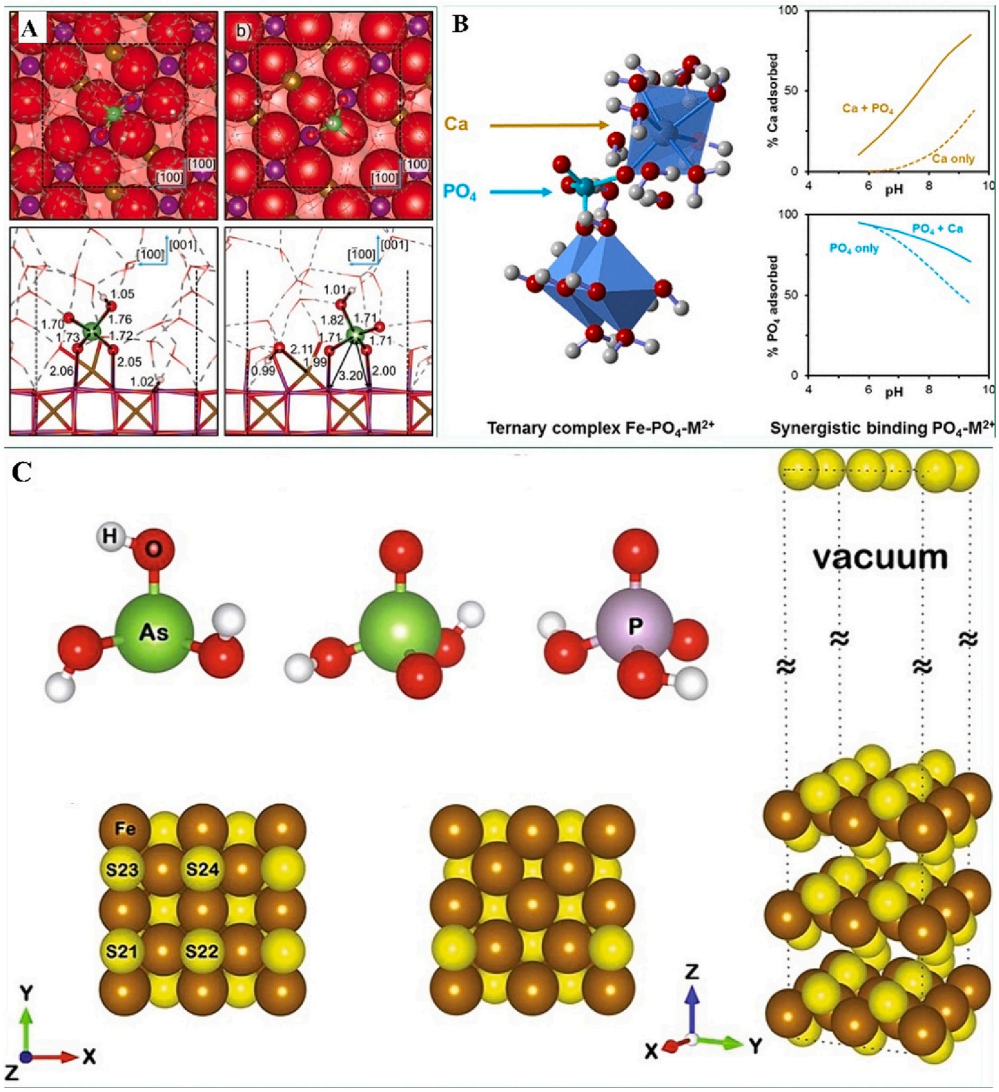

Fig. 12. (A)Schematic of competitive adsorption of phosphate and arsenate with magnetite (Liang et al., 2021); (B) schematic of the surface complexation process of phosphates forming ternary complexes with Ca, Mg ions and ferrihydrite (Mendez and Hiemstra, 2020); (C) schematic of competitive adsorption of phosphate and arsenic on pyrite (Han et al., 2020).

precipitates (Fig. 14A) (Lv et al., 2022). Notably, natural ICNs adsorb more phosphate (2.29 μm/m^2) than synthesized ICNs (1.04 μm/m^2) (Fig. 14B and C, respectively) (Dorau et al., 2019). Overall, in terms of natural surface water, multicomponent aqueous solutions, and wastewater, the study of SSA, co-existing ions, sunlight exposure, as well as the crystal size and crystallinity of ICNs and mICNs is crucial in phosphate management. Some conclusions can be drawn from the existing literature. However, effective research in this field is lacking; thus, further in-depth studies are necessary to investigate the impact of these factors.

7. Phosphate desorption from ICNs and mICNs

Desorption from phosphate-saturated ICNs and mICNs depends on the type and crystal structural properties of the desorbents.

7.1. Crystal structural properties

The crystal structures, chemical and physical properties, and crystallinities of the ICNs and mICNs influence phosphate desorption from the ICNs and mICNs. For example, the phosphate-adsorbing capacity of ferrihydrite exceeds that of magnetite, siderite, lepidocrocite, goethite, hematite, limonite, pyrite, and pyrrhotite, but the desorption capacity of phosphate-saturated ferrihydrite is low (Table 4), indicating a high proportion of obligatory adsorption (Arai and Sparks, 2007).

As previously mentioned, crystallinity affects desorption from phosphate-saturated ICNs and mICNs. One study (Arai and Sparks, 2007) revealed that the ratio of phosphate desorption from phosphate-saturated ferrihydrite declined from 4.81 % to 0.92 % between 2 days and 19 months at a pH of 7.5. Meanwhile, the desorption ratio reduced from 10.07 % to 3.83 % between 2 days and 10 months at a pH of 4. This decline is attributable to the precipitation or diffusion of the adsorbed phosphate in the micropores of ferrihydrite. Krumina et al. (2016) confirmed a substantially higher desorption rate from phosphate-saturated ferrihydrite than from phosphate-saturated goethite, which can be explained by the charge difference between saturated goethite and ferrihydrite; specifically, monoprotonated phosphate desorbs more slowly than deprotonated phosphate (Song et al., 2012; Wen et al., 2022).

7.2. Desorbents

ICNs and mICNs can be regenerated in desorbents such as acids, alkalis, and salts (He et al., 2022). In an alkaline solution, OH^- ions can be

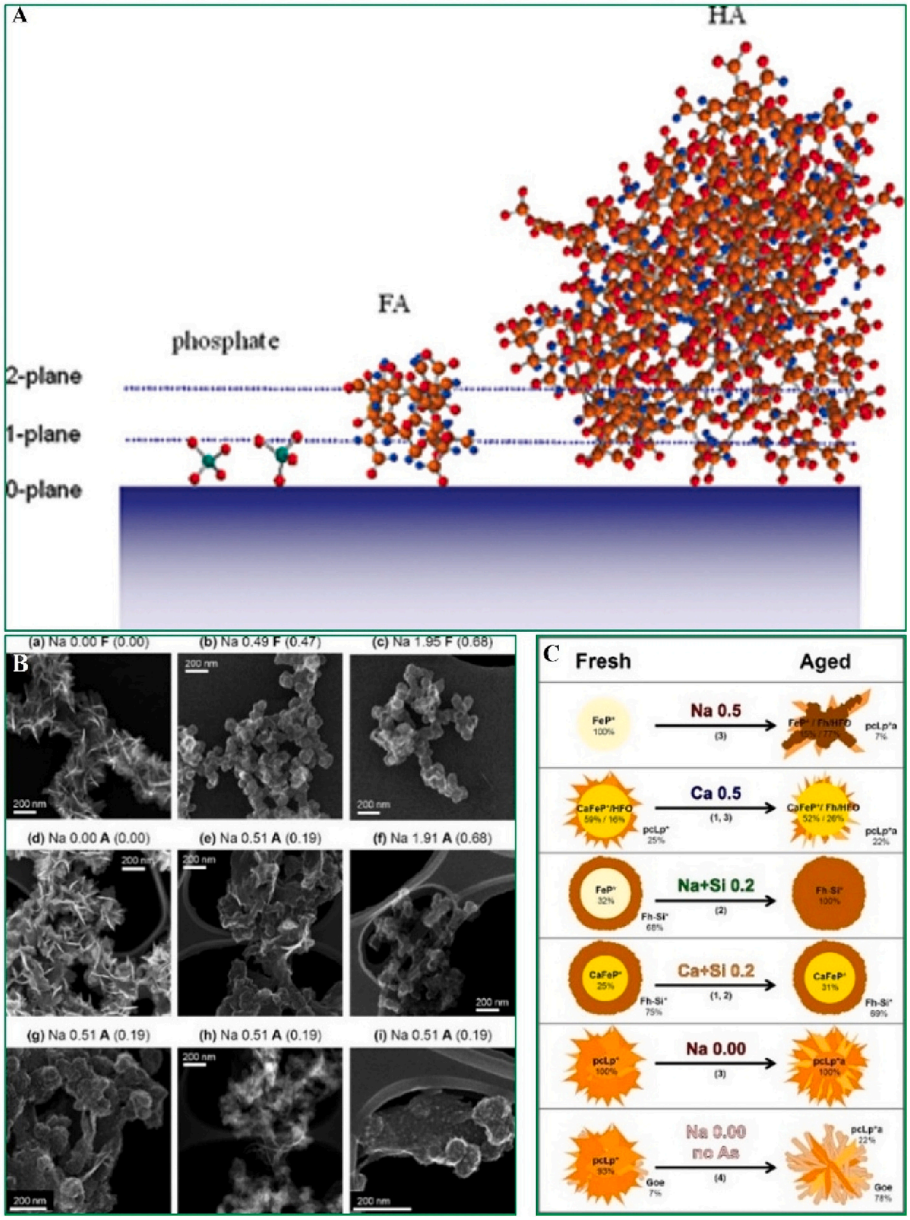

Fig. 13. (A) Phosphate and humic substances compete for adsorption on goethite: a conceptual diagram of the process (Weng et al., 2008); (B) and (C) the influence of phosphate retention on the aging process structure of Fe(III) precipitates formed by the oxidation of Fe(II) in water (Senn et al., 2017).

exchanged with phosphate. NaOH can regenerate highly crystalline goethite and 50 % of the phosphate from weakly crystalline goethite (Strauss et al., 1997). NaOH can also regenerate PAN/Fe_2O_3/TBAB after five consecutive cycles. A superior regenerative effect is observed at pH = 3 than at pH = 5 due to the regeneration resistance of iron–phosphate complexes formed through electrostatic ligand exchange at the lower pH at pH = 5 (Wang et al., 2021b). NaOH regenerates nano-Fe_3O_4 more efficiently than NH_4OH because NaOH can completely dissociate, creating higher concentrations of OH^- than NH_4OH (Zeng et al., 2004). Other studies reported that NaOH regenerates MLC (Hao et al., 2019) and MLC-La$(OH)_3$ (Song et al., 2020), but MLC maintains a higher recovery ratio (83 % after five cycles) than MLC-La$(OH)_3$ (74.9 % after four cycles).

Phosphate in salt solutions is desorbed via ion exchange. For example, $Na_2S_2O_8$ can be regenerated into ISMs. Nanostructured pyrrhotite regenerated with $Na_2S_2O_8$ delivers a high phosphate removal ratio (Chen et al., 2015). In the presence of KCl desorbent, the total phosphate desorption ratio increases in the following order: ferrihydrite (8.5 %) < goethite (10 %) < hematite (12.5 %) (Wang et al., 2013a). $CaCl_2$ can also regenerate ICNs, demonstrating a total phosphate desorption ratio of 10 %, 20 %, and 65 % on ferrihydrite, goethite, and hematite, respectively (Freese et al., 1999). The regeneration capability of HCl is higher on goethite with good crystallinity (phosphate removal ratio = 92 %) than on goethite with weak crystallinity (phosphate removal ratio = 67 %) (Strauss et al., 1997).

Oxalate, citrate acid, malonic acid disodium salt, cabozantinib malate, L(+)-tartaric acid, sumatriptan, $CaSO_4$, $CaCl_2$, HA, and 3-nitrosalicylaldehyde can also regenerate ICNs and mICNs (Gypser et al., 2019; Johnson and Loeppert, 2006). Notably, the regeneration ratio of low-molecular-weight organic acid to ferrihydrite and goethite is increased at pH = 4 (Johnson and Loeppert, 2006).

The above analysis concluded that NaOH can achieve higher desorption efficiency for the adsorption saturation of ICNs and mICNs compared to other desorption agents. However, most research reports show limited desorption cycles. Thus, future research should focus on developing high-performance ICNs and mICNs to extend their recovery,

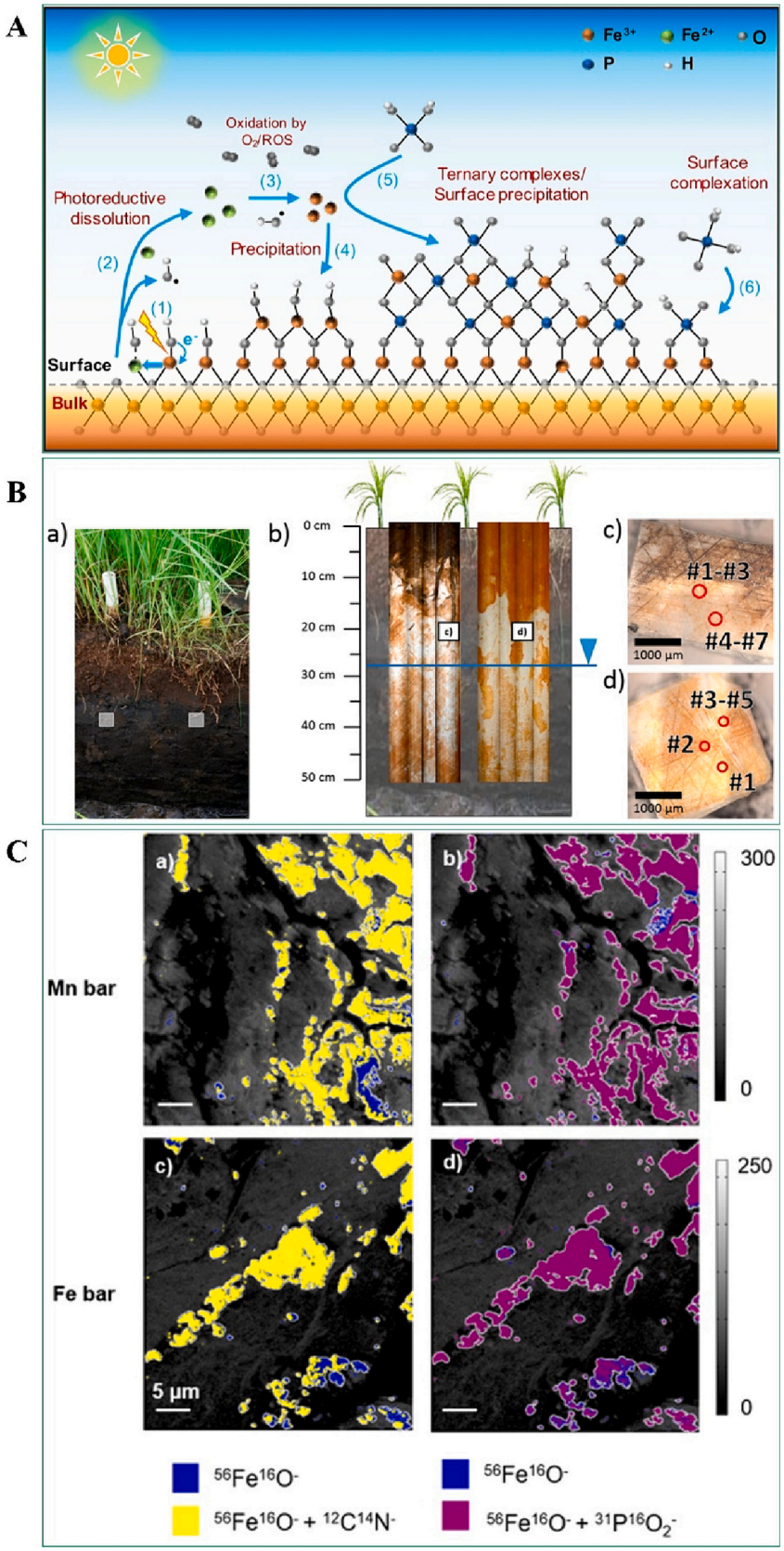

Fig. 14. (A) Schematic of mechanism of photoreduction and dissolution of phosphate adsorption on ferrihydrite (Lv et al., 2022); (B and C) schematic of in-situ adsorption of phosphate under soil by synthetic and natural ICNs (Dorau et al., 2019).

regeneration, and actual service life, which is crucial for the practical application and cost-benefit analysis of ICNs and mICNs.

8. Application of ICNs and mICNs to phosphate management

8.1. Management of municipal wastewater

The removal of low phosphate concentrations by urban sewage treatment plants remains challenging because low concentrations of phosphate cannot maintain sufficiently many and diverse microbial metabolisms. Therefore, the phosphate removal efficiency by microorganisms is low (Wang et al., 2021a). By contrast, the adsorption method effectively manages low concentrations of phosphate. In recent years, mICNs and ICNs have been widely used on a large scale for the deep treatment of municipal wastewater. The ICNs commonly used in municipal wastewater treatment include siderite (Xing et al., 2017), pyrite (Chen et al., 2015), and goethite (Liu, 2013). Raw ICNs have a low phosphate removal capacity, while modified ICNs can effectively enhance their affinity for adsorbing phosphate ions. The most commonly reported modification methods currently include thermal activation of ICN under different atmospheres (N_2, O_2, and H_2), the preparation of high-performance filtering media using composite natural minerals, or the application of sulfur- or calcium-containing minerals to achieve simultaneous nitrogen and phosphate removal (SNP) in municipal wastewater treatment. For example, Liu et al. applied H_2-calcined limonite (Liu et al., 2013b), O_2-calcined siderite (Xing et al., 2017), and N_2-calcined pyrite (Chen et al., 2015) for phosphate removal. They reported phosphate removals of 0.5–5 mg/L, reducing the phosphate concentration to below 0.02 mg/L. Bao et al. prepared porous magnetic ceramsite (Bao et al., 2019) and porous hematite ceramsite (Bao et al., 2016) as filtering media to achieve SNP from biological aeration filters.

The microorganism *Thiobacillus denitrificans* utilizes sulfur, Fe^0, or Fe^{2+} as electron donors for autotrophic denitrification. Accompanied by phosphate removal, the formation of $FePO_4$ precipitates, and SNP, the autotrophic denitrification process can oxidize ICNs and mICNs to produce Fe^{3+} and its oxyhydroxide (Yang et al., 2017). Pyrite has been applied in singular filter media (Di Capua et al., 2020; Kong et al., 2015; Li et al., 2022a; Li et al., 2022c; Zhu et al., 2023) or incorporated with other materials, such as nanostructured pyrrhotite (Yang et al., 2017), sulfur (Fig. 15A) (Kong et al., 2016; Lu et al., 2021; Chen et al., 2023), zeolite, ceramsite (Chen et al., 2020), corncob (Weng et al., 2022), volcanic rock (Xu et al., 2022), siderite (Yang et al., 2018), natural pyrrhotite (Li et al., 2016a; Zhang et al., 2019), mixed sulfur–siderite (Wang et al., 2019), mixed sulfur–limestone (Li et al., 2020b), or mixed N_2-calcined pyrite–hematite in a calcite (MMH) system (Li et al., 2022c). In powdered and granulated forms, these materials have been applied to SNP in autotrophic denitrification biofilters. Li et al. (2022a) recently reported that the MMH system achieves SNP more efficiently than the other systems mentioned above (Yang et al., 2017; Yang et al., 2018).

ICNs and mICNs have been utilized as substrates in constructed wetlands for the removal of phosphate through the synergistic actions of aquatic plants and microorganisms, offering an affordable and efficient wastewater treatment technology (Ge et al., 2019). Limonite (Fig. 15B) (Hu et al., 2021), natural pyrrhotite mixed with alum sludge (Fig. 15C) (Yang et al., 2021a), natural pyrite mixed with limestone (Fig. 15D) (Ge et al., 2019), natural pyrrhotite (Yang et al., 2021), and ceramsite mixed with magnetite (Dong et al., 2021) are commonly used substrates in constructed wetlands. Among these substrates, the combination of natural pyrite and alum sludge realized the highest phosphate removal ratio (98 %) at an initial phosphate concentration of 13–22 mg/L (Yang et al., 2021a).

8.2. Applications to lake phosphate management

Internal phosphate release and external phosphate input from sediments affect phosphate concentration in overlying water. The continuous release of residual phosphate in sediment causes a steady increase in phosphate concentration while the external phosphate input reduces (Sun et al., 2022). Controlling the release of sediment phosphate is necessary for minimizing internal phosphate loading and accelerating wastewater recycling. Phosphate release from lake sediments can be controlled in situ (Li et al., 2020a) or ex-situ (Yin et al., 2019). The ex-situ dredging process reduces phosphate release from sediment, whereas active end capping/modification are promising in-situ methods for reducing internal phosphate loading.

A phosphate locking agent (PLA) with high phosphate adsorption capacity can prevent the release of phosphate in sediments. The studied PLAs include Al-modified bentonite (Waajen et al., 2016), Al-modified clay mineral (Yang et al., 2020b), nano-Fe_3O_4 (Chen et al., 2021b), and ICNs and mICNs (ferrihydrite [Zou et al., 2017]). Among them, ICNs and mICNs have been recognized for their low cost and environmental friendliness, achieving a high interception efficiency of deposited phosphate release under aerobic conditions.

ICNs and mICNs can be divided into nonmagnetic and magnetic categories. Under aerobic conditions, ICNs and mICNs can effectively manage phosphate in sediments through electrostatic adsorption and precipitation mechanisms. However, under anaerobic conditions, Fe^{3+} oxide/hydroxide adsorbed phosphate can migrate through the overlying and interstitial water due to the reduction of Fe^{3+} to Fe^{2+} by microorganisms (Lin et al., 2023). The application of nonmagnetic ICNs and mICNs is generally difficult to recover. Nonmagnetic ICNs and mICNs left in sediment can effectively fix phosphorus. However, under the alternating aerobic and anaerobic redox conditions in sediment, the fixed phosphorus may migrate or be released into overlying and interstitial water. Magnetic ICNs and mICNs can be employed to overcome the inhibition of phosphorus release by non-magnetic ICNs and mICNs in sediment. The most effective method for recovering magnetic ICNs and mICNs involves magnetic separation of gradients (Lin et al., 2023). For example, Lin et al. (2023) demonstrated that magnetite is more effective in controlling the release of internal phosphates from lakes into the overlying water compared to hematite and goethite. This finding indicates the superior capability of magnetite to control eutrophication. Lin et al. also recently showed that ferrihydrite-modified magnetite composites can control the endogenous phosphate release into OW in an anoxic environment, achieving effective recovery (Lin et al., 2023a).

8.3. Management of eutrophic seawater

Phytoplankton growth is inhibited by oxidative phosphorylation when it adsorbs phosphorus in the ocean. The amount of phosphate ingested by marine organisms depends on the species, biological absorption, intensity of the source, and removal by precipitation of debris and self-generated particulate matter. The diagenetic behavior of phosphate is related to the chemical and physical properties of ICNs (Sanders and Windom, 1980).

ICNs and mICNs have been recently applied to control seawater eutrophication due to their economic and safety advantages. The main ones include goethite (Gao and Mucci, 2003), akageneite (Chitrakar et al., 2006), and g-C_3N_4 modified hematite (Gamshadzehi et al., 2019). For example, competition for the goethite adsorption sites by species with high ionic strength influences phosphate adsorption from seawater by goethite. Balistrieri and Murray (1981) characterized the surface chemical properties of goethite in seawater. Research has shown that the surface complexation model can effectively simulate the competitive adsorption of SO_4^{2-}, Ca^{2+}, and Mg^{2+} in goethite in a single adsorbent system in seawater. In a high pH water environment, a three-layer model was used to simulate the titration of goethite surface charge. Hawke et al. (1989) studied the adsorption of phosphate on goethite in a seawater environment. They found that equilibrium constants obtained from a three-layer model did not match the adsorption data of phosphate on goethite obtained from seawater ions in a single adsorbent system. Gao and Mucci (2001) studied the competitive adsorption process of

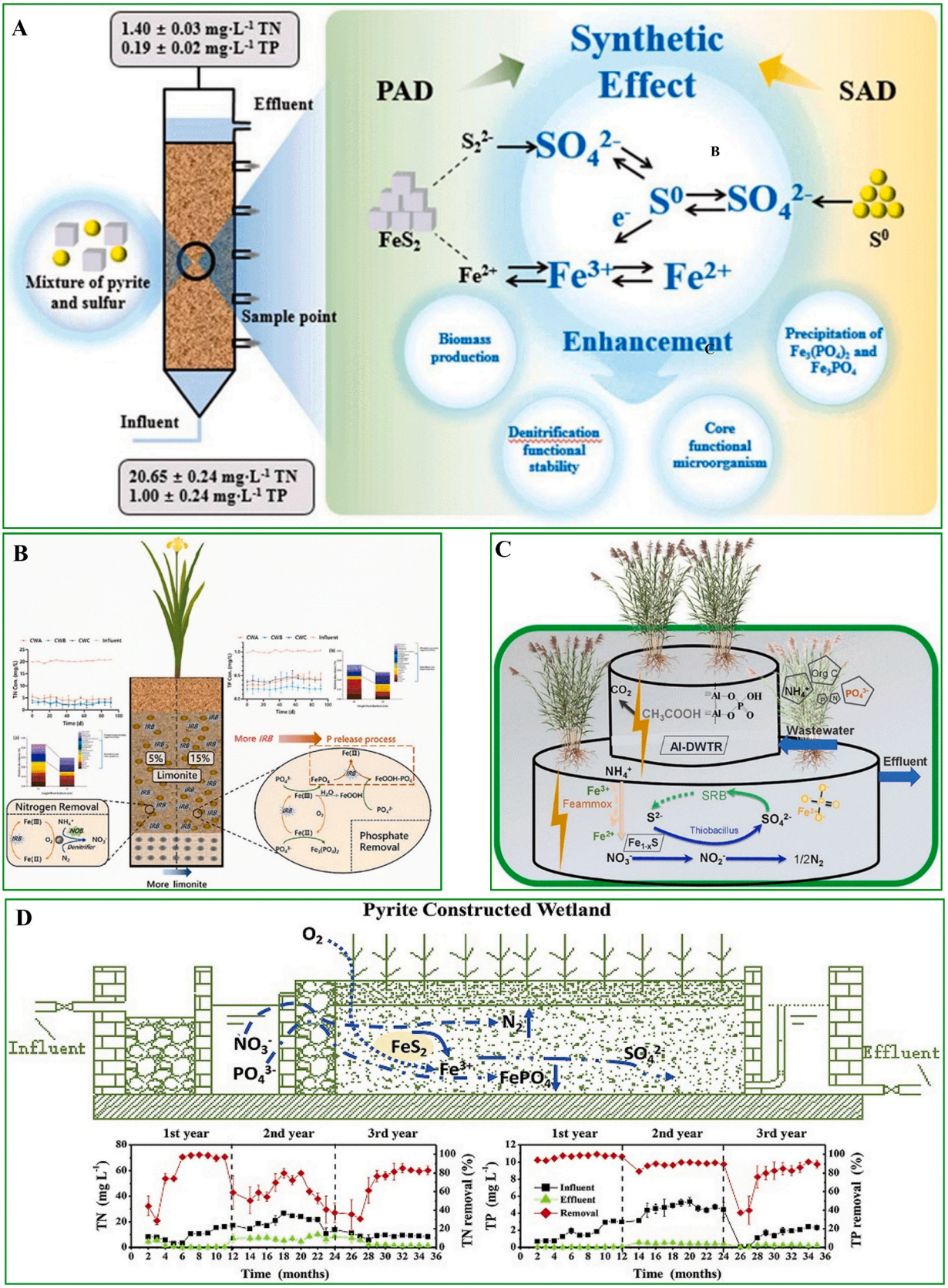

Fig. 15. (A) Schematic of coupled pyrite and sulfur for N and P removal (Chen et al., 2023); (B) schematic of limonite in a constructed wetland system (Hu et al., 2021); (C) schematic of pyrrhotite mixed with alum sludge in a constructed wetland system (Yang et al., 2021a); (D) schematic of simultaneous N and P removal in constructed wetland system using natural pyrite mixed with limestone as substrate (Ge et al., 2019).

goethite for arsenate and phosphate in a sodium chloride solution (0.7 M). A constant capacitance model of three monodentate surface complexes was constructed to describe the adsorption process of goethite for arsenate and phosphate in a single adsorbate system. Developing ICNs and mICNs for seawater eutrophication treatment is a reasonable future research direction.

8.4. Application of ICNs and mICNs to phosphate crop fertilizers

Phosphate-loaded ICNs and mICNs have been applied to agriculture. The high iron and nutrient contents of ICNs and mICNs can increase soil fertility, enhance the nutrient binding capacity, and promote plant growth. For example, Guzman et al. (1994) found that goethite adsorbs a lower proportion of phosphate than hematite. Moreover, plants grown in hematite-supplemented soil will more likely obtain phosphate than those grown in goethite-supplemented soil. Zhang et al. reported that α-FeOOH-600BC recovered 967.5 mg/kg of phosphate from urine, indicating that phosphate-saturated α-FeOOH-600BC can act as a slow-release fertilizer (Zhang et al., 2021b). Boutchuen et al. (2019) demonstrated that phosphate-adsorbed goethite can supply phosphate fertilizers to crops and that phosphate uptake is improved by adding limestone to reduce soil acidity. However, further research is necessary from theoretical, modeling, experimental, and technical perspectives to study the release of phosphates from adsorbed phosphate in ICNs and mICNs into plants. More importantly, further investigation into environmental and ecological safety issues, as well as the release of metal ions into plants and soil, is crucial. In addition, appropriate guidance/policies must be established by the government to regulate the use of ICNs and mICNs as agricultural phosphate fertilizers.

8.4.1. Influence of ICNs and mICNs on soil microflora and aquatic organisms

This section mainly summarizes the positive or negative impacts of ICNs and mICNs on aquatic organisms and soil microbial communities, evaluates the toxic mechanisms of ICNs and mICNs at the cellular level, and comprehensively conducts environmental risk assessments to demonstrate the sustainability and safety of applying ICNs and mICNs in agricultural production (Tao et al., 2023a).

(1) Positive effects on soil microflora and aquatic organisms

ICNs and mICNs have a positive impact on soil microorganisms. Specifically, ICNs and mICNs can promote the growth of anaerobic microorganisms. ICNs and mICNs can serve as solid electron shuttles, further facilitating inter-species direct interspecies electron transfer (DIET) among anaerobic bacterial populations (Fu et al., 2019; Huang et al., 2020). After adding Fe_3O_4, *Methanosarcina*, and *Methanosaeta*, Fe_3O_4 can stimulate DIET in methanogenic bacteria, and dominate throughout the culture process, leading to a tenfold increase in biomass compared to cultures without Fe_3O_4 (Huang et al., 2020; Rotaru et al., 2014a; Rotaru et al., 2014b).

ICNs and mICNs promote the growth of soil-related microorganisms that benefit plant growth and carbon cycling, with the exception of anaerobic microorganisms. For example, Fe_3O_4 can stimulate the growth of microorganisms in agricultural soil, including populations of *Burkholderia Paraburkholderia* (increased from 1.50 % to 2.09 %), *Rhizobium* and (increased from 1.41 % to 1.74 %), *Pantoea* (increased from 1.31 % to 2.22 %), *Chitinophaga sancti* (increased from 1.12 % to 2.08 %), and *Nocardioides* (increased from 1.63 % to 1.77 %) (Zhang et al., 2020). In addition, ICNs and mICNs have positive effects on soil microorganisms, including decomposing organic matter in soil, alleviating the stress of heavy metals on microorganisms in soil, providing nutrients for soil microorganisms, and promoting their growth. For example, Fe_3O_4 can synergistically enhance the efficient degradation of β-keratinase, leading to an increase in the population of microorganisms in soil (Rai and Mukherjee, 2015). α-Fe_2O_3 can increase the activity of *Pseudomonas jinjuensis* by 7.9 %, as it reduces the toxicity of arsenic in soil by 82.5 % (Lee et al., 2020). The latest research shows that iron nanoparticles can absorb more beneficial microorganisms, enhance competition and cooperation among microbial populations, effectively improve the functionality of rhizosphere microorganisms of alfalfa, and promote the growth of alfalfa (Figs. 14[B] and 16[A]) (Zhang et al., 2024). Additionally, studies have also found that nanomaterials such as selenium nanomaterials (Figs. 14[D] and 16[C] (Jiao et al., 2023) and Nano-MoS_2 (Fig. 16[E]) (Li et al., 2024) promote microbial activity, thereby promoting the growth of rice and soybeans.

In addition to microorganisms and plants, invertebrates are also found in soil (such as earthworms and nematodes). Whether ICNs and mICNs have a positive impact on these microorganisms remains unclear, and further research is needed. Studies have shown that *E. coli* can produce siderophores and enrich Fe^{3+} from the surrounding environment, allowing *Caenorhabditis elegans* to further promote the enrichment of iron and growth using the iron carrier (Kim, 2018). This finding indicates that ICNs and mICNs could serve as a source of iron carriers for soil invertebrates. In addition, the demand for iron by soil invertebrates is relatively limited; thus, further controlling the content of ICNs and mICNs in soil is crucial for ecological balance. Properly measured ICNs and mICNs can ensure the safety of soil invertebrates and maintain the stability of the soil ecosystem. However, ICNs and mICNs can have

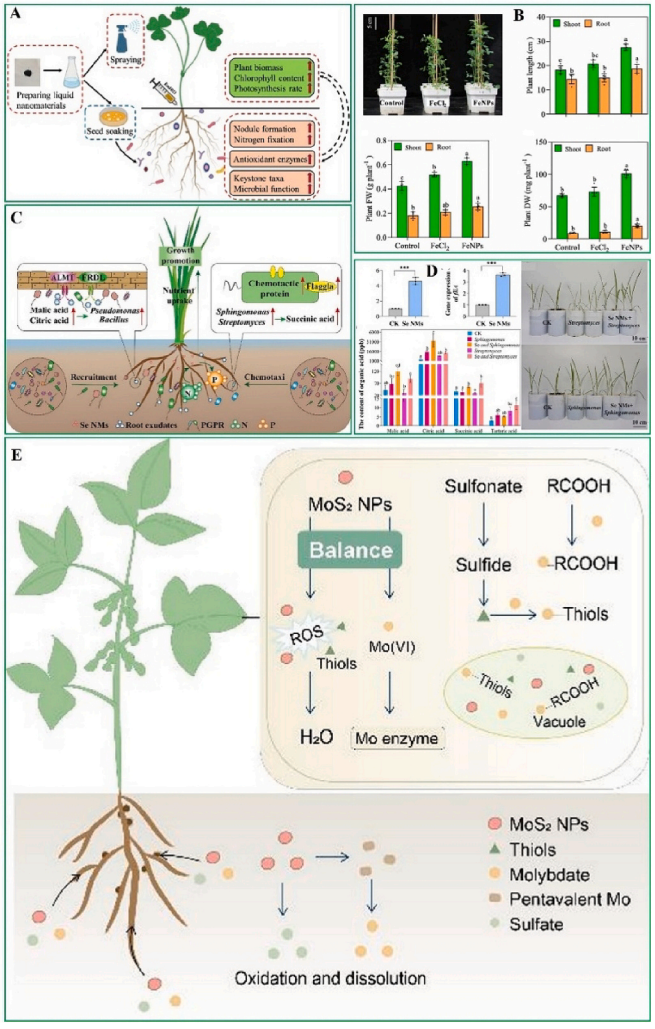

Fig. 16. (A and B) Schematic of iron nanomaterials promote root growth of alfalfa in soil (Zhang et al., 2024); (C and D) schematic of selenium nanomaterials promoting rice growth in soil (Jiao et al., 2023); (E) Schematic of the promotion of soybean growth by nano-MoS_2 in soil (Li et al., 2024).

negative effects on soil microorganisms, as well as aquatic organisms, invertebrates, and plants. This effect will be systematically discussed in the next section. The application of ICNs and mICNs in soil fertilizers can provide valuable insights and ensure ecological safety.

(2) Detrimental effects on soil microflora and aquatic organisms

The negative impact of ICNs and mICNs on soil biota is worth studying and thus cannot be ignored. ICNs and mICNs have a considerable impact on soil microbial activity and biomass production. For example, hematite (2000 $mg \cdot kg^{-1}$) reduced the mineralization of grass clippings in sandy soil (60 % decrease within 180 days compared to 90 days), as well as the carbon content of grass clippings (30 % decrease within 180 days, 28 % decrease within 90 days) and the quantity of fungi, bacteria, and microbial biomass (49 % decrease within 180 days, 27 % decrease within 90 days) (Rashid et al., 2017a). ICNs and mICNs inhibit microbial growth and are toxic to microbes. For example, the addition of magnetite (1000 ppm) reduced the growth rate of *Pseudomonas aeruginosa*. Additionally, hematite exhibited remarkable inhibitory effects on *Escherichia coli*, *Staphylococcus aureus*, *Serratia marcescen*, and *Pseudomonas aeruginosa* (Ismail et al., 2015). In addition to reducing microbial activity and biomass and inhibiting growth, ICNs and mICNs also have an impact on the structure of soil microbial communities (Bhalerao, 2019; Lee et al., 2020). Studies have shown that exposure to Fe_3O_4 can lead to changes in the relative abundance of metabolites in maize rhizosphere soil, with the abundance of iron-oxidizing and -reducing bacterium *Sediminibacterium* decreasing from 2.15 % to 2.07 % and the abundance of nitrogen-fixing bacterium *Bradyrhizobium* decreasing from 2.94 % to 2.40 % (Zhang et al., 2020). Another study revealed that the C/N ratio of soil microbial biomass stabilized around 10 after nine weeks but increased to 17 in the first week (Antisari et al., 2013). The considerable changes in C/N ratio may be attributed to changes in the ratio of fungal biomass to bacterial biomass because reports have indicated that the C/N ratio of bacteria (3–6) is lower than that of fungi (5–15) (Antisari et al., 2013; Paul and Clark, 1989). The changes in the structure of soil microbial communities caused by ICNs and mICNs will markedly impact nutrient cycling, energy flow, decomposition, soil ecosystem stability, and soil biodiversity.

ICNs and mICNs can also have certain impacts on aquatic organisms. For example, Nations et al. (2011) revealed that the addition of hematite at 0.001 mg/L can shorten the snout–vent length (SVL) of African clawed frog tadpoles. SVL increases with the addition of hematite at 1 mg/L. Compared to the control group, the body length of African clawed frog tadpoles is also significantly reduced ($p \leq 0.033$) when exposed to hematite at a concentration of 1000 mg/L. Another study found that hematite at a concentration of 1 mg/L also affects ion regulation, biochemical, enzymatic parameters, and hematological parameters in the major Indian carp *Labeorohita* after 96 h of static exposure (Saravanan et al., 2011). This finding indicates the high toxicity of hematite to aquatic microorganisms and animals in aquatic environments (Saravanan et al., 2011). Overall, the release of ICNs and mICNs into the ecological environment may be harmful to a variety of ecologically related organisms, plants, animals, and aquatic animals. However, further research on the impact of ICNs and mICNs on soil microbial communities and aquatic organisms is highly necessary.

8.5. Environmental geochemical implications of the phosphate cycle and ICNs

The interaction between ICNs and phosphates affects the phosphate cycle of the Earth. ICNs can be converted via the following two mechanisms: (1) Fe(II) or Fe(III) precipitation during rock weathering and (2) solid-state processing or reprecipitation/dissolution of precursor iron oxides (Fig. 17A) (Barrón and Torrent, 2013; Cornell and Schwertmann, 2003).

Hematite and goethite undergo thermodynamically stable hydrolysis, oxidation, dehydration, dehydroxylation, redissolution, and crystallization reactions (Fig. 17B). The precursor (ferrihydrite) is transformed to hematite or goethite through reprecipitation and dissolution processes involving aggregation, dehydration, and rearrangement. Maghemite, magnetite, and lepidocrocite are formed through other pathways and can persist over the long term in soil (Barrón and Torrent, 2013). At phosphate/Fe atomic ratios lower than 2.5 %, the crystallization product is a twinned goethite crystal with a hematite core. Crystallization products form in alkaline media, but spindle-shaped hematite crystals appear in acidic media (Barrón and Torrent, 2013; Schwertmann and Murad, 1983). Phosphate adsorption hinders the aggregation of hematite, which reaches 2.5 % (Barrón and Torrent, 2013; Barrón et al., 1997). Ordered ferrimagnetic ferrihydrite is formed at temperatures above 100 °C and then converted to hematite (Barrón and Torrent, 1996; Barrón et al., 2003; Barrón and Torrent, 2013). Phosphate delays or inhibits the crystallization of ferrihydrite (Barrón et al., 1997). Goethite crystallization during the conversion and oxidation of Fe(II) salts is prevented in the presence of phosphate. Cumplido et al. (2000) obtained the ferrihydrite of platy lepidocrocite, which is soluble at phosphate/Fe ratios above 2 % and has a large SSA. Barrón et al. (2006) observed that hematite nanoparticles adsorb phosphates, develop ionic strength, and promote incompatible jarosite iron dissolution under acidic conditions. Furthermore, jarosite on the surface of Mars is possibly caused by hematite symbiosis.

Fe(II) minerals and NZVI originating from submicron magnetite were recently discovered in lunar soil. Sulfides on the lunar surface underwent complex gas–liquid reactions during the impact process. Fe—O dissolved into sulfides, thereby forming submicron-sized magnetite and elemental iron through the eutectoid reaction (Fig. 17C) (Guo et al., 2022). Disproportionation of micrometeorite impact-induced Fe(II) can produce numerous Fe(III) products, including nanophase metallic iron ($npFe^0$) (Fig. 17D) (Xian et al., 2023). Twenty-four types of minerals have been found in lunar soil, including ilmenite, titanium oxide, and hydroxyapatite. The Moon became enriched in minerals (or molecules) containing potassium, rare earth elements, and phosphate during its evolution (Fig. 17E) (Yao et al., 2022). Overall, ICNs are not only abundant in sediments and soils but are also present in air and water, as evidenced by their generation within organisms. ICNs play a crucial role in the lunar iron and biogeochemical cycles, influencing the adsorption and transport of nutrients and redox processes.

9. Future perspectives

Future research focuses on the selectivity and capacity for phosphate adsorption of ICNs and mICNs. Combining or developing advanced technologies from other fields is necessary to study high-performance adsorption materials, mainly in the following areas:

(1) The removal efficiency of phosphates will generally decrease as the pH of the water environment increases, which will be a major limitation to their application. Phosphates in solutions may compete with hydroxyl groups for limited adsorption sites, leading to a decreasing trend in ligand exchange reactions between phosphates and metal species under alkaline conditions. Additionally, a considerable risk of leaching of metal elements emerges in high-pH water environments, which can negatively affect phosphate removal and cause secondary pollution to the environment. Therefore, further expanding the scope of research is mainly focused on stability and adaptability under alkaline conditions.
(2) From the perspective of economic feasibility, the recyclability of ICNs and mICNs is a key factor in evaluating adsorbents. The recovery of phosphate resources from desorption solutions saturated with ICNs and mICNs is a problem. The proper disposal of waste ICNs and mICNs remains an issue worth exploring. More importantly, the desorption solutions of phosphate-saturated

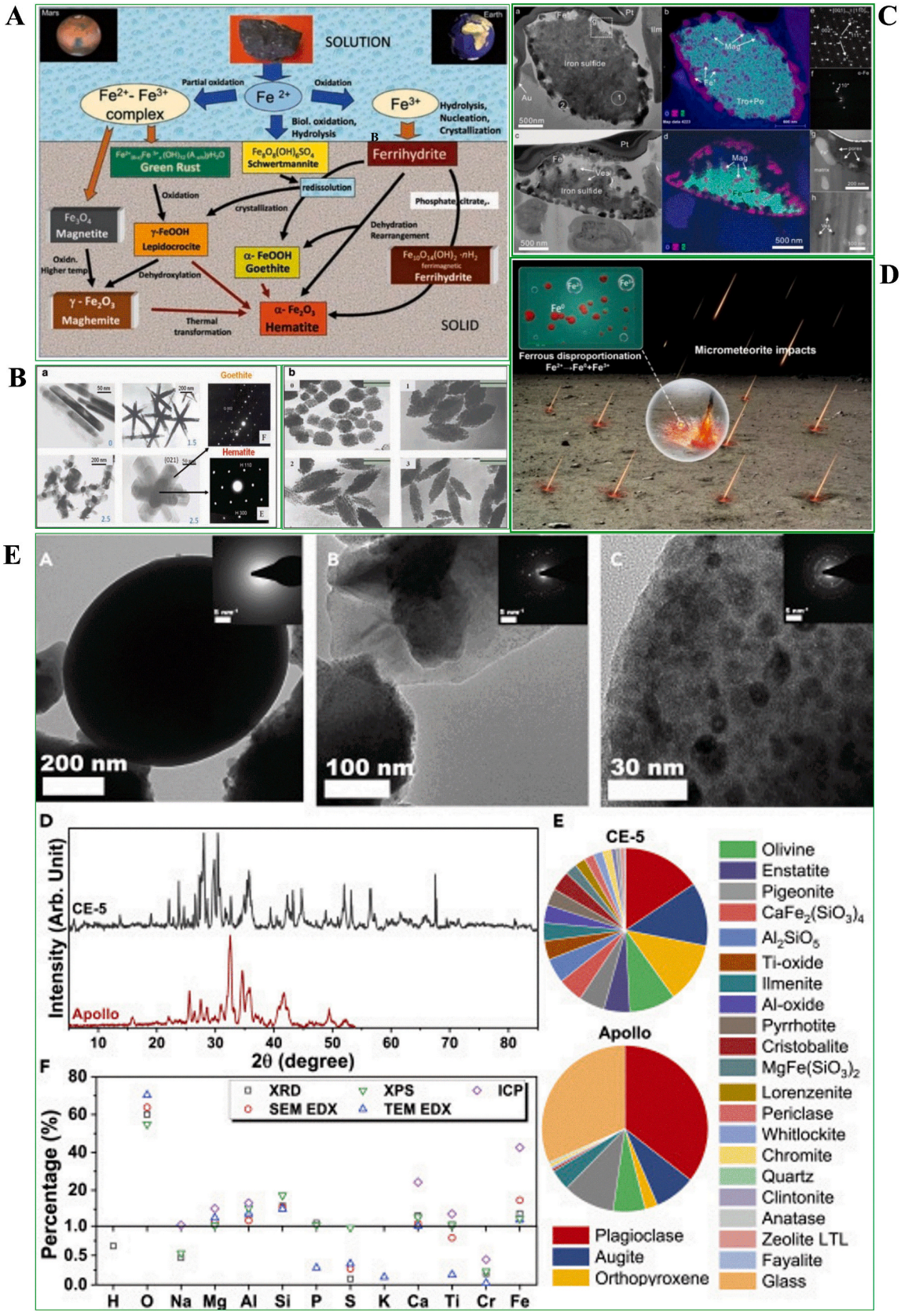

Fig. 17. (A) Schematic of transformation and formation pathways of ICNs (Barrón and Torrent, 2013); (B) electron diffraction and TEM images showing the chemical properties of ICNs (Barrón and Torrent, 2013); (C) schematic of spherical iron-sulfide nanoparticles research (Guo et al., 2022); (D) schematic of the ferrous disproportionation reaction caused by a micrometeorite impact (Xian et al., 2023); (E) characterization of CE-5 (lunar soil samples) and comparison with Apollo-12 (lunar soil samples) (Yao et al., 2022);

ICNs and mICNs contain a substantial amount of phosphate, which is a valuable resource. Thus, efficient recovery and concentration of desorption solutions pose a major challenge and require additional research efforts. Future research should also consider the separation of spent ICNs and mICNs, with filtration and centrifugation as the basic methods for solid–liquid separation. Although solid–liquid separation using filtration methods may be affected by membrane pore blockage and pollution, centrifugation requires additional investment costs, leading to further energy consumption. While the construction of magnetic ICN and mICN adsorption reaction systems is feasible, further research is still needed.

(3) Starting from the surface modification and preparation methods, combining large SSA and easily adjustable internal crystal structures based on ICNs and mICNs is a new research direction. For example, modified ICNs can be prepared into array and core–shell structures, and high-performance adsorbents can then be obtained using new preparation or modification methods such as nano-confinement, topology, and defects, exploring the adsorption mechanism. In addition, when preparing multidimensional mICNs, which generally comprise multiple crystal faces, the properties of the crystal faces will determine the individual performance of mICNs. The area of catalytic degradation of organic pollutants has received extensive research attention, and its related mechanisms have been determined. However, in the field of adsorption agents, further research is needed on the adsorption performance between crystal faces and phosphate ions (Fig. 3). Currently, the required functions for high-performance phosphate removal cannot be achieved using a single material or structure. This approach requires structurally designed and complex multifunctional materials with multiple components. The synthesized and modified multimetal mICNs will inherit the adsorption performance of single ligands while exhibiting efficient synergistic effects and achieving high phosphate removal efficiency. Notably, additional effort should be invested in further research in the future.

(4) mICNs can effectively adsorb phosphates through a chemical adsorption process, and future strategies will combine physical–chemical processes with biological processes to improve phosphate removal efficiency. For example, self-nitrifying mineral materials based on ICNs can be further developed and applied to municipal wastewater with low carbon-to-nitrogen ratios to achieve SNP. Additionally, consideration should be given to the application of ICNs and mICNs as substrates in constructed wetlands, as phosphorus sequestrants in nutrient-rich lake sediments, and in the control of eutrophication in seawater. Further research and exploration are necessary to develop low-cost materials and low-toxicity ICNs and mICNs for effective use as agricultural phosphorus fertilizers to promote plant growth. Further evaluation should also be conducted on the impact of ICNs and mICNs on soil microorganisms, soil invertebrates, and aquatic organisms. Additionally, supplementary research is needed to assess the effects of competing substances (anions, cations, and NOM) on the phosphate immobilization technology by ICNs and mICNs in the management of municipal wastewater, eutrophic lakes, and marine eutrophication. The following research directions are particularly important: the role of phosphate immobilization technology by ICNs and mICNs in biological communities in lakes and seawater, as well as their long-term application in sediment, and the combined application of ICN– and mICN–phosphate immobilization in underwater and plant restoration techniques. They should be considered as the main research directions for the future.

(5) The rapid development of ICNs presents remarkable opportunities for water treatment applications. However, in practical water treatment, ICNs encounter bottlenecks such as easy aggregation leading to deactivation, operational difficulties, and potential safety risks. One of the most effective strategies to address these bottlenecks is to prepare composite materials with a nanoscale confinement structure by fixing ICNs in nanochannels of suitable carriers. However, research on the nanoscale confinement effect directly related to the pollutant removal process of composite nanomaterials is generally limited, especially regarding the limited understanding of the confinement effects on the structure and performance of ICNs during their growth process (Wang et al., 2024). For example, Wang et al. (2024) studied nanoscale iron oxide for water treatment purposes using track-etched (TE) membranes as confinement carriers. They also investigated for the first time the evolution of the structure of ICNs in TE membrane nanochannels of different sizes and their influence on the adsorption of As(V) (Figs. 18. [A] and [B]). Their study revealed that nanoscale confinement led to a change in the structural transformation pathway during the aging process of ICNs, from ferrihydrite to goethite rather than hematite in an open system. Nanoscale confinement substantially slowed down the phase transition kinetics of ferrihydrite, and this unique structural evolution characteristic is beneficial for the long-term stable application of ICN nanoparticles in the field of water treatment (such as As(V) adsorption). Future work based on this study applied to phosphate management can effectively address eutrophication control.

(6) Future research should clarify the differences in phosphate adsorption between weak and pure crystalline systems. Ferrihydrite often co-precipitates with various anions and cations in the environment, releasing and migrating during the transformation or reduction of ferrihydrite. The transformation of this ferrihydrite and the forms of related elements should be investigated in future research. Given the discovery of ICNs and phosphate–ICNs in lunar soil, their sources should be evaluated, and the interactions between phosphate and ICNs on the moon should be elucidated. Phosphates play an important evolutionary role in planetary bodies. Thus, studying this role will help further evaluate the impact of phosphates.

(7) Thus far, several applications of mICNs in phosphate adsorption have been reported, wherein each type of mICN demonstrates a wide range of different modification and synthesis parameter indexes. Therefore, identifying the factors (mICN use, mICN properties, and modification conditions) is necessary to further determine the optimal adsorption conditions and environment for the same type of mICNs. Traditional data analysis methods will encounter considerable challenges at present due to the relatively complex adsorption reaction system and large amount of data. Therefore, the use of machine learning (ML) methods can effectively overcome obstacles and will become the main direction and trend of future research. ML can collect representative and in-depth experimental data to further reveal hidden adsorption mechanisms and treatment effects, thereby providing targeted guidance for the synthesis and modification of mICNs. By contrast, in the field of preparation and design of mICNs, introducing a large amount of experimental data on modification parameters can help predict the chemical function, composition, and modification methods of mICN structures, as well as the parameters of DFT molecular calculations (adsorption energy, bond angle, and bond length). Appropriate and reasonable calculations can effectively and quickly determine the optimal design scheme for modified ICNs, thereby saving cost and time. Moreover, such calculations can directly determine and predict the adsorption form and capacity of mICNs in the loaded reaction system, design different algorithms to further explain the adsorption model, and further establish the adsorption site and reaction mechanism of functional groups. The efficient and accurate operation of ML depends mainly on the breadth and depth

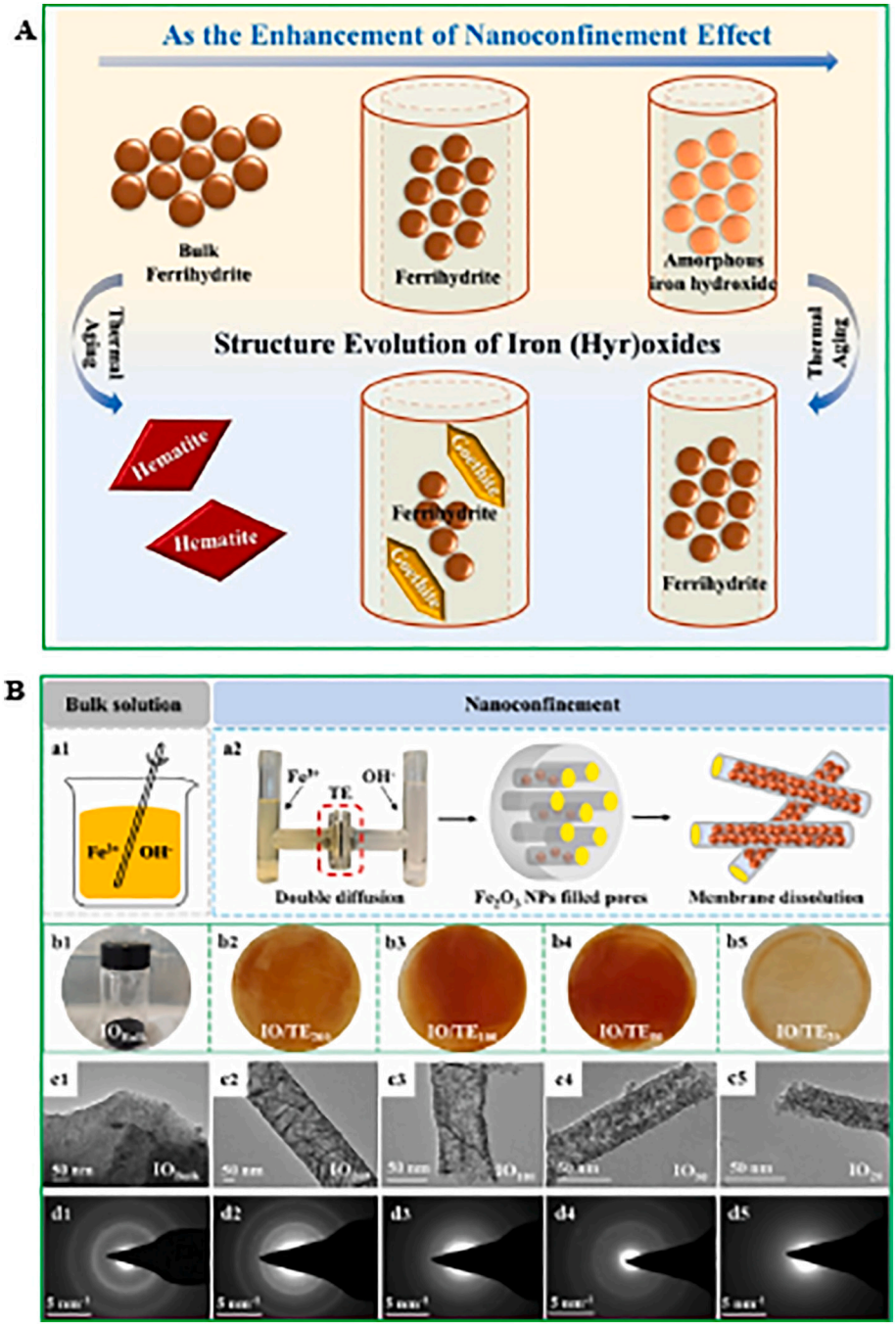

Fig. 18. (A) and (B) Schematic of the evolution of the microscopic structure of iron-based hydroxides under nano-confinement and its significance for wastewater treatment (Wang et al., 2024).

of the imported reaction data and, more importantly, the depth of understanding of the problem and literature. However, at present, the vast majority of experimental data only reports successful cases without reporting failed cases, thereby limiting challenges in the data collected via ML. In addition, the reliability of the ML fitting results may be low due to the significant differences in experimental handling conditions, experimental procedures, and experimental environments for each mICN. Therefore, instances of experimental failures should be considered as future research directions, and the results of these failed studies should be reported, leading to further modifications of the treatment environment to improve the maturity of ML operations.

10. Conclusions

This review comprehensively summarizes the updated research on ICNs and mICNs used in phosphate management through adsorption. Ferrihydrite, which is characterized by its low crystallinity, active sites, large SSA, and superior phosphate removal ratio compared to other minerals such as goethite, hematite, siderite, pyrite, pyrrhotite, and magnetite, is proven to be an effective adsorbent for phosphate. ICNs often undergo physical or chemical modification to enhance their phosphate binding capacity. mICNs demonstrate high affinities for phosphate. The primary mechanisms for phosphate removal by ICNs and mICNs involve electrostatic ligand exchange, surface precipitation, surface complexation, and electrostatic attraction. The impact of ionic

strength on phosphate removal by ICNs and mICNs depends on the complexation mode with phosphate, the pH of the water environment, and the inhibitory effect of anions due to their charge density and competitive interaction with phosphate. By contrast, cations promote phosphate removal by ICNs and mICNs because they act as effective active sites. High concentrations and molecular weights of NOMs inhibit phosphate removal by ICNs and mICNs. Thus, ICNs and mICNs are effective in managing municipal wastewater, eutrophic lakes, and eutrophic seawater. ICNs and mICNs can also be used as phosphate fertilizers after reaching phosphate saturation. However, they may have positive and negative effects on soil microorganisms and aquatic organisms. Thus, utilizing ICNs and mICNs for phosphate management is an effective strategy to address eutrophication and the phosphate resource crisis in the water environment.

CRediT authorship contribution statement

Teng Bao: Writing – original draft, Methodology, Investigation, Formal analysis, Data curation, Conceptualization. **Mekdimu Mezemir Damtie:** Resources, Methodology, Investigation, Formal analysis. **Chu Yan Wang:** Supervision, Resources, Funding acquisition. **Cheng Long Li:** Investigation. **Zhijie Chen:** Validation, Methodology, Investigation, Formal analysis, Conceptualization. **Kuk CHO:** Writing – review & editing, Supervision, Methodology, Investigation. **Wei Wei:** Software, Resources, Methodology, Formal analysis, Data curation. **Peng Yuan:** Visualization, Validation, Software, Resources, Methodology, Data curation, Conceptualization. **Ray L. Frost:** Writing – review & editing, Validation, Supervision, Software, Project administration, Methodology. **Bing-Jie Ni:** Writing – review & editing, Supervision, Project administration, Funding acquisition.

Declaration of competing interest

We declare that we have no financial and personal relationships with other people or organizations that can inappropriately influence our work, there is no professional or other personal interest of any nature or kind in any product, service and/or company that could be construed as influencing the position presented in, or the review of, the manuscript entitled, “Iron-containing nanominerals for sustainable phosphate management: A comprehensive review and future perspectives”.

Data availability

Data will be made available on request.

Acknowledgment

This research was supported by Anhui Province Excellent Research and Innovation Team Project for Universities (Grant No. 2023AH010050); Natural Science Research Project of Anhui Educational Committee (Grant No. 2023AH052170); and Science Research Project of Hefei University (Grant No. 20RC42).

References

Abdala, D., Northrup, P., Arai, Y., 2015. Surface loading effects on orthophosphate surface complexation at the goethite/water interface as examined by extended X-ray Absorption Fine Structure (EXAFS) spectroscopy. J. Colloid Interface Sci. 437, 297–303.
Abdala, D., Northrup, P., Vicentin, F., 2015a. Residence time and pH effects on the bonding configuration of orthophosphate surface complexes at the goethite/water interface as examined by Extended X-ray Absorption Fine Structure (EXAFS) spectroscopy. J. Colloid Interface Sci. 442, 15–21.
Abu-Obaid, S., Aktij, S., Tabe, S., Sadrzadeh, M., Farnood, R., 2022. Surfactant-modified adsorptive electrospun nanofiber membrane impregnated with akageneite for phosphorus recovery from wastewater. J. Environ. Chem. Eng. 10 (6), 108786.
Adam, N., 2017. A wet-chemical and phosphorus K-edge X-ray absorption near edge structure investigation of phosphate adsorption on binary mixtures of ferrihydrite and calcite: implications for phosphorus bioavailability. Soil Sci. Soc. Am. J. 81 (5), 1079–1087.
Ahmed, A., Gypser, S., Leinweber, P., Freese, D., Kühn, O., 2019. Infrared spectroscopic characterization of phosphate binding at the goethite-water interface. Phys. Chem. Chem. Phys. 21 (8), 4421–4434.
Ahmed, S., Lo, I.M., 2020. Phosphate removal from river water using a highly efficient magnetically recyclable $Fe_3O_4/La(OH)_3$ nanocomposite. Chemosphere 261, 128118.
Ajmal, Z., Muhmood, A., Usman, M., Kizito, S., Lu, J.X., Dong, R.J., Wu, S.B., 2018. Phosphate removal from aqueous solution using iron oxides: adsorption, desorption and regeneration characteristics. J. Colloid Interface Sci. 528, 145–155.
Almanassra, I.W., Mckay, G., Kochkodan, V., Atieh, M.A., Al-Ansari, T., 2021. A state-of-the-art review on phosphate removal from water by biochars. Chem. Eng. J. 409, 128211.
Ammary, B.Y., 2004. Nutrients requirements in biological industrial wastewater treatment. Afr. J. Biotechnol. 3 (4), 236–238.
Anschutz, A., Penn, R., 2005. Reduction of crystalline iron (III) oxyhydroxides using hydroquinone: influence of phase and particle size. Geochem. Trans. 60, 1–7.
Antelo, J., Avena, M., Fiol, S., 2005. Effects of pH and ionic strength on the adsorption of phosphate and arsenate at the goethite-water interface. J. Colloid Interface Sci. 285 (2), 476–486.
Antelo, J., Arce, F., Avena, M., 2007. Adsorption of a soil humic acid at the surface of goethite and its competitive interaction with phosphate. Geoderma 138 (1/2), 12–19.
Antelo, J., Fiol, S., Pérez, C., 2010. Analysis of phosphate adsorption onto ferrihydrite using the CD-MUSIC model. J. Colloid Interface Sci. 347 (1), 112–119.
Antelo, J., Arce, F., Fiol, S., 2015. Arsenate and phosphate adsorption on ferrihydrite nanoparticles. Synergetic interaction with calcium ions. Chem. Geol. 410, 53–62.
Antisari, L.V., Carbone, S., Gatti, A., Vianello, G., Nannipieri, P., 2013. Toxicity of metal oxide (CeO_2, Fe_3O_4, SnO_2) engineered nanoparticles on soil microbial biomass and their distribution in soil. Soil Biol. Biochem. 60, 87–94.
Arai, Y., Sparks, D., 2001. ATR-FTIR spectroscopic investigation on phosphate adsorption mechanisms at the ferrihydrite-water interface. J. Colloid Interface Sci. 241 (2), 317–326.
Arai, Y., Sparks, D., 2007. Phosphate reaction dynamics in soils and soil components: a multiscale approach. Adv. Agron. 94, 135–179.
Arroyave, J., Puccia, V., Zanini, G., Avena, M., 2018. Surface speciation of phosphate on goethite as seen by infrared surface titrations (IRST). Spectrochim. Acta A 199, 57–64.
Atkinson, R., Parfitt, R., Smart, R., 1974. Infrared study of phosphate adsorption on goethite. J. Chem. Soc. Faraday Trans. 1 Phys. Chem. Condens. Phases 70, 1472–1479.
Baalousha, M., Desmau, M., Singerling, S.A., Webster, J.P., Matiasek, S.J., Stern, M.A., Alpers, C.N., 2022. Discovery and potential ramifications of reduced iron-bearing nanoparticles-magnetite, wüstite, and zero-valent iron-in wildland-urban interface fire ashes. Environ. Sci. Nano 9 (11), 4136–4149.
Bacelo, H., Pintor, A., Santos, S., Boaventura, R., Botelho, C., 2020. Performance and prospects of different adsorbents for phosphorus uptake and recovery from water. Chem. Eng. J. 381, 122566.
Baek, G., Kim, J., Lee, C., 2019. A review of the effects of iron compounds on methanogenesis in anaerobic environments. Renew. Sust. Energ. Rev. 113.
Balboni, E., Smith, K., Moreau, L., 2020. Transformation of ferrihydrite to goethite and the fate of plutonium. ACS Earth Space Chem. 4 (11), 1993–2006.
Balistrieri, L.S., Murray, J.W., 1981. The surface chemistry of goethite (a-FeOOH) in major ion seawater. Am. J. Sci. 281 (6), 788–806.
Banfield, J., Zhang, H., 2001. Nanoparticles and the environment. Rev. Mineral. Geochem. 44 (1), 1–58.
Bao, T., Chen, T., Tan, J., Wille, M., Zhu, D., Chen, D., Xi, Y., 2016. Synthesis and performance of iron oxide-based porous ceramsite in a biological aerated filter for the simultaneous removal of nitrogen and phosphorus from domestic wastewater. Sep. Purif. Technol. 167, 154–162.
Bao, T., Damtie, M., Yu, Z., Liu, Y., Jin, J., Wu, K., Ni, B., 2019. Green synthesis of Fe_3O_4@carbon filter media for simultaneous phosphate recovery and nitrogen removal from domestic wastewater in biological aerated filters. ACS Sustain. Chem. Eng. 7 (19), 16698–16709.
Barrón, V., Torrent, J., 1996. Surface hydroxyl configuration of various crystal faces of hematite and goethite. J. Colloid Interface Sci. 177 (2), 407–410.
Barrón, V., Torrent, J., 2013. Iron, manganese and aluminium oxides and oxyhydroxides. EMU Notes Miner. 14 (9), 297–336.
Barron, V., Herruzo, M., Torrent, J., 1988. Phosphate adsorption by aluminous hematites of different shapes. Soil Sci. Soc. Am. J. 52 (3), 647–651.
Barrón, V., Galvez, N., Hochella, M., Torrent, J., 1997. Epitaxial overgrowth of goethite on hematite synthesized in phosphate media; a scanning force and transmission electron microscopy study. Am. Mineral. 82 (11–12), 1091–1100.
Barrón, V., Torrent, J., De, Grave, 2003. Hydromaghemite, an intermediate in the hydrothermal transformation of 2-line ferrihydrite into hematite. Am. Mineral. 88 (11–12), 1679–1688.
Barrón, V., Torrent, J., Greenwood, J., 2006. Transformation of jarosite to hematite in simulated Martian brines. Earth Planet Sci. Lett. 251 (3–4), 380–385.
Barrow, N., Bowden, J., Posner, A., 1980. Describing the effects of electrolyte on adsorption of phosphate by a variable charge surface. Aust. J. Soil. Res. 18 (4), 395–404.
Belloni, C., Korving, L., Witkamp, G., Brück, E., Dugulan, A., 2023. Effect of goethite doping using elements with different preferential oxidation states for improved reversible phosphate adsorption. J. Environ. Chem. Eng. 11 (5), 110505.
Benjamin, M., Leckle, J., 1982. Effect of complexation by Cl^-, SO_4^-, and $S_2O_3^-$ on adsorption behavior of Cd on oxide surfaces. Environ. Sci. Technol. 16, 162–170.

Bhalerao, T.S., 2019. Magnetic nanostructures: environmental and agricultural applications. In: Magnetic Nanostructures: Environmental and Agricultural Applications, pp. 213–224.
Bonneville, S., Cappellen, P., Behrends, T., 2004. Microbial reduction of iron (III) oxyhydroxides: effects of mineral solubility and availability. Chem. Geol. 212 (3–4), 255–268.
Bose, S., Hochella Jr., M., Gorby, Y., Kennedy, D., McCready, D., Madden, A., Lower, B., 2009. Bioreduction of hematite nanoparticles by the dissimilatory iron reducing bacterium *Shewanella oneidensis* MR-1. Geochim. Cosmochim. Acta 73 (4), 962–976.
Boutchuen, A., Zimmerman, D., Aich, N., Masud, A., Arabshahi, A., Palchoudhury, S., 2019. Increased plant growth with hematite nanoparticle fertilizer drop and determining nanoparticle uptake in plants using multimodal approach. J. Nanomater. 1–11.
Bradford, S.A., Segal, E., Zheng, W., Wang, Q., Hutchins, S.R., 2008. Reuse of concentrated animal feeding operation wastewater on agricultural lands. J. Environ. Qual. 37 (S5), S97–S115.
Bustillo-Lecompte, C., Mehrvar, M., 2015. Slaughterhouse wastewater characteristics, treatment, and management in the meat processing industry: a review on trends and advances. J. Environ. Manage. 161, 287–302.
Byrne, J., Klueglein, N., Pearce, C., Rosso, K., Appel, E., Kappler, A., 2015. Redox cycling of Fe(II) and Fe(III) in magnetite by Fe-metabolizing bacteria. Science 347 (6229), 1473–1476.
Cai, T., Park, S.Y., Li, Y., 2013. Nutrient recovery from wastewater streams by microalgae: status and prospects. Renew. Sustain. Energy Rev. 19, 360–369.
Cai, W., Fu, F., Zhu, L., Tang, B., 2019. Simultaneous removal of chromium (VI) and phosphate from water using easily separable magnetite/pyrite nanocomposite. J. Alloys Compd. 803, 118–125.
Caraballo, M., Asta, M., Perez, J., Hochella Jr., M., 2022. Past, present and future global influence and technological applications of iron-bearing metastable nanominerals. Gondw. Res. 110, 283–304.
Chassé, A., Ohno, T., 2016. Higher molecular mass organic matter molecules compete with orthophosphate for adsorption to iron (oxy)hydroxide. Environ. Sci. Technol. 50 (14), 7461–7469.
Chen, C., Sparks, D., 2018. Fe(II)-induced mineral transformation of ferrihydrite-organic matter adsorption and co-precipitation complexes in the absence and presence of As (III). Soil Sci. Soc. Am. J. 2 (11), 1095–1101.
Chen, T., Wang, J., Wang, J., Xie, J., Zhu, C., Zhan, X., 2015. Phosphorus removal from aqueous solutions containing low concentration of phosphate using pyrite calcinate sorbent. Int. J. Environ. Sci. Technol. 12, 885–892.
Chen, T., Shi, Y., Liu, H., Chen, D., Li, P., Yang, Y., Zhu, X., 2016. A novel way to prepare pyrrhotite and its performance on removal of phosphate from aqueous solution. Decalin. Water Treat. 57 (50), 23864–23872.
Chen, Y., Shao, Z., Kong, Z., Gu, L., Fang, J., Chai, H., 2020. Study of pyrite based autotrophic denitrification system for low-carbon source stormwater treatment. J. Water Process Eng. 37, 101414.
Chen, M., Li, X., Zhang, Q., Wang, C., Hu, H., Wang, Q., Zeng, C., 2021a. Phosphate removal from aqueous solution by electrochemical coupling siderite packed column. Chemosphere 280, 130805.
Chen, X., Liu, L., Yan, W., Li, M., Xing, X., Li, Q., Zhu, L., Wu, T., He, X., 2021b. Effects of nFe_3O_4 capping on phosphorus release from sediments in a eutrophic lake. Environ. Sci. Pollut. Res. 28, 47056–47065.
Chen, P., Song, D., Zhang, X., Xie, Q., Zhou, Y., Liu, H., Rosso, K., 2022. Understanding competitive phosphate and silicate adsorption on goethite by connecting batch experiments with density functional theory calculations. Environ. Sci. Technol. 56 (2), 823–834.
Chen, P., Zhou, Y., Xie, Q., Chen, T., Liu, H., Xue, S., Rosso, K., 2022a. Phosphate adsorption kinetics and equilibria on natural iron and manganese oxide composites. J. Environ. Manage. 323, 116222.
Chen, W., Li, H., He, B., Tao, L., 2022b. Influence of co-existing anions and cations on phosphate sequestration onto goethite. Ecol. Environ. Sci. 31 (1), 151–159.
Chen, Z., Pang, C., Wen, Q., 2023. Coupled pyrite and sulfur autotrophic denitrification for simultaneous removal of nitrogen and phosphorus from secondary effluent: feasibility, performance and mechanisms. Water Res. 120422.
Cheng, D., Ngo, H., Guo, W., Liu, Y., Zhou, J., Chang, S., Nguyen, D., Bui, X., Zhang, X., 2018. Bioprocessing for elimination antibiotics and hormones from swine wastewater. Sci. Total Environ. 621, 1664–1682.
Cheng, P., Chen, T., Zou, X., Liu, H., Chen, D., Xie, J., 2017. Removal of phosphate by thermally activated limonite. J. Chin. Ceram. Soc. 45 (7), 1010–1016.
Chitrakar, R., Tezuka, S., Sonoda, A., Sakane, K., Ooi, K., Hirotsu, T., 2006. Phosphate adsorption on synthetic goethite and akaganeite. J. Colloid Interface Sci. 298 (2), 602–608.
Collins, C., Ragnarsdottir, K., Sherman, D., 1999. Effect of inorganic and organic ligands on the mechanism of cadmium sorption to goethite. Geochim. Cosmochim. Acta 63, 2989–3002.
Colombo, C., Barron, V., Torrent, J., 1994. Phosphate adsorption and desorption in relation to morphology and crystal properties of synthetic hematites. Geochim. Cosmochim. Acta 58 (4), 1261–1269.
Cornell, R.M., Schwertmann, U., 2003. The iron Oxides: Structure, Properties, Reactions, Occurrences, and Uses, Vol. 664. Wiley-Vch, Weinheim.
Cumplido, J., Barrón, V., Torrent, J., 2000. Effect of phosphate on the formation of nanophase lepidocrocite from Fe(II) sulfate. Clay Clay Miner. 48, 503–510.
Dai, R., Wang, P., Jia, P., Zhang, Y., Chu, X., Wang, Y., 2016. A review on factors affecting microcystins production by algae in aquatic environments. World J. Microb. Biot. 32 (51), 1–7.
Davis, M.L., 2010. Water and Wastewater Engineering: Design Principles and Practice. McGraw-Hill.
Delgadillo-Velasco, L., Hernandez-Montoya, V., Rangel-Vazquez, N.A., Cervantes, F.J., Montes-Moran, M.A., Del Rosario Moreno-Virgen, M., 2018. Screening of commercial sorbents for the removal of phosphates from water and modeling by molecular simulation. J. Mol. Liq. 262, 443–450.
Deng, Y., Li, Y., Li, X., Sun, Y., Ma, J., Lei, M., Weng, L., 2018. Influence of calcium and phosphate on pH dependency of arsenite and arsenate adsorption to goethite. Chemosphere 199, 617–624.
Deng, Y., Weng, L., Li, Y., 2019. Understanding major NOM properties controlling its interactions with phosphorus and arsenic at goethite-water interface. Water Res. 157, 372–380.
Di Bella, M., Pirajno, F., Sabatino, G., Quartieri, S., Barbieri, R., Cavalazzi, B., Italiano, F., 2021. Rolling ironstones from earth and mars: terrestrial hydrothermal ooids as a potential analogue of martian spherules. Minerals 11 (5), 460.
Di Capua, F., Mascolo, M., Pirozzi, F., Esposito, G., 2020. Simultaneous denitrification, phosphorus recovery and low sulfate production in a recirculated pyrite-packed biofilter (RPPB). Chemosphere 255, 126977.
Di, H., Cameron, K., 2002. Nitrate leaching and pasture production from different nitrogen sources on a shallow stoney soil under flood-irrigated dairy pasture. Soil Res. 40 (2), 317–334.
Diaz-Barrientos, E., Madrid, L., Contreras, M., Morillo, E., 1990. Simultaneous adsorption of zinc and phosphate on synthetic lepidocrocite. Aust. J. Soil. Res. 28, 549–557.
Dideriksen, K., Stipp, S., 2003. The adsorption of glyphosate and phosphate to goethite: a molecular-scale atomic force microscopy study. Geochim. Cosmochim. Acta 67 (18), 3313–3327.
Dong, L., Qi, Z., Li, M., Zhang, Y., Chen, Y., Qi, Y., Wu, H., 2021. Organics and nutrient removal from swine wastewater by constructed wetlands using ceramsite and magnetite as substrates. J. Environ. Chem. Eng. 9 (1), 104739.
Dong, S., Li, X., Wang, S., Zhang, D., Chen, Y., Xiao, F., Wang, Y., 2023. Adsorption-electrochemical mediated precipitation for phosphorus recovery from sludge filter wastewater with a lanthanum-modified cellulose sponge filter. Sci. Total Environ. 898, 165545.
Dorau, K., Pohl, L., Just, C., 2019. Soil organic matter and phosphate sorption on natural and synthetic Fe oxides under in situ conditions. Environ. Sci. Technol. 53 (22), 13081–13087.
Duenas, J., Alonso, J., Rey, A., Ferrer, A., 2003. Characterisation of phosphorous forms in wastewater treatment plants. J. Hazard. Mater. 97 (1–3), 193–205.
Echigo, T., Hatta, T., Nemoto, S., Takizawa, S., 2012. X-ray photoelectron spectroscopic study on the goethites with variations in crystallinity and morphology: their effects on surface hydroxyl concentration. Phys. Chem. Miner. 39, 769–778.
Elzinga, E., Kretzschmar, R., 2013. In situ ATR-FTIR spectroscopic analysis of the co-adsorption of orthophosphate and Cd(II) onto hematite. Geochim. Cosmochim. Acta 117, 53–64.
Elzinga, E., Sparks, D., 2007. Phosphate adsorption onto hematite: an in situ ATR-FTIR investigation of the effects of pH and loading level on the mode of phosphate surface complexation. J. Colloid Interface Sci. 308 (1), 53–70.
Eynde, E., Hiemstra, T., Comans, R., 2022. Interaction of Zn with ferrihydrite and its cooperative binding in the presence of PO_4. Geochim. Cosmochim. Acta 320, 223–237.
Fang, L., Liu, R., Li, J., Xu, C., Huang, L.Z., Wang, D., 2018. Magnetite/lanthanum hydroxide for phosphate sequestration and recovery from lake and the attenuation effects of sediment particles. Water Res. 130, 243–254.
Farfan, G., Wang, S., Ma, H., Caracas, R., Mao, W., 2012. Bonding and structural changes in siderite at high pressure. Am. Mineral. 97 (8–9), 1421–1426.
Freese, D., Weidler, P., Grolimund, D., 1999. A flow-through reactor with an infinite sink for monitoring desorption processes. J. Environ. Qual. 28 (2), 537–543.
Fu, H., Yang, Y., Zhu, R., Liu, J., Usman, M., Chen, Q., He, H., 2018. Superior adsorption of phosphate by ferrihydrite-coated and lanthanum-decorated magnetite. J. Colloid Interface Sci. 530, 704–713.
Fu, L., Zhou, T., Wang, J., You, L., Lu, Y., Yu, L., Zhou, S., 2019. $NanoFe_3O_4$ as solid electron shuttles to accelerate acetotrophic methanogenesis by methanosarcina barkeri. Front. Microbiol. 10, 388.
Fu, Z., Wu, F., Song, K., 2013. Competitive interaction between soil-derived humic acid and phosphate on goethite. Appl. Geochem. 36, 125–131.
Gamshadzehi, E., Nassiri, M., Ershadifar, H., 2019. One-pot synthesis of microporous Fe_2O_3/g-C_3N_4 and its application for efficient removal of phosphate from sewage and polluted seawater. Colloids Surf. A 567, 7–15.
Gao, Y., Mucci, A., 2001. Acid base reactions, phosphate and arsenate complexation, and their competitive adsorption at the surface of goethite in 0.7 M NaCl solution. Geochim. Cosmochim. Acta 65, 23612378.
Gao, Y., Mucci, A., 2003. Individual and competitive adsorption of phosphate and arsenate on goethite in artificial seawater. Chem. Geol. 199 (1–2), 91–109.
Ge, X., Wang, L., Zhang, W., 2020. Molecular understanding of humic acid-limited phosphate precipitation and transformation. Environ. Sci. Technol. 54 (1), 207–215.
Ge, Z., Wei, D., Zhang, J., Hu, J., Liu, Z., Li, R., 2019. Natural pyrite to enhance simultaneous long-term nitrogen and phosphorus removal in constructed wetland: three years of pilot study. Water Res. 148, 153–161.
Geelhoed, J., Hiemstra, T., van Riemsdijk, W., 1998. Competitive interaction between phosphate and citrate on goethite. Environ. Sci. Technol. 32 (14), 2119–2123.
Groeneveld, M., Catalán, N., Attermeyer, K., 2020. Selective adsorption of terrestrial dissolved organic matter to inorganic surfaces along a boreal inland water continuum. J. Geophys. Res. Biogeo. 125 (3).
Grzmil, B., Wronkowski, J., 2006. Removal of phosphates and fluorides from industrial wastewater. Desalination 189 (1–3), 261–268.
Guo, Z., Li, C., Li, Y., Wen, Y., Wu, Y., Jia, B., Tai, K., Zeng, X., Li, X., Liu, J., Ouyang, Z., 2022. Sub-microscopic magnetite and metallic iron particles formed by eutectic reaction in Chang'E-5 lunar soil. Nat. Commun. 13 (1), 7177.

Gustafsson, J., Antelo, J., 2022. Competitive arsenate and phosphate adsorption on ferrihydrite as described by the CD-MUSIC model. ACS Earth Space Chem. 6 (5), 1397–1406.
Guzman, G., Alcantara, E., Barron, V., Torrent, J., 1994. Phytoavailability of phosphate adsorbed on ferrihydrite, hematite, and goethite. Plant and Soil 159, 219–225.
Gypser, S., Schütze, E., Freese, D., 2019. Crystallization of single and binary iron- and aluminum hydroxides affect phosphorus desorption. J. Plant Nutr. Soil Sci. 182 (5), 741–750.
Han, C., Lalley, J., Iyanna, N., Nadagouda, M.N., 2017. Removal of phosphate using calcium and magnesium-modified iron-based adsorbents. Mater. Chem. Phys. 198, 115–124.
Han, Y., Park, J., Min, Y., Lim, D., 2020. Competitive adsorption between phosphate and arsenic in soil containing iron sulfide: XAS experiment and DFT calculation approaches. Chem. Eng. J. 397, 125426.
Hao, H., Wang, Y., Shi, B., 2019. NaLa$(CO_3)_2$ hybridized with Fe_3O_4 for efficient phosphate removal: synthesis and adsorption mechanistic study. Water Res. 155, 1–11.
Hawke, D., Carpenter, P.D., Hunter, K.A., 1989. Competitive adsorption of phosphate on goethite in marine electrolytes. Environ. Sci. Technol. 23 (2), 187–191.
He, Q., Zhao, H., Teng, Z., Wang, Y., Li, M., Hoffmann, M., 2022. Phosphate removal and recovery by lanthanum-based adsorbents: a review for current advances. Chemosphere 303, 134987.
Hiemstra, T., van Riemsdijk, W., 1996. A surface structural approach to ion adsorption: the charge distribution (CD) model. J. Colloid Interface Sci. 179 (2), 488–508.
Hiemstra, T., van Riemsdijk, W., 2009. A surface structural model for ferrihydrite I: sites related to primary charge, molar mass, and mass density. Geochim. Cosmochim. Acta 73 (15), 4423–4436.
Hinkle, M., Wang, Z., Giammar, D., 2015. Interaction of Fe(II) with phosphate and sulfate on iron oxide surfaces. Geochim. Cosmochim. Acta 158, 130–146.
Hsu, L., Tzou, Y., Ho, M., Sivakumar, C., Cho, Y., Li, W., Liu, Y., 2020. Preferential phosphate sorption and Al substitution on goethite. Environ. Sci. Nano. 7 (11), 3497–3508.
Hu, X., Wan, X., Tan, W., Xie, H., Zhuang, L., Zhang, J., Hu, Z., 2021. More is better? Constructed wetlands filled with different amount of Fe oxides showed opposite phosphorus removal performance. J. Clean. Prod. 329, 129749.
Huang, J., Ma, K., Xia, X., Gao, K., Lu, Y., 2020. Biochar and magnetite promote methanogenesis during anaerobic decomposition of rice straw. Soil Biol. Biochem. 143, 107740.
Huang, X., 2004. Intersection of isotherms for phosphate adsorption on hematite. J. Colloid Interface Sci. 271 (2), 296–307.
Huang, X., Hou, X., Zhao, J., 2016. Hematite facet confined ferrous ions as high efficient Fenton catalysts to degrade organic contaminants by lowering H_2O_2 decomposition energetic span. Appl. Catal. B Environ. 181, 127–137.
Huang, X., Hou, X., Jia, F., 2017. Ascorbate-promoted surface iron cycle for efficient heterogeneous Fenton alachlor degradation with hematite nanocrystals. ACS Appl. Mater. Interfaces 9 (10), 8751–8758.
Ismail, R.A., Sulaiman, G.M., Abdulrahman, S.A., Marzoog, T.R., 2015. Antibacterial activity of magnetic iron oxide nanoparticles synthesized by laser ablation in liquid. Mater. Sci. Eng. C 53, 286–297.
Jaiswal, A., Banerjee, S., Mani, R., Chattopadhyaya, M., 2013. Synthesis, characterization and application of goethite mineral as an adsorbent. J. Environ. Chem. Eng. 1 (3), 281–289.
Jang, M., Min, S., Kim, T., 2006. Removal of arsenite and arsenate using hydrous ferric oxide incorporated into naturally occurring porous diatomite. Environ. Sci. Technol. 40 (5), 1636–1643.
Jiang, W., Lv, J., Luo, L., Yang, K., Lin, Y., Hu, F., Zhang, J., Zhang, S., 2013. Arsenate and cadmium co-adsorption and co-precipitation on goethite. J. Hazard. Mater. 262, 55–63.
Jiao, L., Cao, X., Wang, C., Chen, F., Zou, H., Yue, L., Wang, Z., 2023. Crosstalk between in situ root exudates and rhizobacteria to promote rice growth by selenium nanomaterials. Sci. Total Environ. 878, 163175.
Johnson, S., Loeppert, R., 2006. Role of organic acids in phosphate mobilization from iron oxide. Soil Sci. Soc. Am. J. 70 (1), 222–234.
Kaiser, K., Zech, W., 1997. Competitive sorption of dissolved organic matter fractions to soils and related mineral phases. Soil Sci. Soc. Am. J. 61 (1), 64–69.
Khare, N., Hesterberg, D., Beauchemin, S., Wang, S.L., 2004. XANES determination of adsorbed phosphate distribution between ferrihydrite and boehmite in mixtures. Soil Sci. Soc. Am. J. 68 (2), 460–469.
Khare, N., Martin, J., Hesterberg, D., 2007. Phosphate bonding configuration on ferrihydrite based on molecular orbital calculations and XANES fingerprinting. Geochim. Cosmochim. Acta 71 (18), 4405–4415.
Kim, D.H., 2018. Bacterial siderophores promote animal host iron acquisition and growth. Cell 175, 311–312.
Kim, H.J., Hong, J.S., Choi, J.H., Han, G.S., Jung, H.S., 2022. Effect of phosphate ions on the formation of iron oxide/hydroxide as a stabilizer. J. Solid State Chem. 305, 122688.
Kim, J., Li, W., Philips, B., Grey, C., 2011. Phosphate adsorption on the iron oxyhydroxides goethite (α-FeOOH), akaganeite (β-FeOOH), and lepidocrocite (γ-FeOOH): a ^{31}P NMR study. Energ. Environ. Sci. 4 (10), 4298–4305.
Kodama, R., 1999. Magnetic nanoparticles. J. Magn. Magn. Mater. 200 (1–3), 359–372.
Kong, X., Bai, R., Wang, S., Wu, B., Zhang, R., Li, H., 2022. Recovery of phosphorus from aqueous solution by magnetic TiO_2*/Fe_3O_4 composites. Chem. Phys. Lett. 787, 139234.
Kong, Z., Li, L., Feng, C., Chen, N., Dong, S., Hu, W., 2015. Soil infiltration bioreactor incorporated with pyrite-based (mixotrophic) denitrification for domestic wastewater treatment. Bioresour. Technol. 187, 14–22.
Kong, Z., Li, L., Feng, C., Dong, S., Chen, N., 2016. Comparative investigation on integrated vertical-flow biofilters applying sulfur-based and pyrite-based autotrophic denitrification for domestic wastewater treatment. Bioresour. Technol. 211, 125–135.
Krumina, L., Kenney, J., Loring, J., Persson, P., 2016. Desorption mechanisms of phosphate from ferrihydrite and goethite surfaces. Chem. Geol. 427, 54–64.
Kubicki, J., Paul, K., Kabalan, L., 2012. ATR-FTIR and density functional theory study of the structures, energetics, and vibrational spectra of phosphate adsorbed onto goethite. Langmuir 28 (41), 14573–14587.
Kunhikrishnan, A., Rahman, M.A., Lamb, D., Bolan, N.S., Saggar, S., Surapaneni, A., Chen, C., 2022. Rare earth elements (REE) for the removal and recovery of phosphorus: a review. Chemosphere 286 (2), 131661.
Lai, L., He, Y., Zhou, H., Huang, B., Yao, Gang, Lai, B., 2021. Critical review of natural iron-based minerals used as heterogeneous catalysts in peroxide activation processes: characteristics, applications and mechanisms. J. Hazard. Mater. 416, 125809.
Lee, M., Ahn, Y., Pandi, K., Jo, H., Choi, J., 2020. Sorption of bioavailable arsenic on clay and iron oxides elevates the soil microbial activity. Water Air Soil Pollut. 231 (411).
Ler, A., Stanforth, R., 2003. Evidence for surface precipitation of phosphate on goethite. Environ. Sci. Technol. 37 (12), 2694–2700.
Levett, A., Gagen, E., Vasconcelos, P., Zhao, Y., Paz, A., Southam, G., 2020. Biogeochemical cycling of iron: implications for biocementation and slope stabilisation. Sci. Total Environ. 707, 1–13.
Li, C., 2017. The Mechanisms on Shape Evolution of Aluminum Substituted Hematite and Its Adsorption Characteristics of Phosphate. Master's thesis,. Huazhong Agricultural University, China.
Li, L., Stanforth, R., 2000. Distinguishing adsorption and surface precipitation of phosphate on goethite (α-FeOOH). J. Colloid Interface Sci. 230 (1), 12–21.
Li, R., Kelly, C., Keegan, R., Xiao, L., Morrison, L., Zhan, X., 2013. Phosphorus removal from wastewater using natural pyrrhotite. Colloids Surf. A 427, 13–18.
Li, H., Ai, H., Kang, Li, Sun, X., He, Q., 2016. Simultaneous microcystis algicidal and microcystin degrading capability by a single acinetobacter bacterial strain. Environ. Sci. Technol. 50 (21), 11903–11911.
Li, R., Morrison, L., Collins, G., Li, A., Zhan, X., 2016a. Simultaneous nitrate and phosphate removal from wastewater lacking organic matter through microbial oxidation of pyrrhotite coupled to nitrate reduction. Water Res. 96, 32–41.
Li, W., Liang, X., An, P., Feng, X., Tan, W., Qiu, G., Liu, F., 2016b. Mechanisms on the morphology variation of hematite crystals by Al substitution: the modification of Fe and O reticular densities. Sci. Rep. 6, 35960.
Li, W., Wang, L., Liu, F., Liang, X., Feng, X., Tan, W., Yin, H., 2016c. Effects of Al^{3+} doping on the structure and properties of goethite and its adsorption behavior towards phosphate. J. Environ. Sci. China 45, 18–27.
Li, N., Tian, Y., Zhao, J.H., Zhan, W., Du, J.Y., Kong, L.C., Zhang, J., Zuo, W., 2018. Ultrafast selective capture of phosphorus from sewage by 3D Fe_3O_4@ZnO via weak magnetic field enhanced adsorption. Chem. Eng. J. 341, 289–297.
Li, M., Liu, H., Chen, T., Wei, L., Wang, C., Hu, W., Wang, H., 2019. The transformation of α-(Al, Fe)OOH in natural fire: effect of Al substitution amount on fixation of phosphate. Chem. Geol. 524, 368–382.
Li, Y., Fu, F., Cai, W., Tang, B., 2019a. Synergistic effect of mesoporous feroxyhyte nanoparticles and Fe(II) on phosphate immobilization: adsorption and chemical precipitation. Powder Technol. 345, 786–795.
Li, Y., Wang, L., Yan, Z., Chao, C., Yu, H., Yu, D., Liu, C., 2020a. Effectiveness of dredging on internal phosphorus loading in a typical aquacultural lake. Sci. Total Environ. 744, 140883.
Li, R., Wei, D., Wang, W., Zhang, Y., 2020b. Pyrrhotite-sulfur autotrophic denitrification for deep and efficient nitrate and phosphate removal: synergistic effects, secondary minerals and microbial community shifts. Bioresour. Technol. 308, 123302.
Li, X., Yan, L., Zhong, W., Kersten, M., Jing, C., 2021. Competitive arsenate and phosphate adsorption on α-FeOOH, LaOOH, and nano-TiO_2: two-dimensional correlation spectroscopy study. J. Hazard. Mater. 414, 125512.
Li, R., Zhang, Y., Guan, M., 2022a. Investigation into pyrite autotrophic denitrification with different mineral properties. Water Res. 221, 118763.
Li, Y., Zhang, C., Yang, M., He, H., Arai, Y., 2022b. Carbonate accelerated transformation of ferrihydrite in the presence of phosphate. Geoderma 417, 115811.
Li, Y., Zou, X., Liu, H., 2022c. Autotrophic denitrification over different pyrrhotites for simultaneous nitrate and phosphate removal. Acta Sci. Circumst. 42 (10), 233–240.
Li, M., Zhang, P., Guo, Z., Zhao, W., Li, Y., Yi, T., Lynch, I., 2024. Dynamic transformation of nano-MoS_2 in a soil-plant system empowers its multifunctionality on soybean growth. Environ. Sci. Technol. 58 (2), 1211–1222.
Liang, H., Liu, K., Ni, Y., 2016. Synthesis of mesoporous α-Fe_2O_3 using cellulose nanocrystals as template and its use for the removal of phosphate from wastewater. J. Taiwan Inst. Chem. Eng. 71, 474–479.
Liang, X., Lin, X., Wei, G., Ma, L., He, H., Santos-Carballal, D., De Leeuw, N., 2021. Competitive adsorption geometries for the arsenate As(V) and phosphate P(V) oxyanions on magnetite surfaces: experiments and theory. Am. Mineral. 106 (3), 374–388.
Liao, S., Wang, X., Yin, H., Post, J., Yan, Y., Tan, W., Feng, X., 2020. Effects of Al substitution on local structure and morphology of lepidocrocite and its phosphate adsorption kinetics. Geochim. Cosmochim. Acta 276, 109–121.
Lin, J., Li, Y., Zhan, Y., Wu, X., 2023. Combined amendment and capping of sediment with ferrihydrite and magnetite to control internal phosphorus release. Water Res. 235, 119899.
Lin, J., Xiang, W., Zhan, Y., 2023a. Comparison of magnetite, hematite and goethite amendment and capping in control of phosphorus release from sediment. Environ. Sci. Pollut. Res. 30, 66080–66101.

Lindegren, M., Persson, P., 2009. Competitive adsorption between phosphate and carboxylic acids: quantitative effects and molecular mechanisms. Eur. J. Soil Sci. 60 (6), 982–993.
Lindegren, M., Persson, P., 2010. Competitive adsorption involving phosphate and benzene carboxylic acids on goethite—effects of molecular structures. J. Colloid Interface Sci. 343 (1), 263–270.
Liu, F., 1997. Coordination forms and transformations of phosphate adsorbed by goethite surface on different pH. Acta Pedol. Sin. 34 (4), 367–374.
Liu, F., Jie, X., Zhou, D., 1995. Influence of pH on chemical forms of phosphate adsorbed on goethite surfaces. Pedosphere 5 (2), 157–162.
Liu, F., De Cristofaro, A., Violante, A., 2001. Effect of pH, phosphate and oxalate on the adsorption/desorption of arsenate on/from goethite. Soil Sci. 166 (3), 197–208.
Liu, H., 2013. Structural Evolution of Thermally Treated Al-substituted Goethite and Its Response of Surface Reactivity. Doctoral Dissertation,. Hefei University of Technology, China.
Liu, H., Li, P., Zhu, M., Wei, Y., Sun, Y., 2007. Fe(II)-induced transformation from ferrihydrite to lepidocrocite and goethite. J. Solid State Chem. 180 (7), 2121–2128.
Liu, H., Chen, T., Chang, J., Zou, X., Frost, R., 2013a. The effect of hydroxyl groups and surface area of hematite derived from annealing goethite for phosphate removal. J. Colloid Interface Sci. 398, 88–94.
Liu, H., Chen, T., Zou, X., Xie, Q., Qing, C., Chen, D., Frost, R., 2013b. Removal of phosphorus using NZVI derived from reducing natural goethite. Chem. Eng. J. 234, 80–87.
Liu, H., Chen, T., Frost, R., 2014. An overview of the role of goethite surfaces in the environment. Chemosphere 103, 1–11.
Liu, J., Zhu, R., Xu, T., 2016. Co-adsorption of phosphate and zinc (II) on the surface of ferrihydrite. Chemosphere 144, 1148–1155.
Liu, J., Zhu, R., Liang, X., Ma, L., Lin, X., Zhu, J., Molinari, M., 2018. Synergistic adsorption of Cd(II) with sulfate/phosphate on ferrihydrite: an in situ ATR-FTIR/2D-COS study. Chem. Geol. 477, 12–21.
Liu, J., Zhu, R., Ma, L., Fu, H., Lin, X., Parker, S., Molinari, M., 2021. Adsorption of phosphate and cadmium on iron (oxyhydr) oxides: a comparative study on ferrihydrite, goethite, and hematite. Geoderma 383, 114799.
Liu, S., Fan, F., Liu, X., Guo, Y., Ni, Z., Wang, S., 2023. Old wine and new bottles: insights into traditional attapulgite adsorbents with functionalized modification strategies applied in efficient phosphate immobilization. J. Clean. Prod. 395, 136451.
Longhurst, B., Rajendram, G., Miller, B., Dexter, M., 2017. Nutrient content of liquid and solid effluents on NZ dairy cow farms. Science and policy: nutrient management challenges for the next generation. Occasional Rep. 30, 1–9.
Longhurst, R., Roberts, A., O'Connor, M., 2000. Farm dairy effluent: a review of published data on chemical and physical characteristics in New Zealand. N. Z. J. Agric. Res. 43 (1), 7–14.
Lu, X., Wan, Y., Zhong, Z., Liu, B., Zan, F., Zhang, F., Wu, X., 2021. Integrating sulfur, iron (II), and fixed organic carbon for mixotrophic denitrification in a composite filter bed reactor for decentralized wastewater treatment: performance and microbial community. Sci. Total Environ. 795, 148825.
Luengo, C., Brigante, M., Antelo, J., 2006. Kinetics of phosphate adsorption on goethite: comparing batch adsorption and ATR-IR measurements. J. Colloid Interface Sci. 300 (2), 511–518.
Luo, C., Wen, S., An, S., 2021. Phosphate alters the compositional characteristics of humic acid adsorbed onto goethite. J. Soil. Sediment. 21, 3352–3366.
Luther, I.I.I., George, W., 1991. Pyrite synthesis via polysulfide compounds. Geochim. Cosmochim. Acta 55 (10), 2839–2849.
Lv, Y., Liu, J., Chen, C., Lin, X., Wu, X., Chen, Q., Zhu, R., 2022. Enhanced immobilization of phosphate by ferrihydrite during the photoreductive dissolution process. Sci. Total Environ. 838, 155835.
Lyu, S., Chen, W., Zhang, W., Fan, Y., Jiao, W., 2016. Wastewater reclamation and reuse in China: opportunities and challenges. J. Environ. Sci. China 39, 86–96.
Ma, J., Jing, Y., Gao, L., Chen, J., Wang, Z., Weng, L., Li, H., Chen, Y., Li, Y., 2020. Hetero-aggregation of goethite and ferrihydrite nanoparticles controlled by goethite nanoparticles with elongated morphology. Sci. Total. Environ. 748, 141536.
Ma, J., Ma, Y., Qian, X., Wang, Z., Chen, Y., Weng, L., Li, Y., 2021. Phosphorus adsorption onto ferrihydrite and predicting colloidal phosphorus transport. Chin. J. Eco-Agric. 29 (1), 85–93.
Ma, J., Li, J., Weng, L., Ouyang, X., Chen, Y., Li, Y., 2023. Phosphorus-enhanced and calcium-retarded transport of ferrihydrite colloid: mechanism of electrostatic potential changes regulated via adsorption speciation. Environ. Sci. Technol. 57 (10), 4219–4230.
Makie, P., Westin, G., Persson, P., Osterlund, L., 2011. Adsorption of trimethyl phosphate on maghemite, hematite, and goethite nanoparticles. J. Phys. Chem. A 115 (32), 8948–8959.
Mallet, M., Barthélémy, K., Ruby, C., Renard, A., Naille, S., 2013. Investigation of phosphate adsorption onto ferrihydrite by X-ray photoelectron spectroscopy. J. Colloid Interface Sci. 407, 95–101.
Mao, Y., Pham, A., Xin, Y., 2012. Effects of pH, floc age and organic compounds on the removal of phosphate by pre-polymerized hydrous ferric oxides. Sep. Purif. Technol. 91, 38–45.
Martin, R., Smart, R., Tazaki, K., 1988. Direct observation of phosphate precipitation in the goethite/phosphate system. Soil Sci. Soc. Am. J. 52 (5), 1492–1500.
Mendez, J., Hiemstra, T., 2018. Carbonate adsorption to ferrihydrite: competitive interaction with phosphate for use in soil systems. ACS Earth Space Chem. 3 (1), 129–141.
Mendez, J., Hiemstra, T., 2020. Ternary complex formation of phosphate with Ca and Mg ions binding to ferrihydrite: experiments and mechanisms. ACS Earth Space Chem. 4 (4), 545–557.
Michel, F., Barrón, V., Torrent, J., Morales, M., Serna, C., Boily, J., Brown Jr., G., 2010. Ordered ferrimagnetic form of ferrihydrite reveals links among structure, composition, and magnetism. Proc. Natl. Acad. Sci. U.S.A. 107 (7), 2787–2792.
Moharami, S., Jalali, M., 2014. Effect of TiO_2, Al_2O_3, and Fe_3O_4 nanoparticles on phosphorus removal from aqueous solution. Environ. Prog. Sustain. Energy 33 (4), 1209–1219.
Mora Mendoza, E., Sarmiento Santos, A., Vera López, E., Drozd, V., Durygin, A., Chen, J., Saxena, S., 2021. Siderite decomposition at room temperature conditions for CO_2 capture applications. Braz. J. Chem. Eng. 38, 351–359.
Moslemi, H., Gharabaghi, M., 2017. A review on electrochemical behavior of pyrite in the froth flotation process. J. Ind. Eng. Chem. 47, 1–18.
Mosse, K., Patti, A., Christen, E.W., Cavagnaro, T., 2011. Winery wastewater quality and treatment options in Australia. Aust. J. Grape Wine Res. 17 (2), 111–122.
Nanzyo, M., Watanabe, Y., 1982. Diffuse reflectance infrared spectra and ion-adsorption properties of the phosphate surface complex on goethite. Soil Sci. Plant Nutr. 28 (3), 359–368.
Nations, S., Wages, M., Canas, J.E., Maul, J., Theodorakis, C., Cobb, G.P., 2011. Acute effects of Fe_2O_3, TiO_2, ZnO and CuO nanomaterials on *Xenopus laevis*. Chemosphere 83 (8), 1053–1061.
Niculescu, A., Chircov, C., Grumezescu, A., 2022. Magnetite nanoparticles: synthesis methods—a comparative review. Methods 199, 16–27.
Nilsson, N., Lövgren, L., Sjöberg, S., 1992. Phosphate complexation at the surface of goethite. Chem. Spec. Bioavailab. 4 (4), 121–130.
Notini, L., Schulz, K., Kubeneck, L., Grigg, A., Rothwell, K., Fantappiè, G., Kretzschmar, R., 2023. A new approach for investigating iron mineral transformations in soils and sediments using ^{57}Fe-labeled minerals and ^{57}Fe Mössbauer spectroscopy. Environ. Sci. Technol. 57 (27), 10008–10018.
Parfitt, R., Atkinson, R., 1976. Phosphate adsorption on goethite (α-FeOOOH). Nature 264, 740–742.
Parfitt, R., Russell, J., Farmer, V., 1976. Confirmation of the surface structures of goethite (α-FeOOH) and phosphate goethite by infrared spectroscopy. J. Chem. Soc. Faraday Trans. 1 Phys. Chem. Condens. Phases 72, 1082–1087.
Patel, H., Vashi, R., 2015. Characterization and Treatment of Textile Wastewater. Elsevier.
Patra, A., Kundu, S., Bhaumik, A., 2016. Morphology evolution of single-crystalline hematite nanocrystals: magnetically recoverable nanocatalysts for enhanced facet-driven photoredox activity. Nanoscale 8 (1), 365–377.
Paul, E.A., Clark, F.E., 1989. Soil microbiology and biochemistry in perspective—science direct. Soil Biol. Biochem. 1–10.
Persson, P., Nilsson, N., Sjoberg, S., 1996. Structure and bonding of orthophosphate ions at the iron oxide-aqueous interface. J. Colloid Interface Sci. 177 (1), 263–275.
Qin, Y., Wu, X., Huang, Q., Beiyuan, J., Wang, J., Liu, J., Yuan, W., Nie, C., Wang, H., 2023. Phosphate removal mechanisms in aqueous solutions by three different Fe-modified biochars. Int. J. Environ. Res. Public Health 20 (1), 326.
Rahnemaie, R., Hiemstra, T., Van Riemsdijk, W., 2007. Geometry, charge distribution, and surface speciation of phosphate on goethite. Langmuir 23 (7), 3680–3689.
Rai, S., Mukherjee, A., 2015. Optimization for production of liquid nitrogen fertilizer from the degradation of chicken feather by iron-oxide (Fe_3O_4) magnetic nanoparticles coupled β-keratinase. Biocatal. Agric. Biotechnol. 4 (4), 632–644.
Randall, D., Naidoo, V., 2018. Urine: the liquid gold of wastewater. J. Environ. Chem. Eng. 6 (2), 2627–2635.
Rashid, M., Price, N., Pinilla, M., O'Shea, K., 2017. Effective removal of phosphate from aqueous solution using humic acid coated magnetite nanoparticles. Water Res. 123, 353–360.
Rashid, M., Shahzad, T., Shahid, M., Imran, M., Dhavamani, J., Ismail, I.M.I., Basahi, J. M., Almeelbi, T., 2017a. Toxicity of iron oxide nanoparticles to grass litter decomposition in a sandy soil. Sci. Rep. 7 (1), 41965.
Rietra, R., Hiemstra, T., van Riemsdijk, W., 2001. Interaction between calcium and phosphate adsorption on goethite. Environ. Sci. Technol. 35 (16), 3369–3374.
Rotaru, A.E., Shrestha, P., Liu, F., Markovaite, B., Chen, S., Nevin, K.P., Lovley, D.R., 2014a. Direct interspecies electron transfer between *Geobacter metallireducens* and *Methanosarcina barkeri*. Appl. Environ. Microbiol. 80 (15), 4599–4605.
Rotaru, A.E., Shrestha, P., Liu, F., Shrestha, M., Shrestha, D., Embree, M., Zengler, K., Wardman, C., Nevina, K.P., Lovley, D.R., 2014b. A new model for electron flow during anaerobic digestion: direct interspecies electron transfer to *Methanosaeta* for the reduction of carbon dioxide to methane. Energ. Environ. Sci. 7, 408–415.
Sabur, M., Parsons, C., Maavara, T., Van Cappellen, P., 2021. Effects of pH and dissolved silicate on phosphate mineral-water partitioning with goethite. ACS Earth Space Chem. 6 (1), 34–43.
Sanders, J., Windom, H., 1980. The uptake and reduction of arsenic species by marine algae. Estuar. Coast. Mar. Sci. 10, 555–567.
Santos, S.C., Boaventura, R.A., 2015. Treatment of a simulated textile wastewater in a sequencing batch reactor (SBR) with addition of a low-cost adsorbent. J. Hazard. Mater. 291, 74–82.
Saravanan, M., Suganya, R., Ramesh, M., 2011. Toxicity of iron oxide nanoparticles to Indian major carp, *Labeorohita* on haematological, biochemical, ionoregulatory and enzymological alterations. In: 8th International Symposium on Recent Advances in Environmental Health Research. Jackson, MS, USA, pp. 18–21.
Schwertmann, U., Murad, E., 1983. Effect of pH on the formation of goethite and hematite from ferrihydrite. Clays Clay Miner. 31, 277–284.
Sengupta, S., Nawaz, T., Beaudry, J., 2015. Nitrogen and phosphorus recovery from wastewater. Curr. Pollut. Rep. 1, 155–166.
Senn, A., Kaegi, R., Hug, S., Hering, J., Mangold, S., Voegelin, A., 2017. Effect of aging on the structure and phosphate retention of Fe(III)-precipitates formed by Fe(II) oxidation in water. Geochim. Cosmochim. Acta 202, 341–360.

Shan, S., Zhang, T., Wang, W., Liu, D., Shi, W., Cui, F., 2021. Magnetite/hydrated cerium (III) carbonate for efficient phosphate elimination from aqueous solutions and the mechanistic investigation. Chem. Eng. J. 425, 128894.
Song, K., Fu, Z., Zhao, X., Liao, H., Bai, Y., Wang, G., Wu, F., 2012. Mechanism of humic acid influence on the adsorption of phosphate on goethite. Res. Environ. Sci. 25 (8), 904–910.
Song, Q., Huang, S., Xu, L., Wang, N., Hu, Z., Luo, X., Zheng, Z., 2020. Synthesis of magnetite/lanthanum hydroxide composite and magnetite/aluminum hydroxide composite for removal of phosphate. Sci. Total Environ. 723, 137838.
Stanjek, H., 1992. The influence of aluminum on iron oxides. Part XVI: hydroxyl and aluminum substitution in synthetic hematites. Clays Clay Miner. 40, 347–354.
Strauss, R., Brümmer, G., Barrow, N., 1997. Effects of crystallinity of goethite: II. Rates of sorption and desorption of phosphate. Eur. J. Soil Sci. 48 (1), 101–114.
Sun, C., Wang, S., Wang, H., Hu, X., Yang, F., Tang, M., Zhang, M., Zhong, J., 2022. Internal nitrogen and phosphorus loading in a seasonally stratified reservoir: implications for eutrophication management of deep-water ecosystems. J. Environ. Manage. 319, 115681.
Sun, J., Bu, L., Deng, L., Shi, Z., Zhou, S., 2018. Removal of *Microcystis aeruginosa* by UV/chlorine process: inactivation mechanism and microcystins degradation. Chem. Eng. J. 349, 408–415.
Szewczuk-Karpisz, K., Kukowska, S., Grygorczuk-Płaneta, K., Kondracki, B., Jerin, K., Kovačević, D., 2023. Scavenging of copper (II) ions, phosphate (V) ions, and diuron from aqueous media by goethite modified with chitosan or poly (acrylic acid). Environ. Sci. Pollut. Res. 1–21.
Tan, W., Liang, Y., Xu, Y., Wang, M., 2022. Structural-controlled formation of nano-particle hematite and their removal performance for heavy metal ions: a review. Chemosphere 306, 135540.
Tao, L., Chen, W., Liu, Y., Yang, F., Liu, D., Liang, J., Li, H., 2023a. Competitive and synergistic effects of phosphate and cadmium co-adsorbed on goethite. Chemosphere 324, 138171.
Tao, R., Qu, M., Zhang, S., Quan, F., Zhang, M., Shen, W., Mei, Y., 2022. Preparation of FeOOH supported by melamine sponge and its application for efficient phosphate removal. J. Environ. Chem. Eng. 10 (4), 108064.
Tao, Z., Zhou, Q., Zheng, T., Mo, F., Ouyang, S., 2023b. Iron oxide nanoparticles in the soil environment: adsorption, transformation, and environmental risk. J. Hazard. Mater. 132107.
Tartaj, P., Morales, M., Gonzalez-Carreno, T., Veintemillas-Verdaguer, S., Serna, C., 2011. The iron oxides strike back: from biomedical applications to energy storage devices and photoelectrochemical water splitting. Adv. Mater. 5243–5249.
Tejedor-Tejedor, M., Anderson, M., 1990. Protonation of phosphate on the surface of goethite as studied by CIR-FTIR and electrophoretic mobility. Langmuir 6 (3), 602–611.
Theis, T., West, M., 1986. Effect of cyanide complexation on adsorption of trace metals at the surface of goethite. Environ. Technol. Lett. 7, 309–318.
Tiberg, C., Gustafsson, J., 2016. Phosphate effects on cadmium (II) sorption to ferrihydrite. J. Colloid Interface Sci. 471, 103–111.
Torrent, J., Schwertmann, U., Barrón, V., 1992. Fast and slow phosphate sorption by goethite-rich natural materials. Clays Clay Miner. 40, 14–21.
Torrent, J., Schwertmann, U., Barrón, V., 1994. Phosphate sorption by natural hematites. Eur. J. Soil Sci. 45 (1), 45–51.
Tsujimoto, Y., Tassel, C., Hayashi, N., Watanabe, T., Kageyama, H., Yoshimura, K., Paulus, W., 2007. Infinite-layer iron oxide with a square-planar coordination. Nature 450 (7172), 1062–1065.
Tüysüz, H., Salabaş, E., Weidenthaler, C., Schüth, F., 2008. Synthesis and magnetic investigation of ordered mesoporous two-line ferrihydrite. J. Am. Chem. Soc. 130 (1), 280–287.
Vaca-Escobar, K., Villalobos, M., Ceniceros-Gomez, A., 2012. Natural arsenic attenuation via metal arsenate precipitation in soils contaminated with metallurgical wastes: III. Adsorption versus precipitation in clean As(V)/goethite/Pb(II)/carbonate systems. Appl. Geochem. 27, 2251–2259.
Vieira, J., Lijklema, L., 1989. Development and application of a model for regional water quality management. Water Res. 23 (6), 767–777.
Vieira, J.D.S., 2007. Transformações biogeoquímicas na bacia hidrográfica do Rio Lis.
Von Der Heyden, B., Roychoudhury, A., Myneni, S., 2019. Iron-rich nanoparticles in natural aquatic environments. Minerals 9 (5), 287.
Waajen, G., van Oosterhout, F., Douglas, G., Lürling, M., 2016. Geo-engineering experiments in two urban ponds to control eutrophication. Water Res. 97, 69–82.
Wang, C., Yu, S., Cwiertny, D., Yin, Y., Myung, N., 2021a. Phosphate removal using surface enriched hematite and tetra-n-butylammonium bromide incorporated polyacrylonitrile composite nanofibers. Sci. Total Environ. 770, 145364.
Wang, H., Zhu, J., Fu, Q., 2015. Adsorption of phosphate onto ferrihydrite and ferrihydrite-humic acid complexes. Pedosphere 25 (3), 405–414.
Wang, J., Chen, T., Li, P., Xie, J., Ma, B., Cao, G., 2012. Removal phosphate in low concentration by pyrite. Acta. Mineral. Sin. 32 (2), 238–243.
Wang, J.F., Wang, G.X., Wanyan, H., 2007. Treated wastewater irrigation effect on soil, crop and environment: wastewater recycling in the loess area of China. J. Environ. Sci. China 19 (9), 1093–1099.
Wang, L., Ruiz-Agudo, E., Putnis, C., 2012a. Kinetics of calcium phosphate nucleation and growth on calcite: implications for predicting the fate of dissolved phosphate species in alkaline soils. Environ. Sci. Technol. 46 (2), 834–842.
Wang, L., Putnis, C., Ruiz-Agudo, E., 2015a. In situ imaging of interfacial precipitation of phosphate on goethite. Environ. Sci. Technol. 49 (7), 4184–4192.
Wang, L., Putnis, C., Hövelmann, J., 2018. Interfacial precipitation of phosphate on hematite and goethite. Minerals 8 (5), 207.
Wang, Q., Liao, Z., Yao, D., Yang, Z., Wu, Y., Tang, C., 2021b. Phosphorus immobilization in water and sediment using iron-based materials: a review. Sci. Total Environ. 767, 144246.
Wang, S.X., Huang, Y.X., Wu, Q.F., Yao, W., Lu, Y.Y., Huang, B.C., Jin, R.C., 2023. A review of the application of iron oxides for phosphorus removal and recovery from wastewater. Crit. Rev. Environ. Sci. Technol. 1–19.
Wang, W., Wei, D., Li, F., Zhang, Y., Li, R., 2019. Sulfur-siderite autotrophic denitrification system for simultaneous nitrate and phosphate removal: from feasibility to pilot experiments. Water Res. 160, 52–59.
Wang, X., Li, W., Harrington, R., 2013. Effect of ferrihydrite crystallite size on phosphate adsorption reactivity. Environ. Sci. Technol. 47 (18), 10322–10331.
Wang, X., Liu, F., Tan, W., 2013a. Characteristics of phosphate sorption-desorption onto ferrihydrite: comparison with well-crystalline Fe(hydr)oxides. Soil Sci. 178 (1), 1–11.
Wang, X., Wang, X., Zhao, J., Song, J., Wang, J., Ma, R., Ma, J., 2017a. Solar light-driven photocatalytic destruction of cyanobacteria by F-Ce-TiO_2/expanded perlite floating composites. Chem. Eng. J. 320, 253–263.
Wang, X., Hu, Y., Tang, Y., Yang, P., Feng, X., Xu, W., Zhu, M., 2017b. Phosphate and phytate adsorption and precipitation on ferrihydrite surfaces. Environ. Sci. Nano. 4 (11), 2193–2204.
Wang, X., Jiang, Z., Qian, J., Fu, W., Pan, B., 2024. Structure evolution of iron (hydr) oxides under nanoconfinement and its implication for water treatment. Environ. Sci. Technol. 58 (1), 826–835.
Wang, Z., Xing, M., Fang, W., Wu, D., 2016. One-step synthesis of magnetite core/zirconia shell nanocomposite for high efficiency removal of phosphate from water. Appl. Surf. Sci. 366, 67–77.
Wei, S., Tan, W., Liu, F., Zhao, W., Weng, L., 2014. Surface properties and phosphate adsorption of binary systems containing goethite and kaolinite. Geoderma 213, 478–484.
Wen, S., Liu, J., Dai, J., Huang, X., An, S., Liu, Z., Du, Y., 2022. Iron (hydr)oxides mediated immobilization and interaction of dissolved organic matter and inorganic phosphate: a review. J. Lake Sci. 34 (5), 1428–1440.
Wen, Z., Zhang, Y., Dai, C., 2014. Removal of phosphate from aqueous solution using nanoscale zerovalent iron (nZVI). Colloid Surf. A Physicochem. Eng. Asp. 457, 433–440.
Weng, L., van Riemsdijk, W., Hiemstra, T., 2008. Humic nanoparticles at the oxide-water interface: interactions with phosphate ion adsorption. Environ. Sci. Technol. 42 (23), 8747–8752.
Weng, Y., Vekeman, J., Zhang, H., Chou, L., Tielens, F., 2020. Unravelling phosphate adsorption on hydrous ferric oxide surfaces at the molecular level. Chemosphere 261, 127776.
Weng, Z., Ma, H., Ma, J., Kong, Z., Shao, Z., Yuan, Y., Chai, H., 2022. Corncob-pyrite bioretention system for enhanced dissolved nutrient treatment: carbon source release and mixotrophic denitrification. Chemosphere 306, 135534.
Wen-Xin, L., Wei-Na, Z., Song, S., 2023. Preparation and characterization of nano-Fe_3O_4 and its application for C18-functionalized magnetic nanomaterials used as chromatographic packing materials. Nanomaterials 13 (6), 1111.
Wheeler, D., Wang, G., Ling, Y., Li, Y., Zhang, J., 2012. Nanostructured hematite: synthesis, characterization, charge carrier dynamics, and photoelectrochemical properties. Energ. Environ. Sci. 5 (5), 6682–6702.
Xian, H., Zhu, J., Yang, Y., Li, S., Lin, X., Xi, J., Xu, Y., 2023. Ubiquitous and progressively increasing ferric iron content on the lunar surfaces revealed by the Chang'e-5 sample. Nat. Astronom. 7, 280–286.
Xie, Y., Dong, H., Zeng, G., Tang, L., Jiang, Z., Zhang, C., Deng, J., Zhang, L., Zhang, Y., 2017. The interactions between nanoscale zero-valent iron and microbes in the subsurface environment: a review. J. Hazard. Mater. 321, 390–407.
Xing, B., Chen, T., Liu, H., Qing, C., Xie, J., Xie, Q., 2017. Removal of phosphate from aqueous solution by activated siderite ore: preparation, performance and mechanism. J. Taiwan Inst. Chem. E 80, 875–882.
Xing, B., Ouyang, M., Graham, N., Yu, W., 2020. Enhancement of phosphate adsorption during mineral transformation of natural siderite induced by humic acid: mechanism and application. Chem. Eng. J. 393, 124730.
Xing, B., Zhao, B., Liu, M., Graham, N., Yu, W., 2022. The influence of crystal structure and formation path of precursor on phosphate adsorption during oxidation-hydrolysis phase transition of siderite. Chem. Eng. J. 431, 133358.
Xu, J., Koopal, L., Wang, M., Xiong, J., Hou, J., Li, Y., Tan, W., 2019. Phosphate speciation on Al-substituted goethite: ATR-FTIR/2D-COS and CD-Music modeling. Environ. Sci. Nano. 6 (12), 3625–3637.
Xu, R., Li, J., Jiang, J., 2014. Progresses in research on special chemical phenomena and their mechanisms in variable charge soils. Acta Pedol. Sin. 51 (2), 207–215.
Xu, Z., Li, Y., Zhou, P., Song, X., Wang, Y., 2022. New insights on simultaneous nitrate and phosphorus removal in pyrite-involved mixotrophic denitrification biofilter for a long-term operation: performance change and its underlying mechanism. Sci. Total Environ. 845, 157403.
Yan, Y., Wan, B., Liu, F., 2014. Adsorption-desorption of myo-inositol hexakisphosphate on hematite. Soil Sci. 179 (10−11), 476–485.
Yan, Y., Wang, X., Hu, Z., Wang, H., Yin, H., Liu, F., Feng, Xi, 2021. Research progresses on sorption and desorption characteristics of phosphate on minerals. Soils 53 (3), 439–448.
Yang, H., He, K., Lu, D., Wang, J., Xu, D., Jin, Z., Yang, M., Chen, J., 2020a. Removal of phosphate by aluminum-modified clay in a heavily polluted lake, Southwest China: effectiveness and ecological risks. Sci. Total Environ. 705, 135850.
Yang, Y., Wang, S., Xu, Y., 2016. Molecular-scale study of aspartate adsorption on goethite and competition with phosphate. Environ. Sci. Technol. 50 (6), 2938–2945.
Yang, Y., Chen, T., Morrison, L., Gerrity, S., Collins, G., Porca, E., Zhan, X., 2017. Nanostructured pyrrhotite supports autotrophic denitrification for simultaneous

nitrogen and phosphorus removal from secondary effluents. Chem. Eng. J. 328, 511–518.
Yang, Y., Chen, T., Zhang, X., Qing, C., Wang, J., Yue, Z., Yang, Z., 2018. Simultaneous removal of nitrate and phosphate from wastewater by siderite based autotrophic denitrification. Chemosphere 199, 130–137.
Yang, Y., Zhao, Y., Tang, C., Liu, R., Chen, T., 2021. Dual role of macrophytes in constructed wetland-microbial fuel cells using pyrrhotite as cathode material: a comparative assessment. Chemosphere 263, 128354.
Yang, Y., Zhao, Y., Tang, C., Mao, Y., Chen, T., Hu, Y., 2021a. Novel pyrrhotite and alum sludge as substrates in a two-tiered constructed wetland-microbial fuel cell. J. Clean. Prod. 293, 126087.
Yang, Z., Zeng, X., Sun, B., Bai, L., Su, S., Wang, Y., Wu, C., 2020b. Research progress on the stability of ferrihydrite structure and its application in arsenic fixation. J. Agro-Environ. Sci. 39 (3), 445–453.
Yao, Y., Wang, L., Zhu, X., Tu, W., Zhou, Y., Liu, R., Zou, Z., Liu, R., Sun, J., Tao, B., Wang, C., Yu, X., Gao, L., Cao, Y., Wang, B., Li, Z., Yao, W., Xiong, Y., Yang, M., Wang, W., Zou, Z., 2022. Extraterrestrial photosynthesis by Chang'E-5 lunar soil. Joule 6 (5), 1008–1014.
Yi, L., Jiao, W., Chen, X., Chen, W., 2011. An overview of reclaimed water reuse in China. J. Environ. Sci. China. 23 (10), 1585–1593.
Yin, H., Wang, J., Zhang, R., Tang, W., 2019. Performance of physical and chemical methods in the co-reduction of internal phosphorus and nitrogen loading from the sediment of a black odorous river. Sci. Total Environ. 663, 68–77.
Yoon, S., Lee, C., Park, J., Kim, J., Kim, S., Lee, S., Choi, J., 2014. Kinetic, equilibrium and thermodynamic studies for phosphate adsorption to magnetic iron oxide nanoparticles. Chem. Eng. J. 236, 341–347.
Yu, W., Liu, C., Zhang, L., Hou, P., Li, F., Zhang, B., Cheng, H., 2016. Synthesis and electrochemical lithium storage behavior of carbon nanotubes filled with iron sulfide nanoparticles. Adv. Sci. 3 (10), 1600113.
Zach-Maor, A., Semiat, R., Shemer, H., 2011. Adsorption desorption mechanism of phosphate by immobilized nano-sized magnetite layer: interface and bulk interactions. J. Colloid Interface Sci. 363 (2), 608–614.
Zeng, L., Li, X., Liu, J., 2004. Adsorptive removal of phosphate from aqueous solutions using iron oxide tailings. Water Res. 38 (5), 1318–1326.
Zhang, J., Li, R., Li, J., Liu, B., 2013. Removal efficiency of phosphorus by pyrite. Chin. J. Environ. Eng. 7 (10), 3856–3860.
Zhang, Q., Liu, H., Chen, T., Chen, D., Li, M., Chen, C., 2017. The synthesis of NZVI and its application to the removal of phosphate from aqueous solutions. Water Air Soil Pollut. 228, 321.
Zhang, X., Li, R., Liu, Z., 2017a. Performance of phosphorus removal from wastewater by natural siderite. Acta Sctent. Circum. 37 (1), 219–226.
Zhang, Y., Wei, D., Morrison, L., Ge, Z., Zhan, X., Li, R., 2019. Nutrient removal through pyrrhotite autotrophic denitrification: implications for eutrophication control. Sci. Total Environ. 662 (20), 287–296.
Zhang, Z., Yu, H., Zhu, R., Zhang, X., Yan, L., 2020a. Phosphate adsorption performance and mechanisms by nanoporous biochar–iron oxides from aqueous solutions. Environ. Sci. Pollut. Res. 27, 28132–28145.
Zhang, W., Jia, X., Chen, S., Wang, J., Ji, R., Zhao, L., 2020b. Response of soil microbial communities to engineered nanomaterials in presence of maize (*Zea mays* L.) plants. Environ. Pollut. 267, 115608.
Zhang, X., Yao, H., Lei, X., Lian, Q., Roy, A., Doucet, D., Yan, H., Zappi, M.E., Gang, D.D., 2021a. A comparative study for phosphate adsorption on amorphous FeOOH and goethite (alpha-FeOOH): an investigation of relationship between the surface chemistry and structure. Environ. Res. 199, 111223.
Zhang, X., Gang, D., Sun, P., Lian, Q., Yao, H., 2021b. Goethite dispersed corn straw-derived biochar for phosphate recovery from synthetic urine and its potential as a slow-release fertilizer. Chemosphere 262, 127861.
!"count(.//sb:host[1]//child::*//sb:date)" > Zhang, M.X., Zhao, L.Y., He, Y.Y., Hu, J.P., Hu, G.W., Zhu, Y., Khan, A., Xiong, Y.C., Zhang, J.L., . Potential roles of iron nanomaterials in enhancing growth and nitrogen fixation and modulating rhizomicrobiome in alfalfa (*Medicago sativa* L.). Bioresour. Technol. 391, 129987.
Zhao, H., Stanforth, R., 2001. Competitive adsorption of phosphate and arsenate on goethite. Environ. Sci. Technol. 35 (24), 4753–4757.
Zhao, M., Liu, H., Chen, T., Zou, X., Chen, D., Zhao, Y., Li, M., Wang, L., 2021. Enrichment of phosphate by zero-valent iron prepared by the hydrogen reduction of iron-rich ore. Acta. Mineral. Sin. 41 (6), 685–696.
Zhao, Y., Liu, H., Chen, T., Chen, D., Chen, C., Qing, C., 2021a. Performance of nano zero-valent iron derived from the decomposition of siderite in the removal of phosphate. J. Nanosci. Nanotechnol. 21 (1), 623–631.
Zhou, R.Y., Yu, J.X., Li, H.X., Chi, R.A., 2020. Removal of phosphate from aqueous solution by ferrihydrite/bagasse composite prepared through in situ precipitation method. Colloids Surf. A Physicochem. Eng. Asp. 603, 125144.
Zhu, J., Xian, H., Lin, X., Tang, H., Du, R., Yang, Y., He, H., 2018. Surface structure-dependent pyrite oxidation in relatively dry and moist air: implications for the reaction mechanism and sulfur evolution. Geochim. Cosmochim. Acta 228, 259–274.
Zhu, S., Zhao, J., Zhao, N., Yang, X., Chen, C., Shang, J., 2020. Goethite modified biochar as a multifunctional amendment for cationic Cd(II), anionic As(III), roxarsone, and phosphorus in soil and water. J. Clean. Prod. 247, 119579.
Zhu, W., Chen, J., Zhang, H., Yuan, S., Guo, W., Zhang, Q., Zhang, S., 2023. Start-up phase optimization of pyrite-intensified hybrid sequencing batch biofilm reactor (PIHSBBR): mixotrophic denitrification performance and mechanism. J. Environ. Manage. 330, 117232.
Zhu, Z., Huang, C.P., Zhu, Y., Wei, W., Qin, H., 2018a. A hierarchical porous adsorbent of nano-α-Fe_2O_3/Fe_3O_4 on bamboo biochar (HPA-Fe/C-B) for the removal of phosphate from water. J. Water Process Eng. 25, 96–104.
Zou, Y., Grace, M., Roberts, K., Yu, X., 2017. Thin ferrihydrite sediment capping sequestrates phosphorus experiencing redox conditions in a shallow temperate lacustrine wetland. Chemosphere 185, 673–680.